Title
Spectroscopy, photo-physics, and time resolved exciton dynamics of GaSe quantum dots

Permalink
https://escholarship.org/uc/item/3jt703tq

Author
Mirafzal, Hoda

Publication Date
2011-10-10

Peer reviewed|Thesis/dissertation

UNIVERSITY OF CALIFORNIA, MERCED

Spectroscopy, Photo-physics, and Time Resolved Exciton Dynamics of GaSe Quantum Dots and Various Morphologies of Heterostructures of CdTe/CdSe Semiconductor Nanoparticles

A dissertation submitted in partial satisfaction of the requirements for the degree of

DOCTOR OF PHILOSOPHY

in

Physical Chemistry

by

Hoda Mirafzal

Dissertation Committee:

Professor David F. Kelley (Advisor)

Professor Anne M. Kelley (Chair)

Professor Jay Sharping

Professor Michael Colvin

2011

TABLE OF CONTENTS

LIST OF ILLUSTRATIONS

List of Figures

6

List of Tables

ACKNOWLEDGEMENTS

I would like to express my deepest thanks and appreciation to my advisor, Dr. David F. Kelley, for his continuous guidance and support during my graduate career. Without his nonstop help, patience, great ideas, and scientific knowledge, this work would have not been possible. It should be acknowledged that certain parts of this dissertation come from grant proposals or articles written by Dr. Kelley. My honest thanks go to him for these essential contributions. I would like to extend my gratitude to the members of Dr. Kelley's group, specifically Dr. Xichen Cai, Deborah Lair, Dr. Zhong-jie Jiang, Dr. Lian Shoute, and Cory Sobotta for their contributions to some of the material discussed in this dissertation, the thought-provoking and intellectual dialogues, their willingness to help at all times, and most importantly their company. My special thanks go to Dr. Xichen Cai, with whom I have had the pleasure of co-authoring two in-press publications on CdTe/CdSe heterostructures. I wish to acknowledge the electron microscopy lab at University of California – Berkeley and their staff for allowing me to use their facility to obtain TEM images that were crucial to the progress of my dissertation. I also would like to acknowledge Dr. Valerie Leppert and Kennedy Nguyen for providing some of the TEM images that helped the advancement of my research.

Last, but certainly not the least, I wish to express my most genuine and humble thanks to my loveliest Maman, best Baba, and the most wonderful brother, Kia, to all of whom I am greatly indebted for a life full of joy and kindness.

ABSTRACT OF DISSERTATION

The first part of this dissertation discusses GaSe monomer and aggregated particles. GaSe nano-disks have been prepared by several different synthetic methods. A study on the effect of various ligations suggests that well-aggregated stable particles are ligated by tight-binding alkyl phosphonic acid anhydrides. Addition of dodecyl aldehyde to particles that are primarily ligated by trioctylphosphine and trioctylphosphine oxide results in strongly coupled aggregates that cause a large red shift of the absorption spectrum (1600 cm^{-1}) and the reversal of singlet and triplet states. This spin reversal results in changes in time-resolved anisotropy and a dramatic decrease in radiative lifetime. The quantum yield of particles increases from 4.7% in monomers to 61% in strongly coupled aggregates. GaSe aggregates can be mixed with a smectic-A phase liquid crystal, LC (4-octyl, 4'-cyanobiphenyl), where the liquid crystal forces the particles to form long stacks that are in line with the director axis of the LC. This only happens when the synthesized GaSe particles are extremely well-aggregated.

The second part of this dissertation discusses the synthesis and exciton dynamics of various morphologies of CdTe/CdSe nano-heterostructures. Highly luminescent CdTe spherical nanoparticles with an average size of 3.4 nm are synthesized using a novel synthetic method that uses Octadecylphosphonic acid in the Te precursor. These particles can have a quantum yield of up to 90%. Core/shell and dot/tetrapod CdTe/CdSe heterostructures synthesized from these Te cores are used to study the biexciton Auger dynamics and the electron cooling rates in these structures by means of femtosecond transient absorption measurements. An effective mass

approximation (EMA) is used to model the exciton dynamics, specifically Auger times, in these particles. Calculations of the electron and hole wavefunctions using the EMA model predict electron and hole overlap and radiative lifetimes that match those of the experimental data. A better agreement between the experimental and calculated data is observed if compression effects, resulting from depositing a smaller-lattice shell onto a larger-lattice core, are considered. The analysis shows that as thicker Se shells are deposited, both the Auger and electron cooling processes are progressively suppressed, as expected. Calculations show that the Auger time is a strong function of, and thus directly proportional to the coulombic interaction energy between the electron and the hole.

INTRODUCTION

Nanotechnology deals with the discovery and engineering of scientific phenomena at the nanometer (10^{-9} meters) scale. Nanoparticles, particles ranging from 1 to 100 nm in size, often exhibit properties that are different from the bulk material. In a sense, nanoparticles serve as the bridge between bulk material and individual atoms. In bulk material, physical, chemical and optical properties of the sample are not affected by the size of the sample. Nanoparticles, however, show optical properties that are strongly dependent on their size. Since bulk chemistry and classical electromagnetic physics are often inadequate to explain the observed phenomena, scientists in the field of nanoscience have to constantly use quantum physics and chemistry for their research. In addition, the larger surface area of nanoparticles makes the properties of surface molecules dominant, while in bulk samples, the properties of the sample are determined by the molecules in the bulk of the material and surface molecules can be ignored.

Even though nanoparticles have been used by artisans over the years, scientific research on their properties and potential usage in modern technology is fairly new. Colored glass used to decorate church windows is an example, where old glassmakers used gold nanoparticles to create a variety of glass colors. Artisans during Middle Ages and the Renaissance also used gold or copper particles to create a glitter thin film over pottery. Although nanoparticles have been used unknowingly over the past centuries, the science is considered at most about 50 years old. The word "nano-technology" was first used by Taniguchi in a paper he published about ion-sputter machining in 1974. During 1980's the science got a big boost primarily because of new advancements in the field of cluster science and the invention of scanning tunneling microscope

(STM). Carbon nanotubes, semiconductor nanocrystals, quantum dots, and atomic force microscopy (AFM) were all breakthroughs that followed in later years.

Semiconductor nanocrystals are of particular interest for this dissertation. They are defined as semiconducting particles that are single-crystalline. The single-crystallinity of these particles eliminates the complications associated with crystal lattice defects and grain boundaries that are present in bulk samples. Small semiconductor nanocrystals (usually <10 nm) that are quantum confined in all three dimensions are referred to as quantum dots (QD). The size-dependent and tunable optical properties of these dots are the unique characteristics that make them so interesting. Applications of quantum dots range from LEDs, lasers, photovoltaics, solid-state computing, to highly sensitive cellular imaging in biological research. The amount of research and publications in this area is so vast that it is practically impossible to keep track of. Among the widely researched semiconductor QDs are CdSe, CdTe, ZnS, ZnSe, and PbS. A rather recent advancement in this area of research is the synthesis of semiconductor heterostructures, where a QD core is coated with a semiconducting material shell. Optical properties, electron and hole dynamics, and charge transport through these heterojunctions has evolved to a whole new branch of research in the past years. A major part of this dissertation will concentrate on the properties and electrodynamics of type II CdTe-CdSe core-shell heterostructures.

Semiconductor particles such as gallium selenide (GaSe) have not been getting much attention in the scientific community simply because they are extremely hard to synthesize. The first part of this dissertation will focus on the synthesis, optical properties and spectroscopic characteristics of monomer and aggregate gallium selenide quantum dots.

PART I. GaSe NANOPARTICLE AGGREGATES

Chapter One: What are GaSe Quantum Dots?

1.1. Basic Properties.

Layered semiconductors have been of special interest because of their intrinsic plate-like crystal structure and their potential applications in memory devices. Examples of these semiconductors are molybdenum disulfide, lead iodide, and gallium selenide, in which the unique layered structure leads to quasi two-dimensional behavior of electrons in between the sheets[1]. Bonding within the layers is covalent and thus strong, whereas the interactions between the layers are governed by Van der Waals forces.

Among III-VI semiconductors, GaSe quantum dots are of particular interest due to their unique optical properties arising from the disk-like morphology. GaSe particles discussed in this dissertation are nanodisks of approximately less than 8 nm in diameter and about 4 atoms thick[2]: a single tetra-layer of Se-Ga-Ga-Se atoms with strong double bonds between the gallium atoms. Figure 1 depicts the crystal structure of bulk GaSe and a TEM image confirming the disk-like morphology. Se atoms cover the outer faces of the disks whereas gallium atoms are only exposed at the edges. Edge ligands that bind to the gallium atoms play an extremely important role in the stability and extent of aggregation of these particles. Synthetic methods and role of various ligands will be discussed in detail in later chapters. Prof. Tao Ye UC-Merced provided AFM images of the nanodisks, confirming the thickness of the dots to be around 0.7 to 1 angstroms, equivalent to thickness of four atoms. Figure 2 presents the AFM image and the topographical height curve. As a result of their morphology, these particles are expected to have highly

anisotropic spectroscopic properties and also exhibit large interparticle electronic interactions[3]. Organized arrays of these tightly interacting particles show extremely promising optical properties: They can serve as a channel for exciton migration, efficiently collect and transport energy, and even be used as birefringent material.

Most semiconductor quantum dots have a defined three-dimensional crystal structure that hinders strong interparticle coupling. Their crystal structure puts the particle centers at relatively large distances from each other, therefore suppressing dipolar interactions. However, it has been shown that GaSe nanoparticles spontaneously form strongly interacting aggregates[4]. The electromagnetic interaction between the disks is about 1000 cm^{-1}, whereas this interaction is only on the order of a few wavenumbers in nanospheres of comparable size[5]. The transition density can be modeled as a dipole located at the particle center. Dipole approximations are valid when the size of the dipole in comparison to the distance in between the dipoles is small. This is true in case of GaSe nanodisks. Thus, stronger interparticle interactions are expected in the case of nanodisks. The two-dimensional disks stack on top of each other to form one-dimensional linear aggregates. Naturally, there is substantial amount of disorder in the aggregates and thus they are linear only over a few number of particles. As mentioned before, strongly interacting aggregates of GaSe particles have a great potential for becoming efficient antennas for energy transfer.

1.2. Optical Properties.

What happens when GaSe dots are photoexcited? The principal idea is that upon excitation, the incident photon kicks an electron out of the valence band and into the conduction band, leaving behind a hole in the valence band. The bound state of an electron-hole pair is called an exciton. This exciton can be localized over a single particle or delocalized over several ones. Bulk GaSe has an indirect band gap at about 2.1eV. In the relatively larger nanodisks (8 to

10nm is diameter), there is only z-axis quantum confinement which causes the absorption onset to move to the blue of bulk GaSe bandgap by about 0.6eV. The lowest energy transition lies at Γ and is z-polarized (Figure 3)[6]. Z-axis is defined to be the axis perpendicular to the plane of the nanodisks. This z-polarized direct transition for a monomer absorbs at about 405nm and has an onset at about 470nm giving it a deep yellow color (Figure 4). Following photoexcitation, the nanoparticles exhibit moderately intense fluorescence, also largely polarized along the z axis. The fluorescence quantum yield of as-synthesized particles is typically 10-15%[4]. There is also a slightly higher energy transition at Γ that is x,y-polarized and has an onset at about 350nm. Figure 5 shows a typical absorption and photoluminescence spectrum of GaSe monomers. The exciton in a monomer can be modeled as a particle in a cylinder (the nanodisks).

Several studies have characterized the size-dependent spectroscopy and relaxation dynamics of GaSe nanoparticles and aggregates of these nanoparticles[7,8,9,10,11,12]. The aggregates are (locally) one-dimensional; that is, the disk-like nanoparticles stack to form linear aggregates. Electromagnetic coupling between transitions on adjacent particles results in the formation of delocalized singlet excitons. The alignment of the *z*-polarized lowest energy transition results in the lowest energy singlet exciton transition having most of the oscillator strength. This behavior is strongly reminiscent of the lowest energy transitions in organic J aggregates; they shift to the red and become narrower at high concentrations[13,14,15,16,17]. The second transition is *x,y*-polarized (polarized in the plane of the nanoparticle) and, therefore, has the opposite behavior; it shifts to the blue and, thus, behaves like an H aggregate. The spectroscopy of these aggregates is largely determined by the relative magnitude of the interparticle (dipolar) couplings and the inhomogeneous width of the transitions. The as-synthesized particles form aggregates with interparticle couplings[11] of about 300 cm^{-1}. This is significantly less than the energetic

inhomogeneity of the monomers, about 1000 cm^{-1}, which will be discussed in detail in chapter three of this part. As a result, optical excitation produces an exciton with a coherence length (the number of particles over which the exciton is delocalized) that is short, on average, about two to three particles. Time resolved luminescence depolarization studies indicate that these excitons readily diffuse along the one-dimensional aggregate, with a diffusion constant of 2×10^{-5} cm^2/s.

1.3. A Theoretical Approach: Extension of a Dimer Model to an N-mer.

Consider the case of monomers interacting to form aggregates; nanodisks that are stacked on top of each other. Because of the interaction between the forming monomers of the aggregates, the excited state becomes delocalized over a few particles. GaSe aggregates and their transitions to excited state can be best described by a coupled dimer model. The zero'th states of a coupled dimer are $|\phi_1{*}\phi_2>$, $|\phi_1\phi_2{*}>$, where ϕ_1 and ϕ_2 are wavefunctions of monomer 1 and monomer 2, respectively. The monomers are uncharged and so the electronic interaction between them is dominated by dipole-dipole coupling. Hamiltonian of the dimer can be written as H=H$_1$+H$_2$+V$_{12}$ where V$_{12}$ is the operator describing the dipole-dipole interaction:

$$V = \frac{1}{R^3}(\vec{\mu_1}.\vec{\mu_2}) - \frac{3}{R^5(\vec{\mu_1}.\vec{R})(\vec{R}.\vec{\mu_2})}$$

The eigenfunctions for this Hamiltonian are the linear combinations of the zero'th dimer states:

$$\Psi_1 = (2^{-1/2})(\phi1{*}\phi2 + \phi1\phi2{*})$$

$$\Psi_2 = (2^{-1/2})(\phi1{*}\phi2 - \phi1\phi2{*})$$

Consider the z-polarized transition in a coupled dimer (Figure 6). The dimer excited state splits into two levels with a splitting of 2V$_{12,z}$ corresponding to the two linear combinations. The lower energy transition corresponds to the in-phase, head-to-tail arrangement of the coupled oscillators and has a positive net dipole and therefore a large oscillator strength. This low energy head-to-

17

tail arrangement is very much analogous to the J-aggregates in organic dyes. The other transition (i.e. the higher energy one) corresponds to the head-to-head or tail-to-tail arrangement. The dipoles are cancelled and thus this transition has no oscillator strength. The x,y-polarized transitions are analogous to the H-aggregates of organic dyes in that the lower energy arrangement of the dipoles has no oscillator strength due to the cancellation of dipoles. The higher energy state has a positive net dipole and therefore all the oscillator strength. The focus of my project was on the z-polarized transition and so there will be no further discussion of the x,y-polarized transition. It should be clear that extension of the dimer problem to a trimer problem creates three excited state levels with the lowest energy level having the largest oscillator strength. It is critical to realize that the lowest energy state of a trimer is lower in energy than the lowest energy state of a dimer. So, one should expect that a trimer absorbs to the red of a dimer. A further extension of the dimer problem to an n-mer is a proper model capable of describing GaSe aggregates. By analogy to the dimer problem, the excited n-mer state is split into n levels with the lowest energy transition having all the oscillator strength. Notice that the more monomers are coupled, the lower the excited state energy.

Chapter Two: Synthesis

2.1. The Established Synthetic Procedure.

GaSe nanoparticle samples are synthesized using slight variations of the same methods reported in a previous publication2. In general, 11.25 mmol of $Ga(CH_3)_3$ are mixed with 15.75 mmol of TOPSe in a total volume of 15 mL of purified trioctylphosphine (TOP) in a nitrogen atmosphere. The Se to Ga ratio is mostly selected to be somewhere between 1.1:1 to 1.5:1 to have some excess Se in the reaction mixture. As long as chosen within the recommended window, minor variations in Se:Ga ratio do not affect the quality of the synthesis dramatically. Ga precursor concentration can be varied from 0.75 to 1 M depending on what the desired final particle concentration is. Generally speaking, higher concentration of reactant precursors do result in slightly better aggregated particles. Building on the dimer problem discussed in section 1.3, when the two or more oscillators couple, the lowest z-polarized transition drops in energy and the corresponding absorption peak moves to the red. At the same time, the higher x,y-polarized transition in the coupled oscillator has a higher energy than the corresponding transition in the monomers, and thus, the absorption peak moves to the blue. This splitting of the lower z-polarized and higher x,y-polarized transitions created a valley in the absorption spectrum. Therefore, the tentative estimation of aggregation can be known by measuring the peak to valley ratio of the absorption spectrum. Also, Ga concentrations of lower than 0.75 typically result in monomer particles with low degree of aggregation.

The TOP is prepared by careful vacuum distillation of tech-grade TOP. This TOP is sealed

and kept in a glove-box to avoid any oxidation to trioctylphosphine oxide (TOPO). The distillation is performed using an apparatus in which all the joints have been ground together and sealed with Teflon O-rings, ensuring a leak-free vacuum. The fraction between 210 and 230 °C is kept. It is important to note that the distillation temperature is a strong function of vacuum pressure, and thus can be different on various Schlenk lines. Small amounts distill at lower temperatures, and small amounts are left behind at temperatures above 230 °C. We note that typical distillations and the subsequent synthesis reaction using standard glassware with ground joints and Teflon sleeves result in the formation of very slight amounts of phosphonic and phosphinic acids that undergo dehydration to the corresponding anhydrides. But with no controlled addition of these anhydrides, there's usually little produced and the concentrations are unknown and unpredictable. Further details can be found in section 2.3 of this chapter. ^{31}P NMR and GCMS indicate that these TOP solutions do contain little of these compounds.

The Se precursor is made by mixing the required amount of Se in about 10 mL (or 2/3 of total TOP volume) of TOP. This mixture is then stirred vigorously at 120 °C for at least 30 minutes under nitrogen flow. This assures that the solution is completely oxygen-free before the Ga precursor is injected into it. The Ga precursor is prepared by injecting trimethylgallium into about 5 mL (or 1/3 of total TOP volume) of TOP in the glove-box. This precursor is then taken out of the glove-box in a sealed vial and injected into the Se precursor that has been stirring at 120 °C. The reaction is then quickly heated to 268 °C and maintained at that temperature for 90 minutes under nitrogen flow. Upon cooling, some of the smaller particles may precipitate and the solution may become turbid. This is possibly a characteristic of reaction solutions lacking strongly binding ligands, specifically, phosphonic and phosphinic anhydrides. The only edge-binding ligands in this type of syntheses are TOP and very small amounts of TOPO, which bind

relatively weakly. The lack of strongly binding edge ligands allows the particles to irreversibly agglomerate, thereby limiting their solubility. The precipitated particles are removed by centrifugation, leaving a clear yellow solution. An example of the absorption and emission spectrum of this solution can be seen in Figure 12 and Figure 13; the corresponding curves are labeled "as-synthesized". The absorption onsets indicate that this type of anhydride-free synthesis typically gives particles having diameters of 5-6 nm. Syntheses in which tightly-binding ligands are used can result in particles that are up to 12 nm in diameter.

2.2. "Greener" Synthetic Alternatives

As explained above, GaSe nanoparticles are synthesized by the reaction of $Ga(CH_3)_3$ with trioctylphosphine selenium (TOPSe) in a high-temperature coordinating solvent. The nanoparticles consist of single Se-Ga-Ga-Se tetra-layers with the top and bottom Se sheets being coordinately saturated and therefore relatively inert. In contrast, the edges of these particles have dangling bonds and are reactive. The particle edges are passivated during the synthesis by the presence of the coordinating solvent, in this case, trioctylphosphine (TOP) and/or trioctylphosphine oxide (TOPO). TOP and TOPO effectively coordinate the edges of the particles and thereby prevent the particles from forming bulk GaSe. They also control the particle growth kinetics and allow 'focusing' of the particle size distribution[18]. This method was devised in analogy to the CdSe synthesis[19]. This synthesis reliably produces strongly fluorescent, size-controlled, monodisperse particles. It does, however, have two significant problems; the use of TOP and TOPO as coordinating ligands, and the use of $Ga(CH_3)_3$ as a gallium source. These considerations motivated a careful look at the methods of GaSe nanoparticle synthesis.

The problems associated with the use of TOP and TOPO in the synthesis of CdSe nanoparticles are well known. The chemistry of gallium is significantly different than that of

cadmium, specifically, gallium has a much greater affinity for oxygen than does cadmium. This creates greater difficulties in the synthesis and especially the subsequent manipulation of the GaSe particles in a TOP/TOPO solvent. The main difficulty is the oxidation of TOP and the relative extents to which TOP and TOPO bind to GaSe nanoparticles. TOP is easily oxidized to TOPO, which binds much more strongly to the edges of GaSe nanoparticles. Although TOP is a bulky ligand, it does not bind so tightly to the particles to inhibit the formation of strongly interacting aggregates. In contrast, TOPO binds very strongly to the nanoparticles, completely inhibiting aggregate formation. Although TOP and TOPO may be displaced by coordinating other ligands such as hexadecylamine or alkyl carboxylic acids, they are somewhat difficult to eliminate from the final solution. Thus, although particles synthesized by this method are very stable, the extent to which the particles aggregate is difficult to control and a lot of times unpredictable.

One of the main projects in Dr. Kelley's lab at the time was to align GaSe aggregates in liquid crystal (LC) samples to study exciton dynamics and charge flow through the long chains of aggregates. Chapter Four: Alignment of GaSe Aggregates in Liquid Crystal Samplesof this part will discuss some aspects of this project. In addition to the above problems, TOP and TOPO were structurally incompatible with incorporation of the aggregates into liquid crystals. Liquid crystals consist of long, rod-like molecules that form phases having orientational and in some cases positional order. TOP and TOPO are bulky three-dimensional, rather than a linear molecules and therefore destroy the LC alignment at moderate to high concentrations. In the presence of TOP and TOPO, the concentration range over which GaSe nanoparticles can be incorporated into liquid crystals is limited by the incompatibility of liquid crystal phases with high concentrations of TOP and TOPO. High concentrations of nanoparticles and their ligands

will allow the LC material to maintain an ordered LC phase only if the binding ligands are more or less linear. It was therefore desirable to either replace the TOP and TOPO ligands with linear ones, or avoid their use altogether. In order to address this issue, one of things tried was the addition of dodecyl aldehyde to GaSe particles after synthesis to replace the bulky TOP/TOPO ligands. This successful ligand exchange brought about excellent optical properties and dynamics which will be discussed in minor details in Chapter Three: Singlet/Triplet Reversal in Strongly Coupled GaSe Aggregates. In general though, TOP is difficult to purify, easily oxidized, expensive, odorous and generally undesirable. Thus, elimination of TOP and TOPO from the synthesis is preferable to replacing the ligands on the final particles. As such, this section will report the alternative synthetic methods that were used to develop a better greener synthesis of GaSe particles by eliminating TOP/TOPO or trimethylgallium (TMGa).

First attempt was to run the synthesis in a non-coordinating solvent and linear edge-binding ligands, for example, using octadecene (ODE) as the solvent and a coordinating ligand such as octadecylamine (ODA) or a carboxylic acid such as oleic acid (OA). ODA or OA and ODE are oxidatively stable and much more compatible with liquid crystals. They are also easy to get pure and free of trace amounts of air and water. (Trimethylgallium is extremely reactive with air and water, and we have found that great care must be taken to ensure that all reagents are rigorously anhydrous and anaerobic.) Sample syntheses are chosen to show the effects of these changes. Figure 7 shows a comparison between four chosen types of syntheses. Sample 1 shows nicely aggregated particles that were synthesized by Lian Shoute, a former postdoctoral fellow in 2006. The superb peak to valley ratio of about 3.4 suggest a high degree of aggregation. This is a traditional synthesis done using TMGa and TOP-Se and thus can be thought of as the control experiment. Sample 2 shows a synthesis where ODA is used as the coordinating ligand and TOP

is replaced with octadecene in both Se and Ga precursors. Using TOPSe as the source of selenium obviously requires the purification of TOP and ending up with some TOP in the final mixture. However, it is possible to make a (fairly dilute) solution of selenium in ODE. It has recently been shown that selenium will dissolve in deoxygenated ODE at 200 ºC, forming stable, clear dispersion of selenium allotropes[20]. This type of solution has been used as the selenium source in the synthesis of CdSe nanoparticles, and was tried in this synthesis as well. The Se precursor was prepared by dissolving Se and ODA in ODE and the Ga precursor was prepared by directly dissolving TMGa in ODE.

In addition, numerous syntheses were done in an attempt to eliminate trimethylgallium and replace it with less toxic, less volatile Ga sources such as gallium acetylacetonate $(Ga(acac)_3)$, gallium chloride $(GaCl_3)$, and even tributylgallium. $GaMe_3$ is pyrophoric and can only be handled and in a glovebox with an extremely good atmosphere. (We typically maintain sub-ppm oxygen levels.) Furthermore, the use of pure, liquid $GaMe_3$ is very undesirable because it is quite volatile (b.p. of 55 ºC) and will irreversibly deactivate the glovebox catalysts. This makes it very difficult to handle. A better synthesis might start with a gallium salt, rather than an organometallic. Gallium oxide or halides are too stable and would not be expected to react. We noted that the chemistries of gallium and indium are very similar (both form very strong oxygen and halide bonds) and $In(acetate)_3$ is used as the metal source in the synthesis of InP. This suggested that $Ga(acac)_3$ will be sufficiently reactive and thus, several syntheses were tried with $Ga(acac)_3$. Sample 3 and 4 shown in Figure 7 show selected absorption spectra. In sample 3, the Se precursor was made by dissolving Se in tributylphosphine (a smaller molecule than TOP although it has very similar chemical properties). The Ga precursor was prepared by dissolving $Ga(acac)_3$ and ODA in ODE. In sample 4, the Se precursor was made by dissolving Se in

minimal TOP and then diluting it in ODE, and the gallium precursor was prepared by dissolving $Ga(acac)_3$ in a mixture of oleic acid and ODE. As the graphs in Figure 7 suggest, although use of these "greener" reagents does result in growth of GaSe particles, none of these alternative syntheses seem to produce well-aggregated monodisperse particles. In addition, the absorption peak onsets of the spectra imply that the particles produced are relatively small, approximately 3 – 5 nm. This limits the usefulness of the particles, particularly for use in LC samples where coherent stacking of the nanodisks is only obtained with larger diameter particles. All in all, the most promising of these syntheses appears to be sample 3 with a TBP-Se precursor and a $Ga(acac)_3$-ODA-ODE solution as the Ga precursor. This protocol produces particles that are somewhat focused and not as small as the other ones.

In a continuing effort to replace TMGa, few syntheses were carried out with gallium chloride. Gallium chloride comes in the form of solid pellets kept in ampules under argon. It does turn into gallium oxide once exposed to air, but not as quickly as TMGa and it certainly doesn't catch fire! It is also much less volatile, less expensive and easier to handle. The Se precursor in these syntheses was made as always and gallium chloride was simply dissolved in TOP at slightly warm temperatures (not soluble at room temperature.) The Se and Ga precursors were mixed and heated to the regular reaction temperature of 268 ^{o}C. However, no signs of a reaction or particle production were observed. It was expected that upon the dissolution of gallium chloride, gallium atoms will bond with the phosphorous atoms of TOP, and $Cl_2(g)$ will be released as a vapor. However, our experimental observation was that the Ga-Cl bonds seem to lie at a lower energy than Ga-P bonds. We also tried synthesizing tributylgallium in hopes of it being slightly easier to handle due to its higher boiling point. Tributylgallium was synthesized by a reaction between gallium chloride and butyl lithium in ether. Lithium chloride, a solid salt is

another product of this reaction:

$$GaCl_3 + 3\ CH_3(CH_2)_3Li \rightarrow TBGa + 3\ LiCl_{(s)}$$
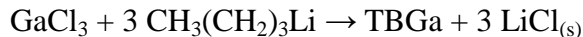
Low amounts of tributylgallium were successfully synthesized by this method. However, extracting pure tributylgallium from the lithium chloride mud proved to be, at the least, practically not feasible.

It was hoped that the above improvements will result in a much easier, "greener" synthesis that produces particles having edge passivation ligands that coherently aggregate in long chains. Coherent aggregation and organization of GaSe particles imposes several criteria on what can be considered a good synthesis. First, the synthesized particles should be relatively large in diameter. This allows for stronger interaction between adjacent nanodisks and therefore provides for formation of longer kink-free aggregate stacks. Second, the size distribution should be narrow. Large inhomogeneities in nanodisk diameters cause kinks or breaks in the aggregate stack. And third, edge ligations should be just right to allow for optimal amount of interaction between the particles. On one end of the spectrum are bulky ligands like TOP or TOPO that can inhibit coupling between the particles and prevent stacking. On the other end of the spectrum are small linear ligands such as dodecyl aldehyde, which allow for such close interaction that once two adjacent monomers pair, they form these strongly coupled dimers that don't like to stack on other dimers. This will be discussed in detail in Chapter Three: Singlet/Triplet Reversal in Strongly Coupled GaSe Aggregates.

2.3. A Study on Ligation Effects.

GaSe nanoparticles were synthesized in the presence of tightly binding ligands. These ligands are formed by heating a solution of pure TOP and octadecylphosphonic acid (ODPA) at 170 ^{o}C for about 12 hours. GaSe particles made by this synthesis are well aggregated and

extremely stable over time. GC-MS data imply that the ligand molecule is relatively heavy. P-31 NMR data show signature peaks of anhydride functional groups, all of which suggests that the ligand is possibly an anhydride molecule. In addition, it was found that the commercial TOP from Aldrich contains free radicals that vary from lot to lot. These free radicals seem to play a significant role in the success of GaSe syntheses.

What are the differences between weaker (loosely-binding) and stronger (tightly-binding) ligands? We speculate that upon nucleation of particles during a reaction, weaker ligands such as TOP or TOPO passivate the gallium dangling bonds at the edges of the particles just enough to still allow for further growth and size-focusing of the particles. However, particles synthesized by this method suffer from short shelf-life (on the order of a couple of weeks). Slightest introduction of oxygen into the sample, leads to oxidation of the edge gallium atoms. Keep in mind that Ga-O bonds are energetically more favored than Ga-P bonds. Weaker ligands can also be easily replaced with much stronger ligands such as dodecanal. Stronger ligands could potentially inhibit the interaction between fresh nuclei in the reaction and therefore suppress particle growth and size-focusing. Thus, the amount of coordinating ligand used in the synthesis is very critical in order to get optimal focusing of the size distribution. It was found that a high concentration of strong ligands such as phosphonic acid (PA) anhydrides often leads to polydisperse samples. The correct concentration range lies somewhere between 2 to 5 % for long-chained phosphonic acids, depending on which one is used. Particles synthesized using these stronger phosphonic acid anhydride ligands are generally very stable, much less sensitive to oxygen, and last for months without any of their optical properties degraded. It is interesting to note that dodecanal does not effectively replace these long-chained PA anhydride ligands, which further supports the idea that they probably grab on the particle edges very tightly. Please note

that dodecyl aldehyde, DDA (or dodecanal) is always added to the particles after they are synthesized. An obvious synthesis to try would be one where dodecanal is present in the Ga precursor from the beginning of the reaction. However, since the reactions are run at about 268 ^{o}C and the boiling point of dodecanal is at 237-239 ^{o}C, this was practically problematic. Longer chain aldehydes such as octadecyl aldehyde (stearyl aldehyde) that have a boiling point of 320 ^{o}C could serve as promising alternatives. A synthesis using stearyl aldehyde was never performed.

GaSe nanoparticles with tightly-binding PA anhydride ligands were synthesized using a variation of the methods previously reported in section 2.1 of this dissertation. Since this method produces especially long-lasting, stable, well-aggregated particles with clean optical properties, details of the synthesis are reported as follows. Here is the list of chemicals used. Trioctylphosphine (TOP), technical grade 90 % form Aldrich; Trioctylphosphine oxide (TOPO), technical grade 90 % from Aldrich; n-Octadecylphosphonic Acid (ODPA), 90 % from PCI synthesis; Dioctylphosphinic acid (DOPA), 99 % from Dr. William Buhro's group at Washington University; Trimethylgallium, 99+ % from Strem Chemicals; Selenium powder, 90+ % from Alfa Aesar. TOP was purified by vacuum distillation and was sealed and kept in the glove box under oxygen free atmosphere. ODPA was purified by double recrystallization from acetonitrile. TOPO was purified by double recrystallization from toluene. The rest of the chemicals were used as received.

In this case, a 3.5% ODPA mixture was made by mixing 0.204 g of ODPA and 7.5 mL of distilled TOP. This mixture was heated at 170 ^{o}C for about 12 hours. It is of utmost importance to heat this precursor solution for a long time. The synthesis carried with non-heated precursors resulted in less stable particles that are low in concentration as well. The Se precursor consisted

28

of 7.6 mmols of Se dissolved in 5 mL of the 3.5% ODPA solution. The Ga precursor, consisted of 5.6 mmols of trimethylgallium dissolved in 2.5 mL of the 3.5% ODPA solution, was then added to the Se precursor. The reaction was run at 268 ^{o}C for 90 minutes. For purposes of simplification, let's call this synthesis, synthesis A.

A few aliquots were taken in the duration of the reaction to monitor the growth of the particles. Due to the presence of the tightly binding edge ligands, the reaction stayed clear up to 75 minutes into the reaction. After the reaction was shut off at 90 minutes, the turbid solution of particles was centrifuged to obtain an optically clear solution. The particles were then kept in the glove box. Figure 8 shows the absorption of the particles measured two months after synthesis. As seen in the figure, not only the particles have not deteriorated but rather they have become better aggregated and also the size distribution has become more focused. Particles made by this method are extremely stable and can keep for months. As previously reported, ligations on GaSe particles that are loosely bound by TOP or TOPO can be easily displaced by long chain aldehydes such as dodecyl aldehyde. This displacement causes a tighter interaction between the monomers, and thus shifts the absorption spectrum to the red by about 50 nm. Addition of dodecyl aldehyde to this set of particles however, produces a smaller shift in the absorption spectrum. This again implies that the particles are very tightly bound. Figure 9 shows the particles before and after the addition of dodecyl aldehyde.

A more thorough study was carried to further investigate the effect of different ligations. Four more syntheses were carried under identical conditions except for variations in the type of ligands. It is of particular importance that the TOP used in all of these syntheses were from the same bottle. A method very similar to the synthesis method explained above was used for these four syntheses. The molar ratios of gallium to selenium and the concentration of gallium and

selenium precursors were kept constant and equal to the ratios and concentrations of synthesis A. In the first of these 4 syntheses, synthesis B, again 3.5% ODPA was used but this time it was not heated for 12 hrs. In synthesis C and D, 3.5% DOPA and 33% TOPO were used, respectively. In synthesis E, our control synthesis, the reaction was run in pure TOP and there were no additional ligands present.

Extensive ^{31}P NMR and GC-MS measurements were performed on these ligand solutions. Hui Zhu, a graduate student in Dr. Matt Meyer's group, an organic chemistry faculty at UC-Merced kindly performed the NMR runs. Dr. Jaramillo-Fellin, the physics and chemistry laboratory coordinator kindly authorized our use of the GC-MS. The data hint at the formation of a relatively heavy molecule in the heated ODPA precursor that is absent in the non-heated sample. Phosphonic acid anhydride is a plausible candidate but unfortunately, exact assignment of some NMR and GC-MS peaks were not achieved. Regardless of this issue, the heated ODPA sample has a peculiarly clean and peakless NMR and GC-MS spectra with almost only the anhydride peak left. Most of the peaks that are present in the non-heated sample are gone. This might mean that the lighter phosphorous containing molecules are turned into anhydrides. Even after few cycles of purification, TOP and TOPO tend to have a lot of impurities in them, which are mostly phosphorous containing molecules, the most common ones being phosphines, mono- and di- phosphonic, and phosphinic acids. The equilibrium between TOP, TOPO and these impurities can be easily perturbed by slightest addition of phosphorous containing molecules, oxygen, or thermal effects. Buhro *et al.* does an excellent job of mapping out these equilibria in his publications on beneficial and harmful impurities of TOPO that influence particle synthesis[21,22]. Determining the exact nature and composition of molecules in the various ligands solutions is an intensely laborious project that is beyond the instrument capabilities of the lab,

and certainly beyond the scope of this dissertation.

Table 1: Quantum Yield of GaSe Particles with Various Ligations.

	Quantum Yield
Synthesis A (3.5% ODPA + heating)	11.2 %
Synthesis B (3.5% ODPA)	12.4 %
Synthesis C (3.5% DOPA)	13.8 %
Synthesis D (33% TOPO)	8.25 %
Synthesis E (TOP only)	7.1 %

Figure 10 and Figure 11 provide a comparison between the absorption and emission spectra of all of these five syntheses. A heated 3.5% ODPA precursor results in the most concentrated and aggregated sample, consistent with the NMR and GC-MS data. It also seems that, in comparison to our control synthesis E which is run in only TOP, addition of DOPA or ODPA with no heating only diminishes the quality of particles. Quantum yield measurements of each synthesis are provided in Table 1.

At this point, it is of some significance to discuss a rather unusual phenomenon that was observed in some GaSe syntheses. GaSe has been synthesized in Dr. Kelley's group for over six years. Traditionally, it used to be that the progress of the synthesis was monitored by taking absorption spectra of frequent aliquots taken during the reaction. Although, most of the reactions were run for approximately 90 minutes, what ultimately determined the shut-down time for the reaction was the absorption spectrum. When the absorption spectrum was either, not evolving

anymore (i.e. reaction was out of source precursors and particles reached the end of their growth), or hinting at "oswalt ripening", the reaction would be shut down. It has been a well-known matter that the particle solution remained optically clear throughout the whole reaction. However, starting early 2007, some syntheses would go turbid at some time-point during the reaction and hence, since we couldn't measure absorption spectra, there was no control over the progress of the reaction. We call these syntheses "blind". Above that, it is also seen that sometimes, although clear throughout the reaction, the particle solution goes foggy or slightly turbid after shut-down. In case of a blind synthesis, the reaction is allowed to run for the usual 90 minutes. After shut down, particle solution is centrifuged (in centrifuge tubes that have been previously pumped and filled with nitrogen gas) to obtain a clear supernatant containing the GaSe nanodisks. The nature of the precipitate at the bottom of the centrifuge tube varies from synthesis to synthesis. Sometimes, it consists of a white solid, a light yellow solid, a deep yellow gel (sometimes optically clear), or a combination of some or all of these. To this date, the exact nature of these precipitates and the exact cause of why some syntheses become blind are unknown to the group. One speculation is that they are tiny nucleation centers that have never reacted further to grow big particles. They are also probably unligated, which causes them to agglomerate irreversibly and thus, become insoluble in TOP and lead to the turbidity of the reaction mixture. Deborah Lair, a fellow graduate student in Dr. Kelley's group has delved deep into the science and behavior of these nucleation centers[23].

To relate this discussion to the five reported syntheses above, it seems that the heavier ligated syntheses are less prone to develop any turbidity attributed with the nucleation centers. This supports the idea that the nucleation centers are un-ligated and therefore precipitate out of solution. For example, synthesis D, in which the highest concentration of ligand is used (33% of

TOPO), remained crystal clear all throughout and after the reaction. Synthesis A became "blind" only after 75 minutes of reaction time while synthesis B was sort of turbid from early on but it was not "blind" in the sense that absorption spectra could still be measured. Even though syntheses A and B both contained 3.5 % ODPA, we strongly suspect that heating of the ODPA prior to synthesis A produces a higher amount of PA anhydrides in comparison to synthesis B. Presence of a higher amount of the strongly binding PA anhydrides in the reaction probably prevents the nucleation centers to fall out of solution, thus is responsible for the fact that synthesis A remains clear for a longer time. Synthesis C and E were both blind, though synthesis C seemed to produce the highest amounts of the precipitate. This explains the fact that it had the lowest amount of absorbance among all five samples (Figure 10). As a whole, DOPA can be considered the least effective ligand.

Experience with GaSe particle synthesis in the past years has shown that a TOP-only synthesis should not produce good particles. Rather, it produces dilute particles with a maximum absorption of about 0.6 at 410 nm, with minimal peak to valley ratio. Peak to valley ratio is a measure of the aggregation of the particles. However, as seen in Figure 10, this particular TOP-only synthesis produces rather very good particles. The group used to make wonderfully aggregated GaSe particles following TOP-only protocols before 2007 (Figure 7, sample 1). In the past few years, we realized that the same synthesis protocol produces very different particles when different bottles of TOP are used. In other words, the content of the TOP varies from bottle to bottle. The TOP used in the syntheses is always carefully vacuum-distilled, the lower boiling point components are discarded, and the higher boiling points components are left behind. Every effort is made to keep the distillation oxygen-free by using Teflon sleeves and O-rings at the joints, and grinding source and receiving flasks to the vacuum distillation apparatus. In general,

since GaSe syntheses are very sensitive, details of the protocol are followed meticulously to ensure consistency and reproducibility of the syntheses. The only feasible explanation left is that the free radicals used in the process of synthesizing TOP are not thoroughly removed. Considering the fact that these free radicals are not removed by vacuum distillation either, they pose a serious problem in terms of keeping reaction conditions constant across different syntheses. In all the studies reported in this dissertation, it has been made sure that comparisons are correctly made between syntheses that used TOP from one bottle. Nonetheless, free radicals in TOP seem to play a critical role in the success of a synthesis. Other factors such as precursor concentration, reaction volume, and type of ligation can and do improve or diminish the quality of particles but what matters the most is the free radical concentration of TOP. Aside from the problem of synthesis reproducibility, a reliable method by which particles could be isolated, purified, and then redissolved in another solvent does not exist. It was because of this difficulty and the irreproducibility problems that the group abandoned the research on GaSe.

Chapter Three: Singlet/Triplet Reversal in Strongly Coupled GaSe Aggregates

3.1. Background.

First, GaSe nanoparticles were synthesized in the absence of tightly binding edge ligands following the synthetic method described in section 2.1. These particles are ligated primarily with TOP and TOPO ligands that are easily displaced by far less bulky dodecyl aldehydes (DDA). Ligand replacement results in nanoparticle aggregates in which the lowest energy optical transitions are strongly coupled, resulting in a large red shift of the absorption spectrum (about 2600 cm-1) and a reversal of the singlet and triplet states. The reversal of the spin states results in changes in the polarization spectroscopy and a dramatic decrease in the radiative lifetime. Specifically, the exciton singlet states are linear oscillators, and time-resolved fluorescence polarization spectroscopy gives an initial anisotropy very close to the linear oscillator limit of 0.4. The radiative lifetime of this fluorescence is about 12 ns, compared to about 82 ns for the monomers. Upon aggregation, the fluorescence quantum yield increases from 4.7 to 61%. This chapter will discuss the details of the static and transient spectroscopy of these DDA-treated particles.

Whereas previous scientific literature have elucidated much of the structural, spectroscopic, and dynamical characteristics of as-synthesized GaSe aggregates, they have not addressed the spectroscopy of more strongly coupled aggregates and, specifically, have not addressed the relative roles of singlet and triplet states in the spectroscopy. Electromagnetic

(dipolar) coupling mixes transitions on adjacent particles having the same polarization and comparable energies. The extent of the coupling depends on the intensity of the transitions. The lowest singlet-singlet transition is allowed in GaSe nanoparticles, resulting in relatively strong coupling between the singlet states on adjacent particles. Since the triplets have a far smaller oscillator strength, they are only weakly coupled. Unlike most organic molecules, the GaSe singlet states are at only slightly higher energy than that of the triplets, 16 cm^{-1} in bulk GaSe[24]. This is far less than the typical interparticle coupling (300 cm^{-1}), and one might, therefore, expect that interparticle coupling could lower the singlets below the triplets. However, this does not occur in any of the GaSe aggregates previously reported. The reason is that the magnitude of the coupling is smaller than the inhomogeneous width of transition energies (about 1000 cm^{-1}), and the coupled aggregate singlet states are interspersed with the triplets. The three-fold degeneracy of the triplets means that, following equilibration, only about one-fourth of the population is in the strongly fluorescing singlets. This is the same as in the GaSe nanoparticle monomers, and the difference in singlet and triplet interparticle interactions does not result in large spectroscopic effects in the previously-studied aggregates. These effects should become apparent only when the magnitude of the interparticle coupling becomes comparable to the energetic inhomogeneity.

The magnitude of the interparticle dipolar coupling is strongly distance dependent. The particles are very thin disks and, in principle, can get very close to each other. The interparticle distance in these aggregates depends primarily on the size of surface ligands. Since the disk-like particles have gallium atoms exposed at the edges, the metal-binding ligands are attached exclusively at the particle edges. The nature and density of these ligands can be controlled by the surface chemistry of the particles. In this chapter, it will be shown that replacing the usual ligands with less bulky ones dramatically increases the interparticle coupling. This coupling

between the singlet states is larger than the inhomogeneous width and, therefore, results in lowering the allowed singlet states below the triplets. As a result, essentially all of the equilibrated population is in the delocalized singlet excitons. The effect of this is to greatly increase the effective radiative rate and fluorescence quantum yield and alter the polarization spectroscopy.

3.2. Static Spectroscopy.

The absorption onsets of GaSe nanoparticle monomers are size-dependent, due to quantum confinement. These size-dependent spectra have been characterized by electron microscopy, and it is possible to determine particles' sizes from these spectra9. The absorption spectra indicate that this type of anhydride-free synthesis typically gives particles having diameters of 5-6 nm. Dodecanal is then added to this solution, 3% by volume. A simple calculation indicates that this is somewhat more than enough to bind all of the edge gallium atoms in the nanoparticle solution. The solution has an immediate color change and, under fluorescent room lights, becomes obviously intensely fluorescent. The spectrum continues to evolve for several hours, after which it is stable for days to weeks. Eventually, bulk GaSe will precipitate out of solution. The absorption and fluorescence spectra of the particles before and after addition of DDA are shown in Figure 12 and Figure 13. The as-synthesized particles may be diluted (typically by a factor of 10) in a tributylphosphine/TOPO solution to obtain nanoparticle monomers. The above solutions are used for the static and time-resolved spectroscopic studies reported here. These same GaSe monomers and DDA-treated GaSe aggregates were also provided to Dr. Tao Ye's group at UC-Merced, where they were successfully oriented on a gold surface[25]. The surface chemistry of particles determines the surface-stabilized stacking of the disks.

Instrumentation. Static fluorescence spectra were obtained using a Jobin-Yvon Fluorolog-3 spectrometer, with a xenon lamp and double monochromator excitation source and a CCD detector. The spectra are corrected for instrument response, using correction curves generated from the spectrum of a Optronix spectrally calibrated lamp. The spectrum of the excitation source is determined by scattering from a BaSO4-coated microscope slide. Quantum yields are determined by comparison of the nanoparticle spectra with the spectrum of rhodamine 6G, with the appropriate spectral calibration factors. Time-resolved measurements were obtained by time-correlated photon counting, using a Becker & Hickel SP-630 board. The detector is a Hamamatsu red-enhanced 6 μm microchannel plate PMT. The light source used to obtain the 410 and 430 nm excitation results is a cavity-dumped Ti:sapphire laser (Coherent Mira), with a 1 MHz repetition rate. The light source for the 460 nm excitation results is a Spectra-Physics Tsunami operating in picosecond mode with a repetition rate of 80 MHz. In all cases, the fluorescence is focused through a 0.25 m monochromator with a 150 groove/mm grating and onto the microchannel plate PMT. Polarized detection is accomplished with a Polaroid film, following fluorescence collection. The monochromator has a polarization scrambler in front of the entrance slit, which almost completely eliminates the polarization dependence of the monochromator throughput. A small correction to the polarization-dependent monochromator throughput is determined from the long-time (>5 ns) fluorescence of a coumarin dye in methanol, which is taken to be isotropic.

Figure 12 shows the absorption spectra of particles obtained directly from the synthesis, diluted by a factor of 10 to obtain monomers, and following the addition of 3% dodecanal. Comparison of these spectra shows that the monomers and the as-synthesized, comparatively weakly aggregated particles both have maxima in the 400-410 nm region. Addition of dodecanal

shifts the absorption onset and the absorption maximum about 2600 cm^{-1} to the red (407 to 455 nm). This shift is assigned to the absorption of strongly interacting GaSe nanoparticle aggregates. Both the as-synthesized and, especially, the diluted samples also show weak shoulders in the 430-460 nm spectral region, which are also assigned to a low concentration of these aggregates. The magnitude of this shoulder in the diluted sample diminishes with time as the particle aggregation approaches equilibrium. These spectra, therefore, indicate that strongly-coupled aggregates are always present at low concentrations and are the dominant species following the addition of dodecanal. Figure 13 shows fluorescence spectra of the same samples. The fluorescence of the dodecanal sample is considerably red shifted and much more intense than that of the as-synthesized or diluted samples. These spectral differences can be understood in terms of the particle surface chemistry and the resulting aggregate formation.

The surface chemistry of GaSe nanoparticles is controlled by the chemistry of the reaction mixture. Recall that the TOP/TOPO reaction mixture is prepared from tech-grade TOP and TOPO, which are purified by vacuum distillation. The surfaces of these two dimensional particles are unreactive, and the ligands are believed to attach to the edges where gallium atoms are exposed. It was long believed that TOP and, especially, TOPO were the primary ligands on the particle edges. This is also the case in the synthesis of CdSe nanoparticles. However, the chemistry of TOP/TOPO mixtures is surprisingly complicated, and recent studies have shown that, in the CdSe case, other species are typically the surface ligands[21,26,27.] A similar situation is found here. We used ^{31}P NMR and GCMS to study the chemistry of these mixtures that occurs upon distillation in an imperfect vacuum. The TOP/TOPO mixtures are particularly complicated (much more complicated than tech-grade TOPO alone) and were discussed in detail in section 2.3. One of the plausible conclusions is that, upon distillation and under reaction conditions,

TOP/TOPO mixtures produce anhydrides of octylphosphonic acid. These are strongly binding ligands that coordinated the edges of the GaSe nanoparticles in most of our previous syntheses (prior to 2007). These bulky bi- or polydentate anhydride ligands bind strongly to the particle edges and keep the particles from getting closer together, thereby limiting the extent of interparticle coupling. These ligands are not easily displaced, and the subsequent addition of alkyl aldehydes has little effect on the particle absorption or fluorescence spectra as was shown in Figure 9.

Synthesis in higher purity TOP (containing very little TOPO and, essentially, no anhydrides) changes the rates of nucleation and growth, as well as the surface chemistry of the particles. In this case, the reaction produces smaller particles, typically 5-6 nm. The absence of these stronger binding ligands also results in particles ligated with the much weaker binding TOP and TOPO ligands. These ligands are easily displaced by the far less bulky alkyl aldehydes. As shown in Figure 12, addition of a few percent of dodecanal shifts the lowest energy transition to longer wavelengths, indicating the presence of very strongly interacting aggregates. The fluorescence from the dodecanal-ligated particles is much more intense than from the TOP/TOPO-ligated particles (or from previously reported anhydride-ligated particles), indicating a dramatic increase in the fluorescence quantum yield (see Figure 13). The fluorescence quantum yield in both the dodecanal and as-synthesized aggregates depends on the excitation wavelength, and quantum yields are given in Table 2. This excitation wavelength dependence is due to two types of inhomogeneity. First, there is a finite distribution of particle sizes, and the larger particles absorb further to the red. Larger particles are known to have higher fluorescence quantum yields[4,6]. Second, more strongly coupled particles absorb further to the red, resulting in more delocalized excitons. Thus, the red-absorbing sections of the aggregates exhibit more

superradiance and, hence, have larger fluorescence quantum yields[28].

Table 2: Fluorescence Maxima and Quantum Yields at Different Excitation Wavelengths.

Excitation Wavelength	With Dodecanal	As-synthesized	Monomers
410	503 nm, 27%	476 nm, 14%	473 nm, 5%
430	506 nm, 44%	499 nm, 25%	
445	507 nm, 54%		
460	509 nm, 61%		

Table 2 also shows that, in general, the λ_{max} values of the fluorescence spectra are excitation wavelength dependent. This is particularly true for the as-synthesized particles because of the inhomogeneities mentioned above. However, in the case of the dodecanal aggregates, the λ_{max} value of the fluorescence spectrum is a much weaker function of excitation wavelength. This indicates less inhomogeneity and rapid relaxation to similar emitting states, independent of the photoselected state. Exciton relaxation processes will be discussed in terms of the time-resolved results.

3.3. Time-Resolved Anisotropy.

The absorption and fluorescence from lowest excited (band-edge) state is largely, but not completely polarized along the z-axis of the particle. The extent of polarization can be characterized in terms of the fluorescence anisotropy, given by

$$r = \frac{I_{par} - I_{perp}}{I_{par} + 2I_{perp}}$$

The fluorescence can be depolarized by electronic relaxation from the band edge into trap states. These trap states derive oscillator strength from both z- and x,y-polarized transitions and give rise to nearly isotropic fluorescence. The static fluorescence has contributions from both trapped and band edge states and therefore reflects an average of both types of fluorescence. This is, in part, why the fluorescence spectra in Figure 13 are relatively broad. The band edge fluorescence anisotropy can be assessed from a time-resolved measurement. Specifically, the anisotropy immediately following excitation (prior to electron or hole trapping) is characteristic of the band edge states. Figure 14 shows that the anisotropy of GaSe monomers immediately ($<$ 50 ps) following excitation with linearly polarized light is about 0.33. Similar values have been previously reported[7] and are also obtained from the as-synthesized aggregates. This anisotropy can be understood in terms of transitions to the allowed singlet state and nominally forbidden triplet states. The transition to the singlet state is z polarized. The transitions to the $m_l = \pm 1$ triplet states obtain x,y-polarized oscillator strength through spin-orbit coupling to the higher energy, allowed (x,y-polarized) state[29,3]. The $m_l = 0$ triplet state is dark. These states and transitions are depicted in Figure 15. The role of the triplets in the fluorescence anisotropy depends on the rate of singlet/triplet population equilibration. Two possibilities can be considered: equilibration is fast and the initial ($t \leq 50$ ps) fluorescence anisotropy reflects a Boltzmann distribution of these populations, and equilibration is slow, occurring on a timescale longer than 50 ps. The second possibility is excluded by the following considerations. In the case of four states, a z-polarized singlet and three triplets (two being x,y polarized and the other being dark), the fluorescence anisotropy before and after equilibration of the different levels can be calculated in terms of the fraction, f_s, of the oscillator strength in the singlet transition. That is,

the singlet has a relative absorption or emission intensity of f_s and each of the spin-orbit allowed

x,y-polarized triplet sublevels has a relative intensity of $(1-f_s)/2$. Ignoring the small difference in

wavelengths, this may be written in terms of the singlet and triplet radiative rates, $f_s = k_{rad, \, singlet}$

$/(k_{rad, \, singlet} + k_{rad, \, triplet})$. Prior to relaxation, the total emission intensity is $I = f_s^{\,2} + (1-f_s)^2$. The

observed anisotropy is the fraction of light coming from each transition, multiplied by its

anisotropy. Linear and planar oscillators give anisotropies of 0.4 and 0.1, respectively. Therefore,

when no relaxation has occurred, $r = 0.33 = \{0.4 \, f_s^{\,2} + 0.1 \, (1-f_s)^2\}/I$. We get that $f_s = 0.65$. This

is a very low value, and one that is not consistent with measured absorption intensity ratios for

bulk GaSe. It is also not consistent with the previously reported polarized absorption

measurements on aligned GaSe nanoparticles in liquid crystals[30]. We conclude that the

anisotropy value of 0.33 does not correspond to unrelaxed singlet and triplet levels, and that

relaxation among the triplet and singlet levels occurs in considerably less than 50 ps. The singlet-

triplet splitting (16 cm^{-1} for bulk GaSe) is small compared to thermal energies at room

temperature (210 cm^{-1}). A somewhat larger value is expected in the case of GaSe monomer

nanoparticles, due to quantum confinement effects. However, the exchange integral is expected

to scale roughly as the ratio of the exciton Bohr radius to particle size. This consideration

suggests that the singlet-triplet splitting will also be much smaller than room temperature thermal

energies in GaSe nanoparticles. We conclude that following fast relaxation, the singlet and triplet

levels are close to equally populated. In this case, the anisotropy is given by: $r = 0.33 = 0.4(f_s^{\,2} - f_s$

$(1-f_s)) + 0.1(1-f_s)^2$ and we get that $f_s = 0.93$. Otherwise stated, the conclusion is that about 93%

of the oscillator strength is in the z-polarized singlet and about 7% is in the x,y-polarized triplets.

It is possible to assess the roles of the singlet and triplet states in the fluorescence from

dodecanal-ligated aggregates from time resolved anisotropy measurements. The 460 nm

polarized fluorescence kinetics are obtained using an 80 MHz repetition rate light source, and the polarized fluorescence kinetics are somewhat complicated by the fact that when an excitation pulse arrives, fluorescence from the previous pulse has not completely decayed. This can be corrected for by a deconvolution procedure, presented in Appendix A: Deconvolution Procedure for Correcting Fluorescence Kinetics. With appropriate approximations, this procedure amounts to subtracting off the respective slowly decaying parallel and perpendicular fluorescence components obtained prior to pulse arrival. Properly corrected anisotropy decays are shown in Figure 14, and an initial fluorescence anisotropy of 0.39 is measured. This is very different from the 0.33 value observed for the GaSe monomers, and very close to the pure linear oscillator limit of 0.40. This is a definitive and remarkable result. It clearly indicates that in the case of the dodecanal-ligated aggregates, the singlet states are below the triplets, and are selectively excited by 460 nm light. This is the situation depicted for the case of a dimer in Figure 15.

3.4. Model for Aggregate Excitons.

We propose that the photoexcited excitons in these aggregates may be described in terms of a simple dipolar coupling model that includes both diagonal (energetic) and off-diagonal (coupling) disorder. A similar model, lacking off-diagonal disorder, was used to model the spectroscopy of the as-synthesized aggregates4[,11] and aggregates of GaSe nanoparticle produced by a low temperature synthesis[28]. The z-polarized transition is modeled as a one-dimensional array of oscillators with nearest neighbor dipolar coupling. In the present case, the monomers are taken to have an inhomogeneously broadened absorption centered at 400 nm, with a Gaussian width (standard deviation) of 1000 cm^{-1}. These values are obtained from fitting the monomer absorption spectrum. The mean and standard deviation of the off-diagonal elements are the only two adjustable parameters of the model. These interparticle couplings are taken to be a Gaussian

distribution centered at 1930 cm^{-1} with a standard deviation of 2300 cm^{-1}. Thus the matrix describing the energies and interparticle interactions of a section of the aggregate has diagonal elements ($C_{i,i}$) chosen randomly in a 25000 ± 1000 cm^{-1} distribution and off-diagonal elements ($C_{i,i+1}$ and $C_{i+1,i}$) chosen randomly in a -1930 ± 2300 cm^{-1} distribution. Diagonalization of this matrix gives the absorption spectroscopy of that aggregate. The eigenvalues are the exciton energies and the eigenvectors give the contribution of the individual particle states to that exciton. Thus, the *i*'th excited state is given by

$$\Psi_i = c_{i,1}\,\varphi_1{}^*\varphi_2...\varphi_n + c_{i,2}\,\varphi_1\varphi_2{}^*...\varphi_n + ... + c_{i,n}\,\varphi_1\varphi_2...\varphi_n{}^* \qquad \text{Equation (1)}$$

The eigenvector coefficients permit calculation of the relative oscillator strength of that exciton state. Specifically, the oscillator strength of a monomer is proportional to the square of the dipole moment operator, $\mu^2 = |{<}\varphi|\boldsymbol{\mu}|\varphi^*{>}|^2$, where $\boldsymbol{\mu}$ is the dipole moment operator and is assumed to be the same for all of the particles. The oscillator strength of each aggregate eigenstate is a very simple expression in terms of μ^2, given in equation 2.

$$\left|\left\langle \Psi_g \left|\boldsymbol{\mu}\right| \Psi_i \right\rangle\right|^2 = \left|\left\langle \varphi_1\varphi_2...\varphi_n \left|\boldsymbol{\mu}_1 + \boldsymbol{\mu}_2 + ...\boldsymbol{\mu}_n\right| \sum_j c_{i,j}\varphi_1\varphi_2..\varphi_j{}^*..\varphi_n \right\rangle\right|^2 = \mu^2 \left|\sum_j c_{i,j}\right|^2 \qquad \text{Equation (2)}$$

All of the eigenstates and their oscillator strengths are used to construct the absorption spectrum of that aggregate. The total absorption spectrum is obtained from summing up many of these (randomly) calculated spectra. The results of this calculation are shown in Figure 16. Using these parameters, the z-polarized part of the absorption spectrum ($\lambda > 400$ nm) is fit quite well. The short wavelength part of the spectrum ($\lambda < 400$ nm) is dominated by the x,y-polarized transition and no attempt is made to fit this region. The only part of the $\lambda > 400$ nm spectrum that is not accurately described by the model is the shoulder at 500 – 520 nm. This feature is absent immediately after the sample is made, and grows in as the sample ages. It is probably due to a different phase of the aggregates that is in the process of forming bulk GaSe. This feature is not

excited by 460 nm light and it will not be considered further. The parameters used to obtain this fit are noteworthy. The coupling is much larger than in the case of the as-synthesized aggregates. However, the standard deviation of these couplings is very large, larger than the median value. The calculations therefore indicate that the aggregates have a lot of disorder in the coupling strengths. The magnitude of the coupling depends on the magnitude of the transition dipole, which depends on the particle size. Some of the coupling disorder is due to the finite particles size distribution. However, the following considerations suggest that this is not a major source of coupling disorder. Similar particles have been characterized by TEM imaging and have a size distribution of about ± 8%. The present synthesis results in a very slightly broader absorption and are somewhat more polydisperse; ± 10% is a realistic estimate. The magnitude of the transition dipole scales roughly with the particle volume, and therefore has variability on the order of ± 20%. The magnitude of interparticle dipole-dipole couplings depends on the transition dipoles of adjacent particles and its variability of is expected to be somewhat larger than 20%. However, this is much smaller than the calculated variability of greater than ± 120%, and we conclude that particle size distribution is a minor source of the off-diagonal disorder. Most of the off-diagonal disorder must be due to structural disorder in the aggregate. The large magnitude of this disorder has implications for the fluorescence characteristics of the aggregates, discussed below.

3.5. Radiative Rates and Coherence Lengths.

In addition to the anisotropy results, the total (wavelength-integrated) fluorescence decays are obtained from the time-resolved results. From the total fluorescence decays and quantum yields, it is possible to determine the initial (band edge) radiative and non-radiative rates. The case of the dodecanal-ligated nanoparticles following 460 nm excitation is particularly simple; the fluorescence kinetics closely follows a single exponential decay. (We will discuss the

significance of the single exponential decay in connection with exciton relaxation, later.) The decay time is 7.42 ns and the fluorescence quantum yield is 61%. The quantum yield and decay times are related by: $\Phi = 0.61 = k_{rad}/(k_{rad} + k_{nr})$, with $(k_{rad} + k_{nr}) = (7.42 \text{ ns})^{-1}$, where k_{rad} and k_{nr} are the radiative and non-radiative rates, respectively. We get that $k_{rad} = (12.2 \text{ ns})^{-1}$ and $k_{nr} = (18.9 \text{ ns})^{-1}$. Similar considerations apply to the monomers. The fluorescence quantum yield for the monomers following 410 nm excitation is 4.7%. In the case of the monomers, there is significant inhomogeneity in the particles, resulting in more complicated decay kinetics. These kinetics can be fit to a biexponential decay having 1800 ps (49%) and 5700 ps (51%) components, similar to the decays previously reported.[8] The monomer band edge radiative rate (t = 0) can be obtained from the comparison with the aggregate decay curve and quantum yield, assuming that the non-radiative decay rates in the monomers and aggregates are the same. This is almost surely a good assumption; the main difference between the monomers and aggregates is the spin state. Non-radiative recombination is preceded by carrier trapping and the rates of carrier trapping are not expected to depend on whether they form a singlet versus triplet spin states. Comparing the monomers and aggregates, the radiative rates and quantum yields are related by

$$\frac{\Phi_{mon}}{\Phi_{agg}} = \frac{.047}{.61} = \frac{k_{rad,mon}}{k_{rad,agg}} \frac{\left((0.49)1800\,ps + (0.51)5700\,ps \right)}{7420\,ps}$$

This gives $k_{rad,agg}/k_{rad,mon} = 6.8$, or the radiative lifetime of the monomers is about 82 ns. The ratio of oscillator strengths is related to the ratio of radiative lifetimes by a factor of υ^3. The initial fluorescence maxima are at about 470 and 506 nm for the monomers and aggregates, respectively. Considering this factor gives a ratio of oscillator strengths of 8.5.

The larger radiative rate of the aggregates is due to two factors: the larger population in the singlet states and the coupling of singlet states on adjacent particles, i.e., the finite coherence

47

length of the exciton giving rise to superradiance. In both monomer and aggregate cases, the net radiative rates depend on the singlet and triplet populations and radiative rates. Specifically, we have

$$k_{rad} = P_S \, k_{rad,singlet} + P_T \, k_{rad,triplet}$$ Equation (3)

where the singlet P_S, and total triplet P_T, populations are given by a Boltzmann distribution and $k_{rad,singlet}$ and $k_{rad,triplet}$ and the singlet and triplet radiative rates. The population factors are given by

$$P_S = \frac{\exp(-\Delta E_{ST}/kT)}{3 + \exp(-\Delta E_{ST}/kT)} \text{ and } P_T = 1 - P_S.$$ Equation (4)

The factor of 3 comes from the fact that there are three essentially degenerate triplet states, and P_T is the total triplet population. As discussed above, the singlet-triplet splitting in GaSe nanoparticle monomers, ΔE_{ST}, is much smaller than thermal energies at room temperature. Thus, in the case of the monomers the Boltzmann factor, $\exp(-\Delta E_{ST}/kT)$ is expected close to unity. The anisotropy measurements discussed above indicate that 93% of the oscillator strength is in the singlet and a total of 7% in the triplets. Thus, the oscillator strength of each of the $m_l = \pm 1$ triplet levels is a factor of 26.6 lower than that of the singlet and the $m_l = 0$ is dark. We conclude that an equilibrated population in the monomers has very close to equal populations in each of the singlet and triplet levels; that is, only about ¼ of the population is in the strongly fluorescent singlet state, one-half is in the weakly emitting $m_l = \pm 1$ triplets and ¼ is in the dark $m_l = 0$ triplet. In contrast, in the case of the aggregates, the coupling of the singlet states lowers their excitation energy from about 406 nm to about 455 nm, and ΔE_{ST} in equation 4 is a large negative number, about -2600 cm^{-1}. As a result, in the case of the aggregates, the Boltzmann factor, $\exp(-\Delta E_{ST}/kT)$, is very large and the coupled singlets have essentially all of the population; $P_S \approx 1$ and $P_T \approx 0$ in equation 3. Applying equation 3 to both monomers and to the aggregates, a ratio of radiative

rates can be calculated. Thus, considering only the relative singlet and triplet populations (and assuming constant singlet and triplet radiative rates), a factor of 3.5 in the net radiative rate results from the change in populations associated with the reversal of the singlet and triplet states. Including the υ^3 factor obtained from the initial fluorescence maxima, the population change and spectral shift together give an oscillator strength ratio of 4.4. This does not match the observed ratio of oscillator strengths, 8.5. The other factor of 1.9 (= 8.5/4.4) comes from the coupling of the singlet oscillators, the superradiance. This factor of 1.9 is the coherence length of the exciton which undergoes fluorescence. Otherwise stated, following 460 nm excitation and any fast (<30 ps) relaxation, the exciton is delocalized over on average about two nanoparticles.

The large red shift of the absorption and fluorescence maxima of the dodecanal aggregates compared to the monomers suggests that the interparticle coupling is very large, on the order of thousands of wavenumbers, and this is borne out by the coupled oscillator calculations described above. The interparticle coupling is considerably larger than the energetic inhomogeneity of the particles, and one might expect this large coupling to result in very long coherence length aggregates. However, the above analysis of the radiative rates indicates a very short coherence length – about 2 particles, a dimer. We suggest that these results may be understood in terms of a simple dipolar coupling model and fast relaxation processes of the exciton.

3.6. Exciton Relaxation.

The above model also permits calculation of the coherence length and the fluorescence oscillator strength. This calculation is complicated by electronic and structural relaxation. We first consider electronic relaxation. The initially excited state can be taken to be the eigenstate closest in energy to the energy of the excitation photon, in this case, 460 nm. This state is a

coherent superposition of monomer excited states and following equation 1, can be denoted as

$$\Psi_{init} = c_1\,\varphi_1{}^*\varphi_2...\varphi_n + c_2\,\varphi_1\varphi_2{}^*...\varphi_n + \,...\, + c_n\,\varphi_1\varphi_2...\varphi_n{}^* \qquad\qquad \text{Equation (5)}$$

Following photoexcitation, the exciton can undergo rapid electronic relaxation, specifically an "internal conversion", corresponding to dephasing of the initial coherent superposition. In a room temperature bath, this results in energy loss and is irreversible. A state that has undergone only electronic dephasing has the same amplitude on each of the monomers as the initially excited state. Thus, this is a non-diffusive relaxation that occurs without any overall motion of the exciton. In room temperature solutions, dephasing is expected to be rapid, $<$ 30 ps. The results presented here focus on radiative lifetime measured about 50 ps after excitation, which is fast compared to exciton diffusion. Spectral reconstruction results show that exciton diffusion occurs on a slower timescale (refer to section 3.7). We conclude that the radiative rate measurements presented here correspond to states that are electronically relaxed, but have not undergone significant exciton diffusion.

Excitons corresponding to both the initially excited and electronically relaxed states can be described in terms of the c_j coefficients in equation 5. The oscillator strength and energy of the initially excited state (and every other exciton state) depends on the magnitudes and relative signs of the coefficients. The coefficients in general, will not all have the same sign. Spectroscopic considerations allow us to make very general statements about how the oscillator strengths of these states vary with energy. The transition to the lowest energy state for these particles is z-polarized. Particle stacking is in the z-direction and results in a J-aggregate; the lowest energy state has the dipoles pointing in the same direction and the coefficients all have the same sign. In the present case, 460 nm photoexcitation is close to the center of the aggregate absorption band. Thus, in contrast to lowest energy states, the initially excited state will generally

have coefficients of different signs. Following excitation, the exciton does not move to different particles in the aggregate, that is, purely electronic relaxation corresponds to keeping the same amount of excitation on each of the particles. For this to occur the magnitudes of each of the coefficients in equation 5 remain constant and this relaxation only changes the signs of the coefficients. Specifically, the electronically relaxed state is given by

$$\Psi_{rlx} = |c_1| \, \varphi_1{}^*\varphi_2...\varphi_n + |c_2| \, \varphi_1\varphi_2{}^*...\varphi_n + \ ... \ + |c_n| \, \varphi_1\varphi_2...\varphi_n{}^* \qquad \text{Equation (6)}$$

where the c_j coefficients are the same as in equation 5. It is important to note that dephasing changes the coefficients in equation 5 and therefore also changes the oscillator strength of the exciton. This relaxed state is not an eigenfunction of the coupling Hamiltonian, but can be expanded in the basis set of these eigenfunctions. This relaxed state is a superposition of the aggregate eigenstates and the expansion coefficients are given by

$$a_i = \left\langle \Psi_{rlx} \middle| \Psi_i \right\rangle = \sum_j \left| c_j \right| c_{i,j} \qquad \text{Equation (7)}$$

where the coefficients $c_{i,j}$ correspond to those in equation 1. The oscillator strength of this superposition relative to that of a monomer is given by

$$f = \left| \left\langle \Psi_g \middle| \mathbf{\mu} \middle| \Psi_{rlx} \right\rangle \right|^2 = \mu^2 \sum_i a_i \left| \sum_j c_{i,j} \right|^2 \qquad \text{Equation (8)}$$

where the subscript g indicates the ground state, $\mathbf{\mu}$ is the dipole moment operator (see equation 2) and the a_i coefficients are given by equation 7. This result allows the evaluation of the relative oscillator strength, that is, the superradiance of the relaxed aggregate following electronic relaxation but prior to structural relaxation or exciton diffusion. It is important to note that once the monomer and aggregate absorption spectra are fit, there are no further adjustable parameters in this calculation. The extent to which electronic relaxation changes the oscillator strength of the fluorescent states depends on the excitation wavelength. We find that for 460 nm excitation and

51

the same parameters as were used to fit the absorption spectrum, the calculated oscillator strength of the initially excited state is 3.0 times that of the monomer. Electronic relaxation increases this oscillator strengths ratio to 3.8, as per equation 8. This is the calculated exciton coherence length and is significantly greater than the value of 1.9 determined from the comparison of monomer and aggregate radiative lifetimes and quantum yields. The conclusion is that this coupled-dipole model alone does not explain the observed short coherence length of the exciton luminescence.

We suggest that in addition to electronically relaxation, the excitons also undergo rapid structural relaxation. Prior to photoexcitation, the distances between particles are determined by the balance between attractive van der Waals forces and repulsive steric interactions from the edge-binding ligands. The extent of coupling between any two particles depends critically on the distance between them. If the coupling is sufficiently strong, the presence of the exciton affects the balance of these forces. Two particles will be pulled together if the increased exciton stabilization energy exceeds energetic cost due to particle-particle steric repulsion. We suggest that this occurs in the case of the aldehyde-ligated particles. Following photoexcitation and electronic relaxation, the exciton resides on an average of 3.8 particles. The two most strongly coupled particles on which the exciton resides are drawn together, increasing the coupling between these particles. This motion increases the distance between those two particles and their other neighbors, so this increase in coupling occurs at the expense of lowering the other couplings. This process amounts to exciton self-trapping. It occurs as a result of the interaction of the excitation and the particles longitudinal displacements, i.e., the of electron-phonon coupling. The effect of this process is to turn a delocalized exciton into what is spectroscopically a very strongly coupled dimer. We note that when the exciton consistently collapses to a dimer, it forms

a rather well-defined spectroscopic entity – dimers have very little inhomogeneity. We suggest that this may explain why simple, single-exponential fluorescence decay kinetics are observed following 460 nm excitation of these aggregates.

3.7. Time-resolved Emission and Stimulated Emission in GaSe Aggregates.

Further characterization of the aldehyde-ligated aggregates was done by time-resolved emission spectroscopy and transient absorption experiments. A reconstruction of a curve of emission maxima as a function of time leads to some insight (Figure 17). Maximum emission peak for monomers shifts to the red by only 4nm within the first 4ns and it does not exceed 485nm. In contrast, the maximum emission in aldehyde-ligated aggregates shifts by about 20nm, eventually reaching a maximum value of about 520nm. The reality is that the aggregates are far from being perfect and straight: they have kinks, bends, non-linearities, and defect sites that inhibit the movement of the exciton. The length over which the exciton is delocalized is called the coherence length and it critically depends on how defect-free the aggregates are. The more kink-free the aggregates, the longer the coherence length. Initially, a photon creates an exciton and the exciton delocalizes over nearest kink-free neighboring particles. The amount of red-shift in the emission spectrum is a function of coherence length and the coupling strength between the particles. Thus, the time-resolved emission data presented in Figure 17 is an indirect qualitative measure of the combination of two independent factors: coupling and the coherence length. Following the discussion in previous sections of this chapter, we know that although a small percentage of longer aggregates exist in the solution, the red-shift in the emission spectrum is primarily due the strong coupling of dimers. The time-resolved data are still helpful in that they give us an idea about the timescales. Fitting the curve to a bi-exponential implies that there is a fast 200ps component and a slower nanosecond component to the dynamics of the exciton.

Another technique that can be utilized to characterize the aggregates is femtosecond transient absorption spectroscopy. Using a pump-probe technique and a delay stage, one can obtain information on time-dependent decay of the transient excited population. Figure 18 shows the transient absorption spectra for the GaSe monomers for the first 200ps after excitation. The positive change in absorbance in the red (peak at about 620nm) indicates the intraband hole transitions. Note that there is no bleach in the blue. The Figure also shows the spectra of the aldehyde-ligated aggregates for 200ps after excitation. In addition to the intraband hole transitions, there is a strong bleach in the blue hinting at stimulated emission. It has been shown that stimulated emission from the excitons leads to superradiance. Superradiance is the phenomenon where the coupled oscillators in an assembly cooperate to collectively emit light at a rate which is much greater than their incoherent emission rate. Relative measurement of the stimulated emission yields Einstein A and B values and therefore the excited state transition dipole moment. It is important to realize that one cannot obtain quantitative values from these experiments. The results qualitatively tell us about a combination of coherence length and coupling strength of aggregates. The data in this section are just presented to provide some extra insight on earlier material. Nonetheless, no rigorous attempt was made to collect further transient data.

In summary, several conclusions may be drawn from the results presented in this chapter. GaSe nanoparticles have aggregation properties that are strongly dependent on the nature of the surface (edge) ligands. In the present case, the TOP and TOPO ligating the particle edges are easily displaced by alkyl aldehydes, resulting in very strongly coupled aggregates. The strong dipolar coupling between adjacent particles results in delocalized singlet excitons that are energetically below the triplet states; polarization measurements indicate that singlet-triplet

reversal occurs in these aggregates. The radiative rates and fluorescence quantum yields in these aggregates are much greater than in the monomers. This is due to a combination of all the population being in the singlet states and the coupling of the singlet oscillators. The highly fluorescent aggregate state is essentially a nanoparticle dimer that results from self-trapping of the delocalized exciton.

Chapter Four: Alignment of GaSe Aggregates in Liquid Crystal Samples

4.1. Overview and Potential Applications of GaSe/Liquid Crystal Hybrid Samples.

This chapter discusses highly organized three-dimensional structures of strongly interacting semiconductor GaSe dots in liquid crystals. The development of organized arrays of these quantum dots could result in entirely new classes of optical materials. Liquid crystals (LCs) form a highly anisotropic and ordered environment. Most liquid crystals consist of long, rod-like organic molecules. These molecules are typically much more polarizable along their long axis, compared to the perpendicular direction. This results in birefringence when the molecules are aligned. When these molecules align in LC phases there is a well-defined preferred direction, and hence a well-defined birefringence. It has been demonstrated that liquid crystals can align low concentrations of guest molecules, for example carbon nanotubes[31] or sections of polymers[32,33]. The underlying idea is to use organic liquid crystals to organize aggregates of GaSe nanoparticles into well-defined three-dimensional structures. The structure of these nanoparticle aggregates is constrained by the structure of the surrounding organic liquid crystal (LC) phase. Thermotropic liquid crystals, such as 8CB, change phase with temperature changes. In a nematic phase, the long molecules of the LC have no positional order but have somewhat of a directional order that keeps the long axes of the molecules roughly parallel to each other. The LC molecules in smectic phases, which are formed at lower temperatures than nematic phases, have positional order and form well-defined layers. Otherwise stated, the presence of the organic nematic or

smectic phase forces the disk-like nanoparticles into a collinear and/or planar discotic liquid crystal phase. The discotic phase is formed when disk-like particles, in this case GaSe, pack into stacks. The entire system may be thought of as nematic/discotic or smectic/discotic hybrid liquid crystal composed of organic and semiconductor components. The nanoparticles in these structures have both orientational and three-dimensional positional order. As such, the optical and electronic properties of the hybrid organic/semiconductor liquid crystal are highly anisotropic and could be made to be spatially dependent. Furthermore, it should be possible to change the orientation of the hybrid liquid crystals by the application of an external electric field, just as it is in conventional organic liquid crystals. Application of an electric field will result in changing the orientation of the liquid crystal director field and hence the nanoparticle structures. In this sense, reconfigurable photonic devices based on hybrid liquid crystals could be fabricated. The combination of using semiconductor quantum dots as chromophores to collect photons and subsequently funneling energy through strongly-interacting structures of these quantum dots has many technological possibilities. These include the fabrication of very efficient displays or detectors, and solar energy conversion.

Organized arrays of GaSe disk-like nanoparticles could result in materials that are very strongly birefringent. The extent of birefringence depends on the difference in the refractive indices for light polarized parallel versus perpendicular to the liquid crystal director axis. We also speculate that if there is strong electronic coupling between adjacent quantum dots in one direction, the refractive index along that direction will approach that of the bulk material. As such, hybrid LCs may be far more birefringent than their organic counterparts.

4.2. Polarization and Time-Resolved Spectroscopy.

For this project, 8 nm GaSe particles are dissolved in the smectic-A phase of a very

common LC material 4-octyl, 4'-cyanobiphenyl, 8CB. At temperatures over 40.8 ºC, 8CB forms an isotropic phase, a true liquid. As the temperature is lowered, it forms a nematic liquid crystal phase, in which there is orientational, but no positional order. Between 22 and 33.8 ºC, 8CB forms a smectic-A liquid crystal phase, consisting of well-defined layers of oriented molecules. Finally, below 22 ºC, a crystalline phase is obtained[34]. In addition, GaSe particles were provided to Dr. Ghosh's lab at UC-Merced, where particles were suspended in a nematic phase LC and successfully aligned with the director axis of the LC[35]. In this study, the spatial orientation of the aggregates and thus their spectroscopic propertied were controlled by application of in-plane electric fields.

Samples are prepared by sandwiching the nanoparticle/LC mixture between two microscope slides. Through chemical modification of the glass surfaces, the director axis can be made to be parallel or perpendicular to the slides. If the surface is coated with poly-vinyl alcohol and unidirectionally rubbed, this establishes a director axis that is parallel to the surface of the slide. A perpendicular director axis is obtained by coating the surfaces with a sub-monolayer of a surfactant, such as an alkyl carboxylic acid. A clean slide is simply dipped in an aqueous solution of the carboxylic acid, rinsed and dried. The carboxylate group anchors to the surface and the alkyl chain extends perpendicular to the surface. This establishes the preferred direction for the liquid crystal. Polarization spectroscopy data obtained on parallel director samples by Shoute *et al*[30] show that in the smectic-A phase, the GaSe nanoparticles are extremely well oriented. Figure 19 shows the polarized absorption intensity of GaSe nanoparticles in smectic-A 8CB as a function of the angle, Θ, between the LC director axis and the polarization of the light. Also shown is a sine squared curve, fitted to the 416 nm polarized absorption curve. The curve corresponds to $A = 0.004 + 0.055 \sin^2 \Theta$. The 0º versus 90º absorbance ratio is about 15:1 at 416

nm. We note that the absorbance is largest when the polarization of the light is aligned with the unique axis of the LC. The lowest energy GaSe nanoparticle absorption is almost entirely polarized along the *z* axis, the normal to the particle. The results in Figure 19 therefore indicate that the *z* axes of the particles are very well aligned with the LC.

Time-resolved fluorescence spectroscopy (also done by L. C. T. Shoute, a previous postdoctoral fellow in the group) indicates that in the LC environment, GaSe nanoparticles form aggregates consisting of weakly- and strongly-interacting domains. Most of the particles are in the weakly-interacting domains and a small fraction of the particles are in strongly-interacting domains. The strongly-interacting domains have these disk-like particles stacked to form linear, one-dimensional regions in which the interparticle coupling is very large, about 1600 cm^{-1}. We speculate that most of the nanoparticles in the weakly-interacting domains are between the layers of 8CB molecules, forming two-dimensional sheets of particles. Time-resolved fluorescence spectra presented in Figure 20 suggest energy transfer from the weakly- to the strongly-interacting domains, in which the fluorescence maximum evolves from about 474 nm to 517 nm in less than 30 ps. This is followed by slower (~ 3 ns) energy transfer within the strongly-interacting domain, with the result being a further red shift of the fluorescence spectrum. This result indicates that excitons migrate a long distance along the director axis.

In the case of a perpendicular director, this distance is limited by the thickness of the sample, typically tens of microns. Thus, with a sample of known thickness, the differences between fluorescence spectroscopy of the samples with parallel and perpendicular directors can be indicative of the exciton migration distance scale. Therefore, by varying the thickness of the LC layer, these experiments provide a means of determining the distance scale over which exciton transport occurs. Preliminary results (collected by L. C. T. Shoute) shown in Figure 21

suggest these distances are very long. The results comparing 46μm parallel and perpendicular samples are displayed in Figure 21. The results are different for the two samples, indicating that the exciton migration distance is somewhat limited by the thickness (46μm) of the sample. Figure 21 therefore implies that excitons migrate on the order of tens of microns! This is an extraordinary result – it corresponds to the exciton migration through $10^4 - 10^5$ particles. The result suggests that these types of nanoparticle arrays may be capable of extremely efficient photon collection, followed by long distance directed energy transport.

As mentioned above, this project has extraordinary potentials. However, the results presented here can only be obtained if the GaSe particles are extremely high quality; relatively larger, very-well aggregated (high peak to valley ratio), and have the right edge-ligands. An example of this type of synthesis was shown in Figure 7 (sample 1) earlier. Unfortunately, a reproduction of these particles was never attained. Our speculation is that extremely high quality particles such as those in Figure 7 (sample 1) were only possible to synthesize with the earlier (before 2007) commercial bottles of TOP that contained the right concentration of free radicals. GaSe particles produced by the variety of syntheses after that never led to the production of particles that will readily align in LCs. At first, it was thought that the problem might be possible introduction of air or water in the 8CB, and thus the particles are oxidized. However, same results were obtained even after the liquid crystal was carefully heated and vented with nitrogen gas to get rid of any trace of air and water. In addition, a range of concentrations from 1 part in 300 to 1 in 50 was tried with no success. We speculate that the nano-disks will only align in the liquid crystal if they come in an already well aggregated form, as synthesized. The other less likely reason can be concentration. That deduction is made based on the fact that even particles such as those presented in Figure 8, which are relatively large, concentrated, and have tight-

binding ligands on their edge did not align in the LC samples. The peak to valley ratio of this sample (~2.2) is much smaller than that of sample 1 in Figure 7, which is around 3.4. In fact, a common obstacle with these PA anhydride-ligated particles is that they form bulk when dissolved in 8CB. The nanoparticle/LC solution quickly turns dark yellow, red, and eventually gray, which signals that bulk GaSe has formed. The GaSe hybrid liquid crystal project, with all of its extraordinary potentials, was discontinued because of this issue of synthesis irreproducibility.
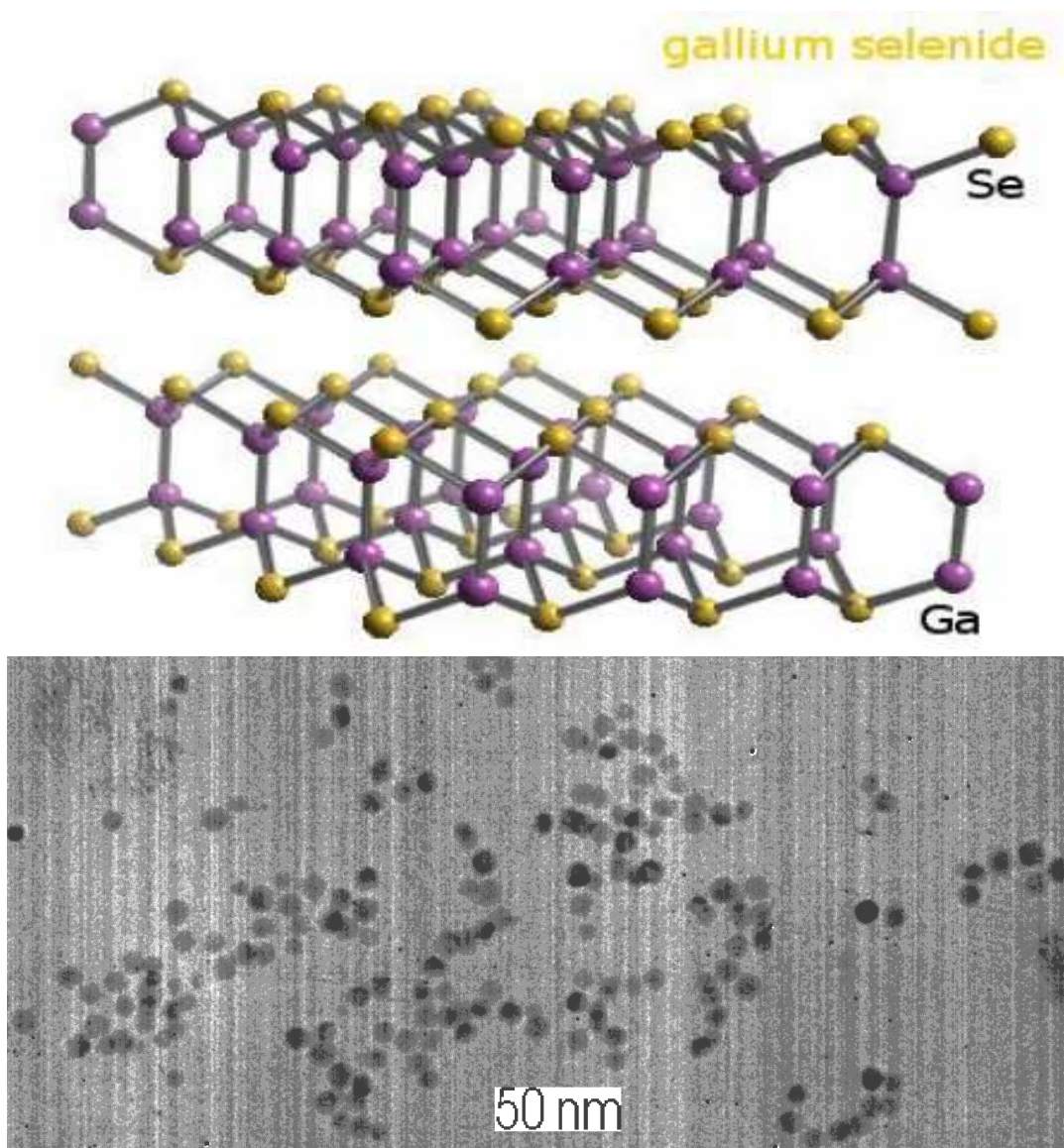
Figure 1: Crystal Structure of Bulk β-GaSe (Top) and TEM Image of GaSe Nanodisks (Bottom). Purple represents gallium atoms, and yellow represents selenium atoms.
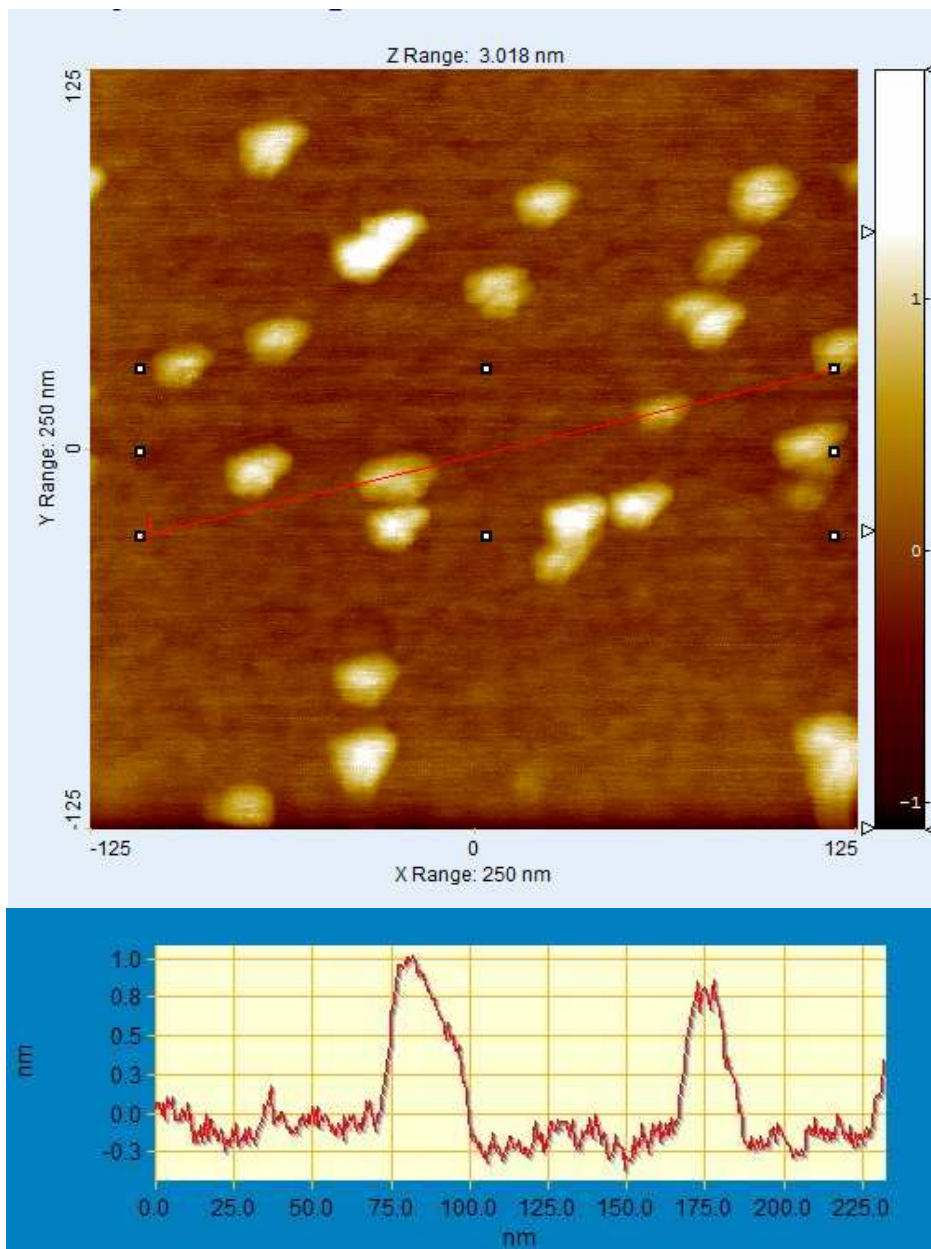
Figure 2: AFM Topography Image of GaSe Monomers.
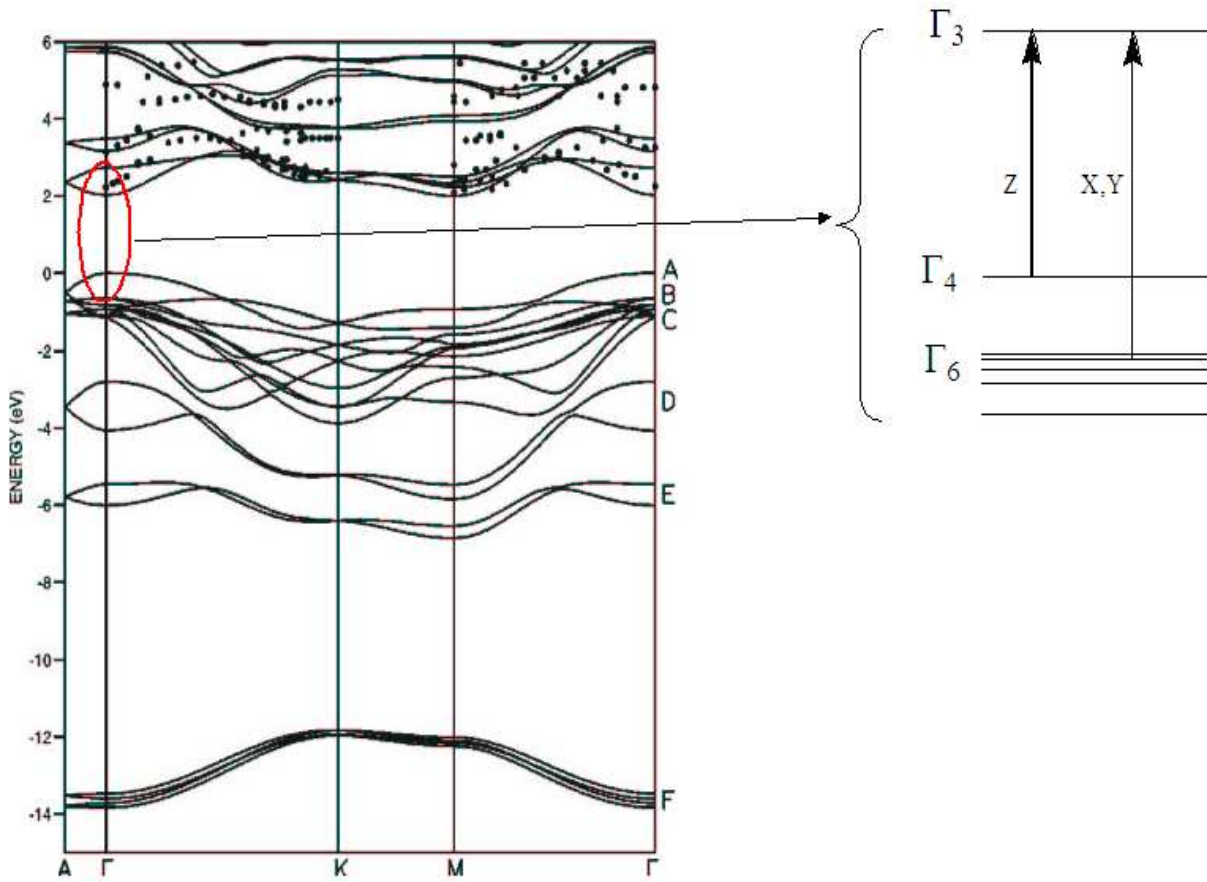
Figure 3: Band Structure of Bulk GaSe[36]. There are two main transitions at the Γ point, one is z-polarized and the other is x,y-polarized*.

*Phys. Rev. B. **2002**, *65*, 125206

Figure 4: GaSe Nanoparticle Solution Showing a Deep Yellow Color. [Photograph by Deborah Lair (c 2010)]
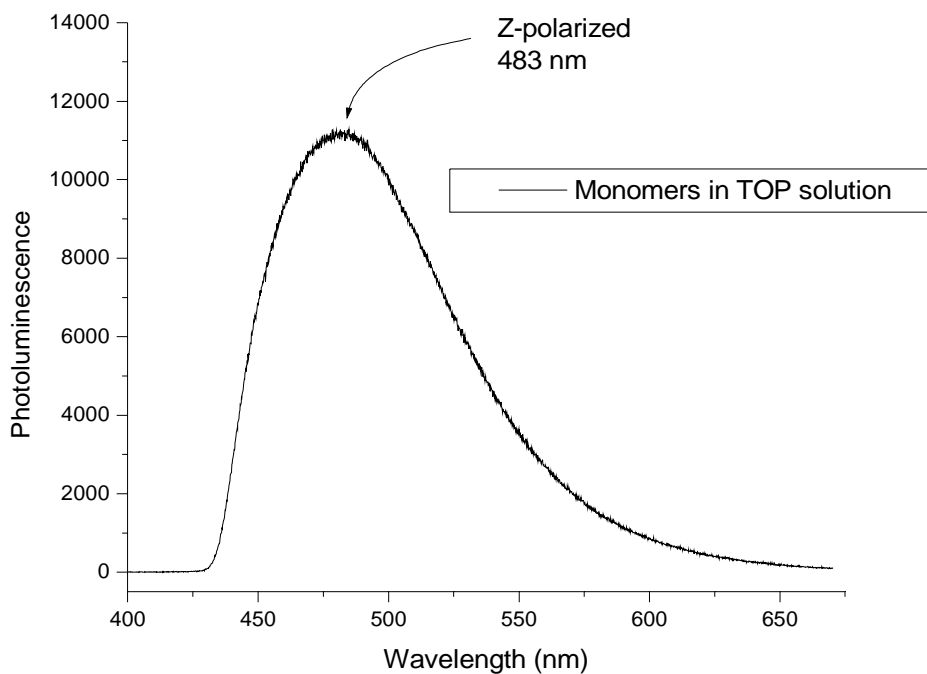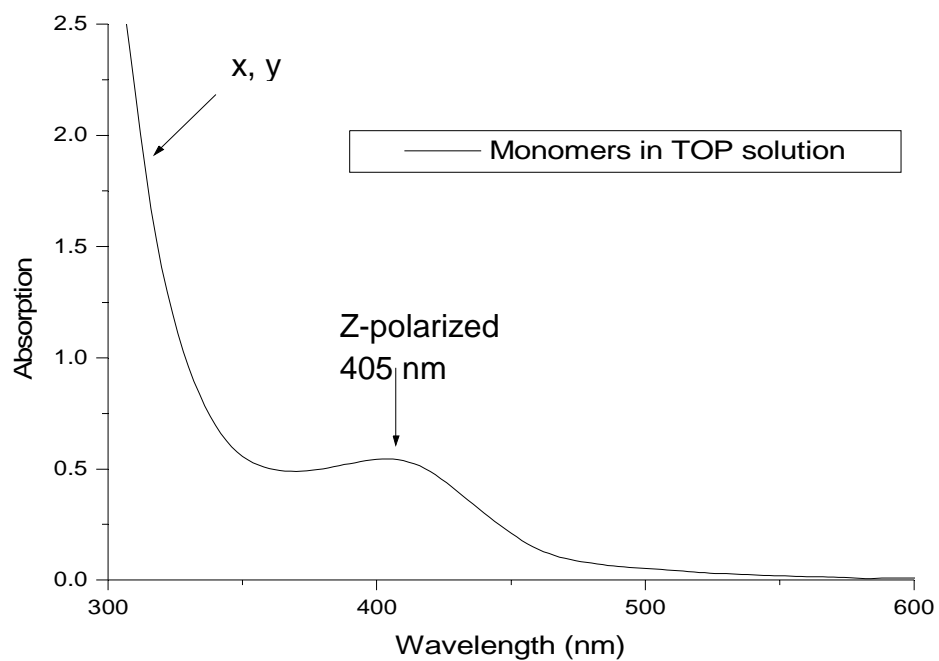
Figure 5: Typical Absorption and Photoluminescence Spectra of GaSe Monomers.
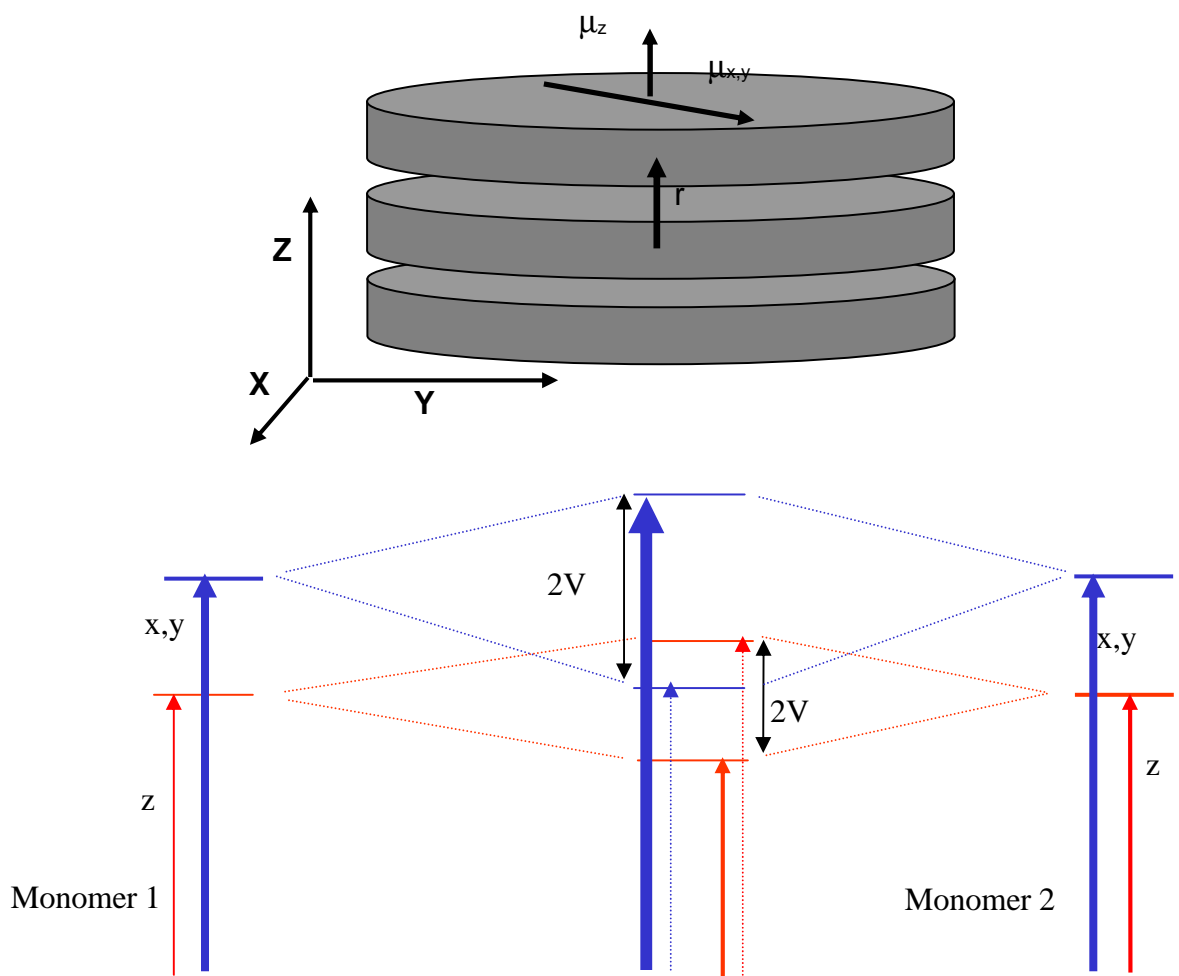
Figure 6: Transition Levels of a Coupled Dimer of GaSe Nanodisks.
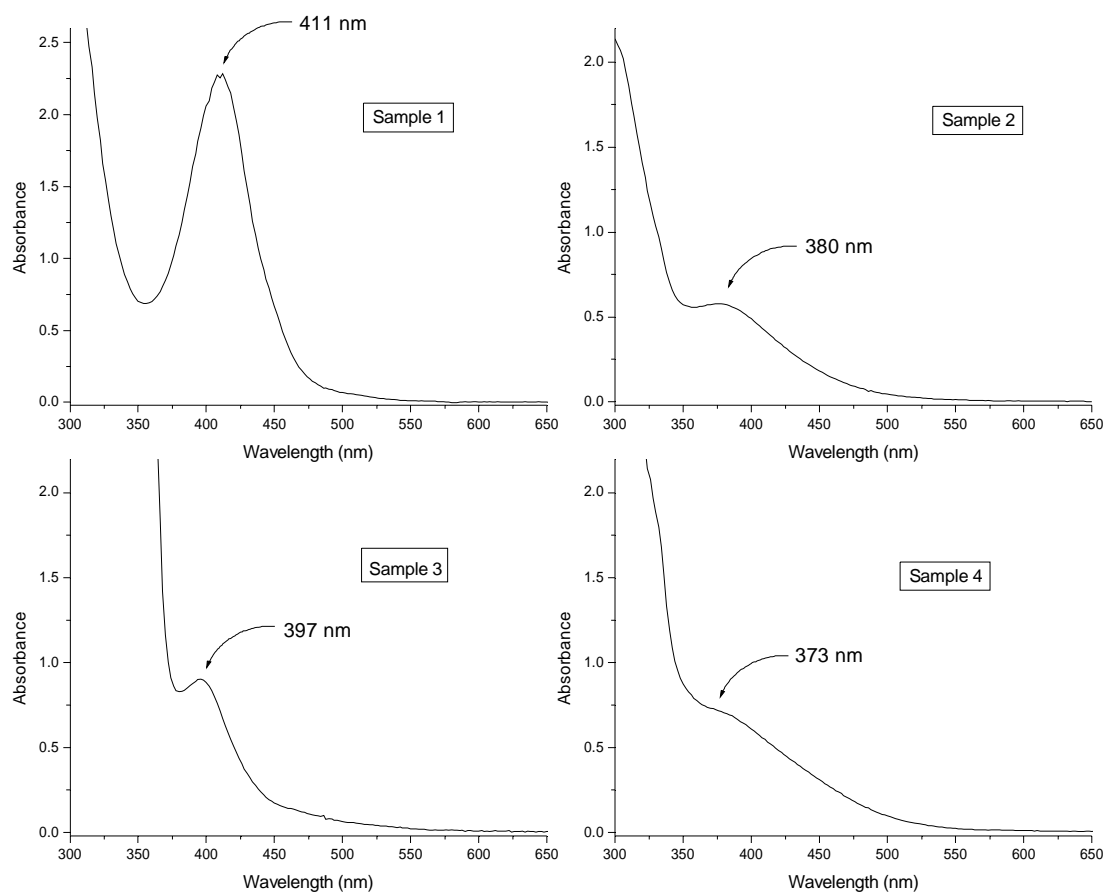
Figure 7: Absorption Spectra of Selected GaSe Syntheses Using "Greener" Reagents.
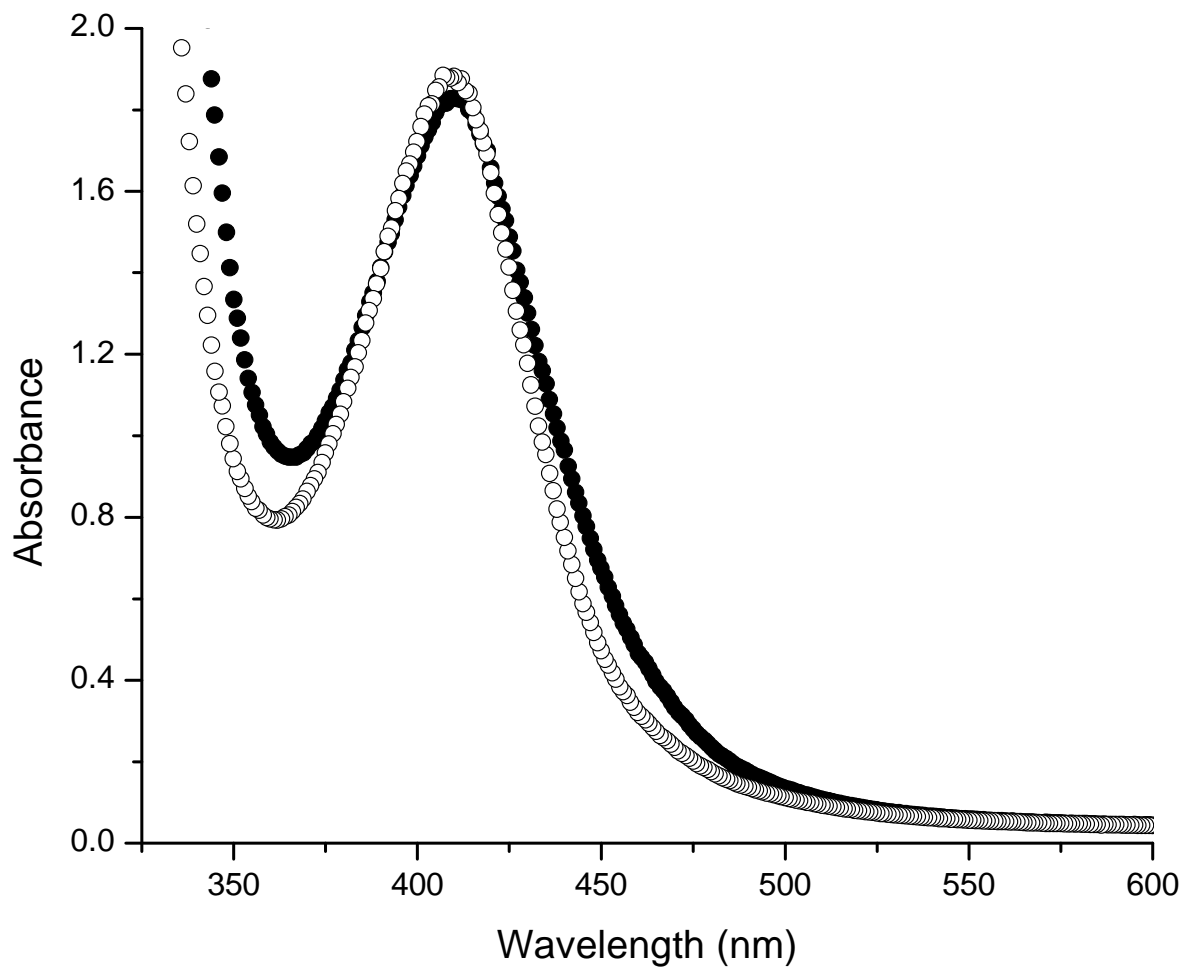
Figure 8: Absorption Spectrum of Synthesis A, GaSe Particles on the Day of Synthesis (Solid Circles) and Two Months after Synthesis (Open Circles). The particle size distribution has focused down over time.
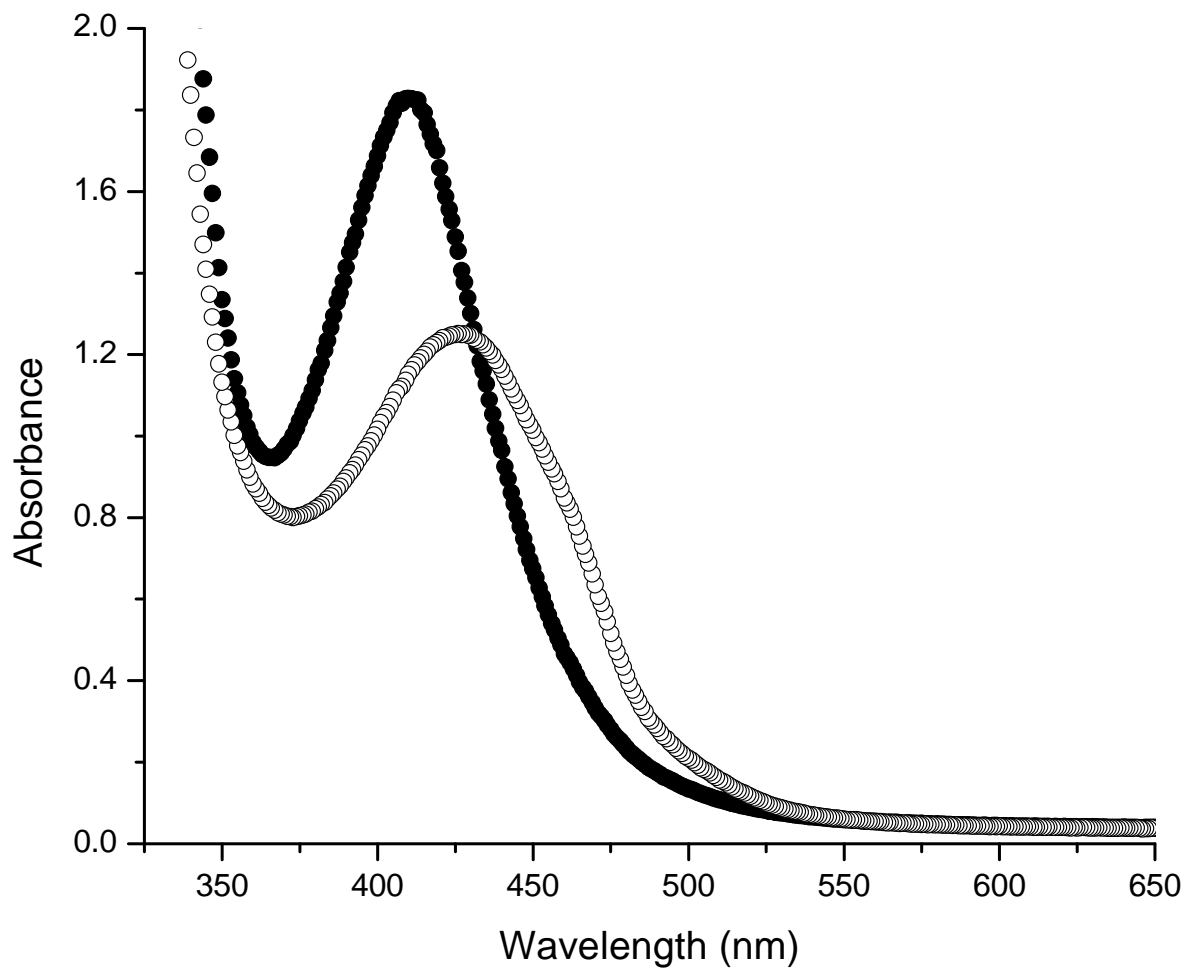
Figure 9: Absorption Spectrum of Synthesis A, GaSe Particles Before (Solid Circles) and After Addition of Dodecyl Aldehyde (Open Circles).
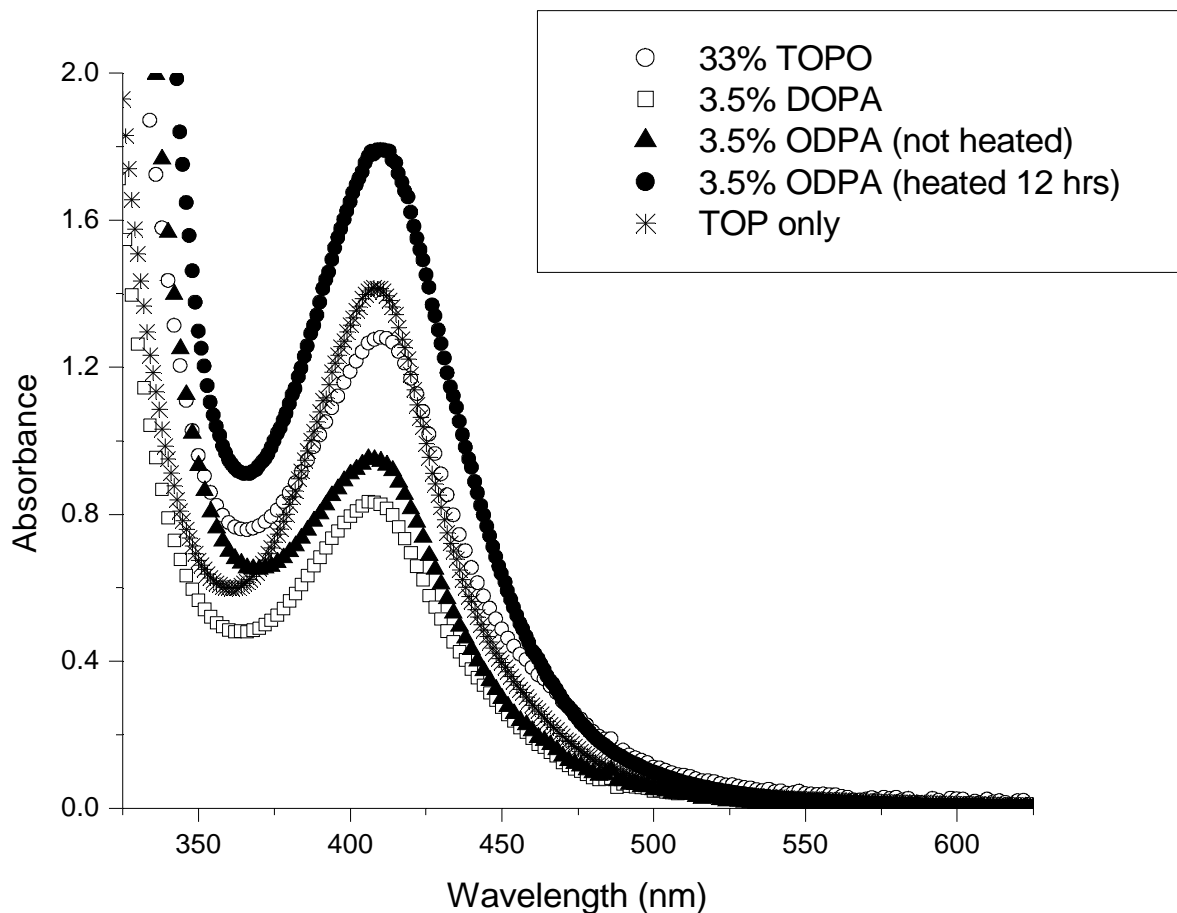
Figure 10: Absorption Spectrum of GaSe Particles with Different Ligations. The reaction precursor contains, in order, 33% TOPO (open circles), 3.5% DOPA (open squares), 3.5% ODPA with no heating (solid triangles), 3.5% ODPA with 12 hrs of heating (solid circles) and TOP only (stars), respectively.
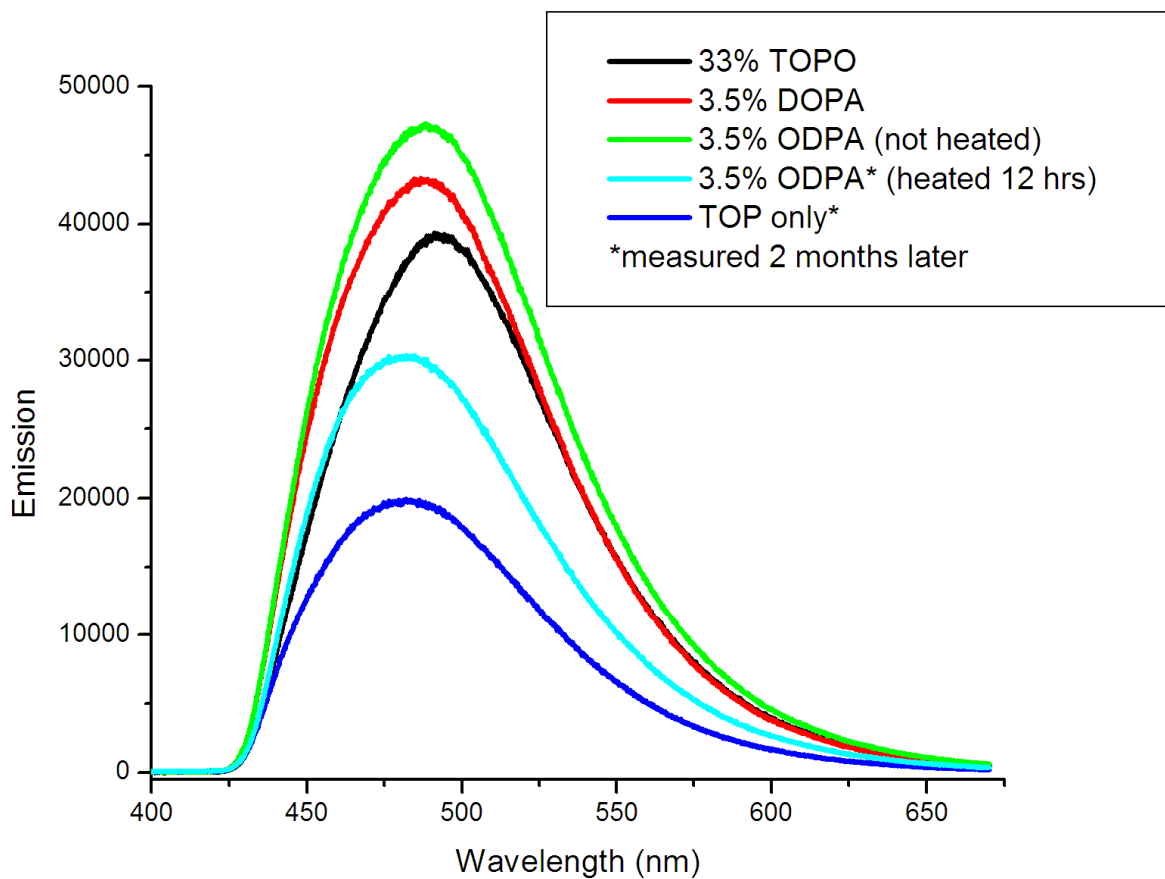
Figure 11: Emission Spectrum of GaSe Particles with Different Ligations. The reaction precursor contains in order 33% TOPO (black), 3.5% DOPA (red), 3.5% ODPA with no heating (green), 3.5% ODPA with 12 hrs of heating (cyan) and TOP only (blue), respectively.
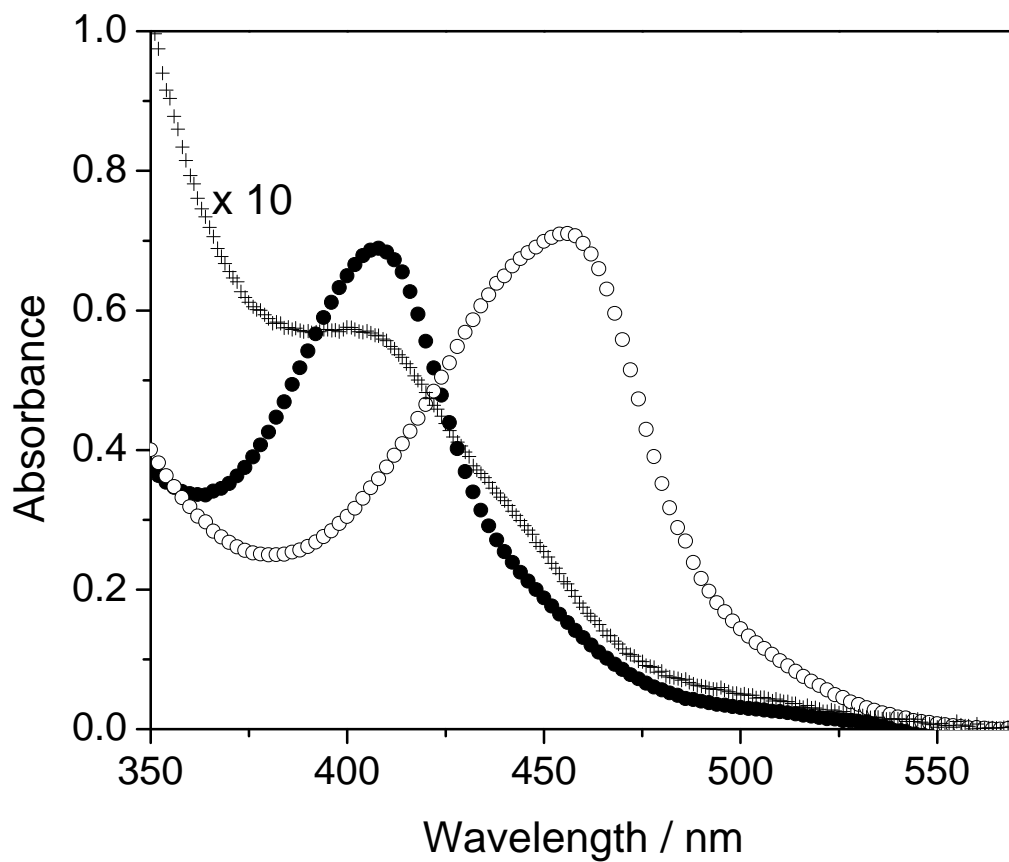
Figure 12: Absorption Spectra of the GaSe Nanoparticles, As-synthesized with TOPO (Solid Circles), Diluted in TBP/TOPO (Plus Signs), and with 3% Dodecanal (Open Circles). The monomer absorption curve has been multiplied by 10.
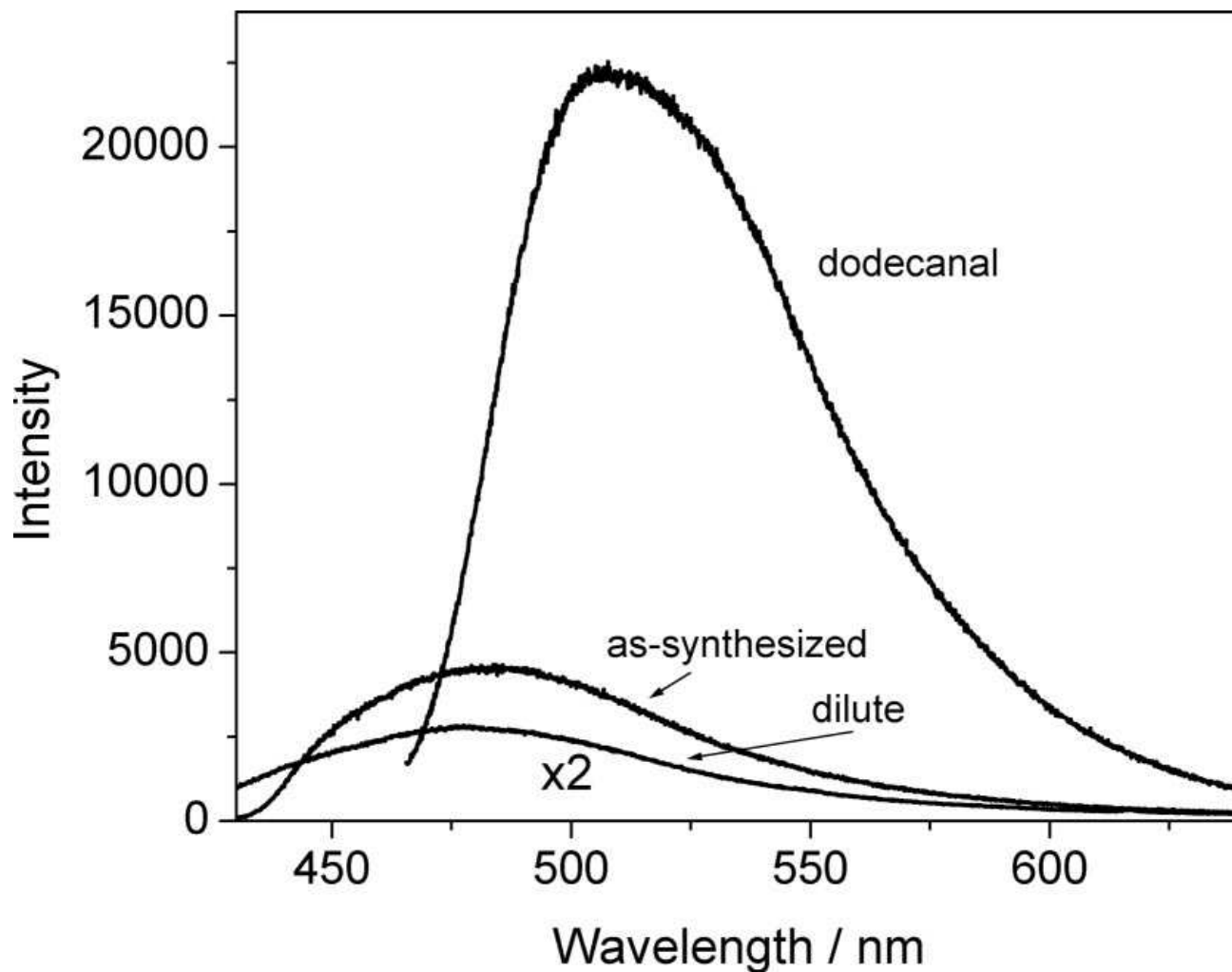
Figure 13: Fluorescence Spectra of the GaSe Samples Shown in Figure 12, As-synthesized with TOPO, Diluted in TBP/TOPO, and with 3% Dodecanal, as Indicated. The intensities are scaled to the same absorbances at the excitation wavelengths of 410 (monomer and as-synthesized) and 460 nm (dodecanal). The monomer fluorescence curve has been multiplied by 2.
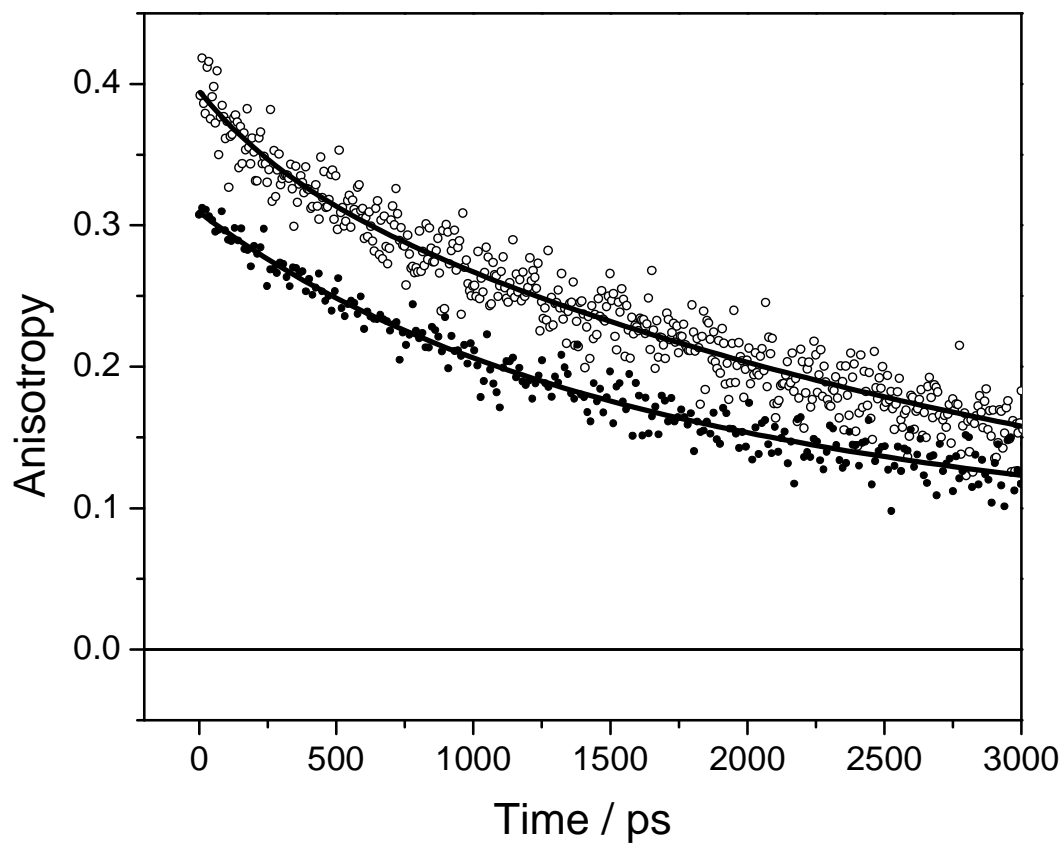
Figure 14: Time-resolved Fluorescence Anisotropies for GaSe Monomers Excited at 410 nm (Solid Circles) and Dodecanal-ligated Aggregates Excited at 460 nm (Open Circles). Also shown are curves fitted to the experimental results.
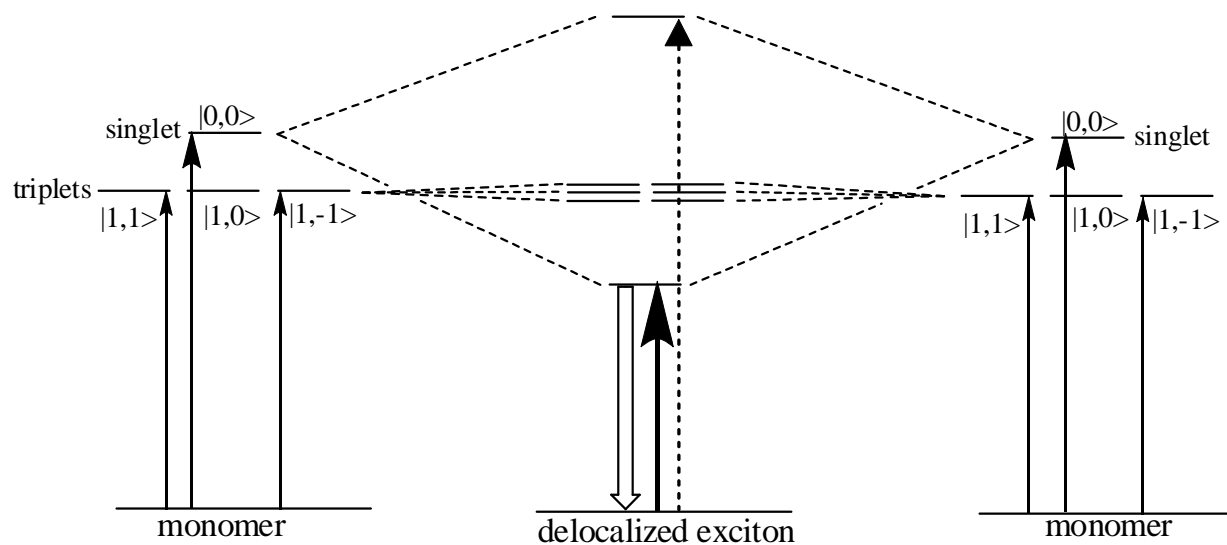
Figure 15: Schematic Energy Level Diagram for the Interaction of Singlets and Triplets in a Particle Dimer. The singlet coupling is much larger than that of the triplets, lowering the energy of the lowest singlet state. Dimer fluorescence occurs from the lowest singlet state.
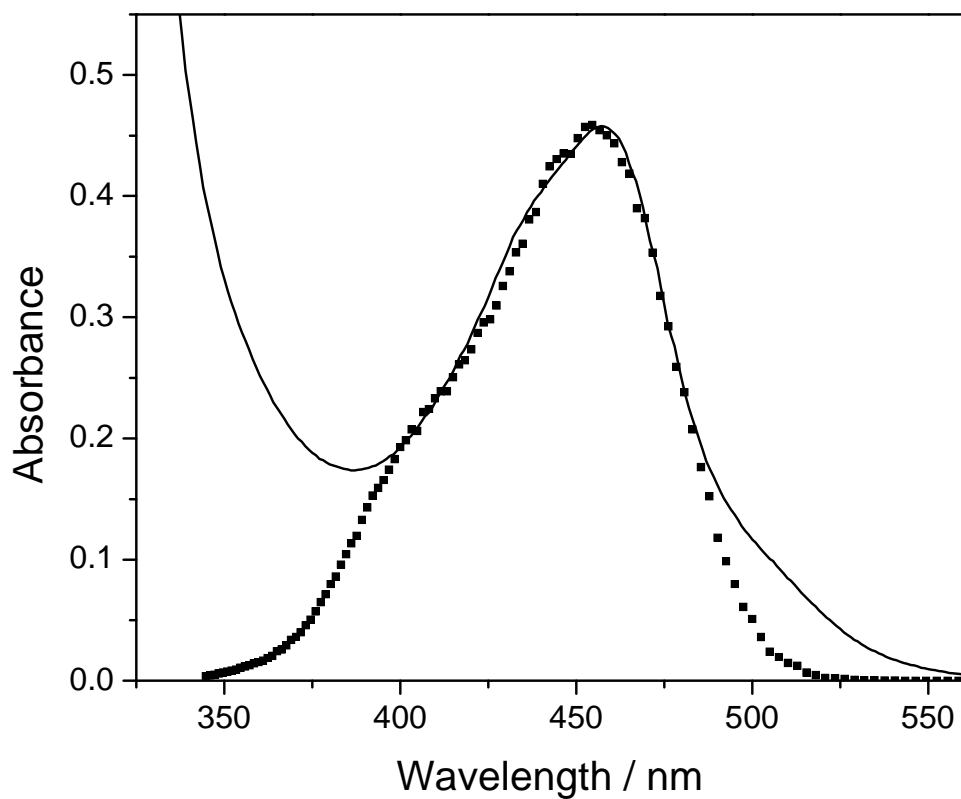
Figure 16: Experimental (Solid Curve) and Calculated (Dotted Curve) Aggregate Absorption Spectra. The calculated curve was obtained for an average interparticle coupling of 1950 cm^{-1} and having a standard deviation of 2300 cm^{-1}.
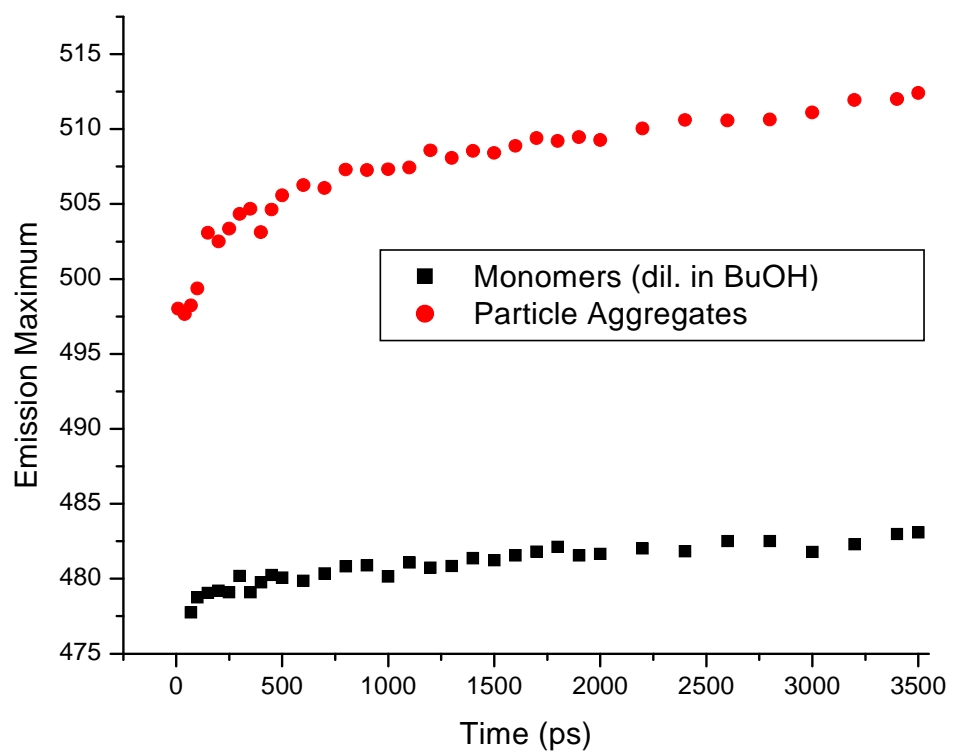
Figure 17: Time Resolved Emission Spectroscopy of GaSe Monomers Versus Aldehyde-ligated Aggregates.
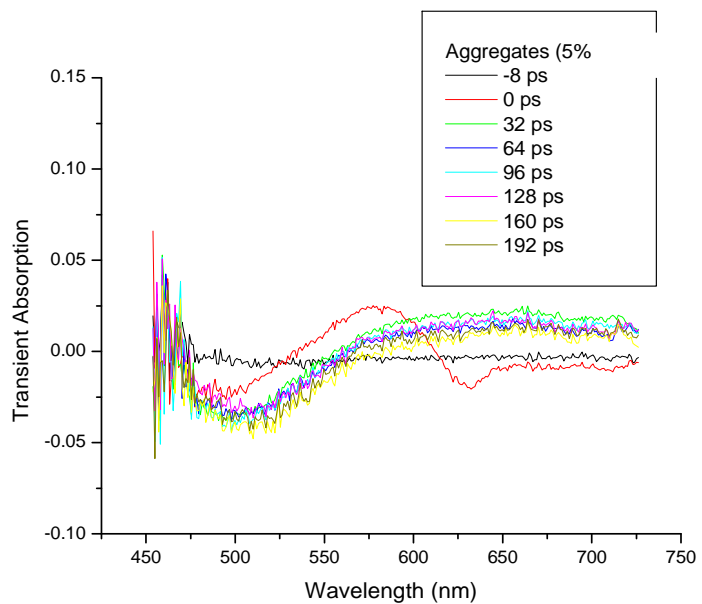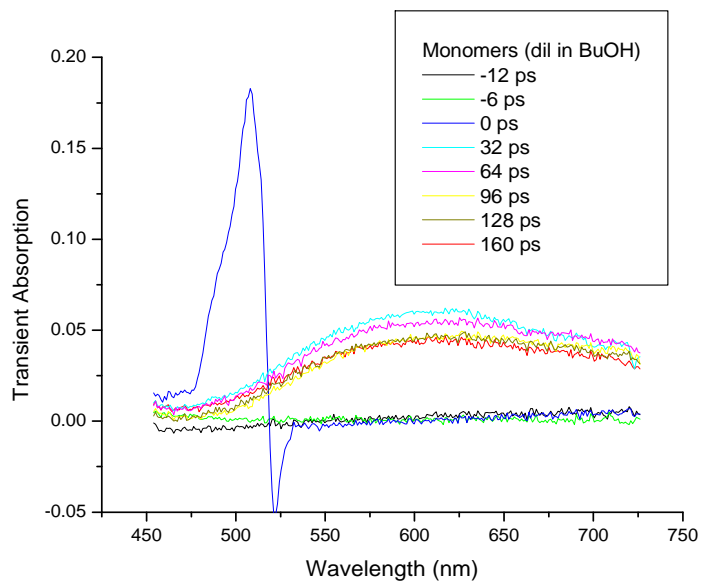
Figure 18: Femtosecond Transient Absorption Spectra of (Top) GaSe Monomers and (Bottom) GaSe OA-ligated Aggregates for the First 200ps After Excitation.
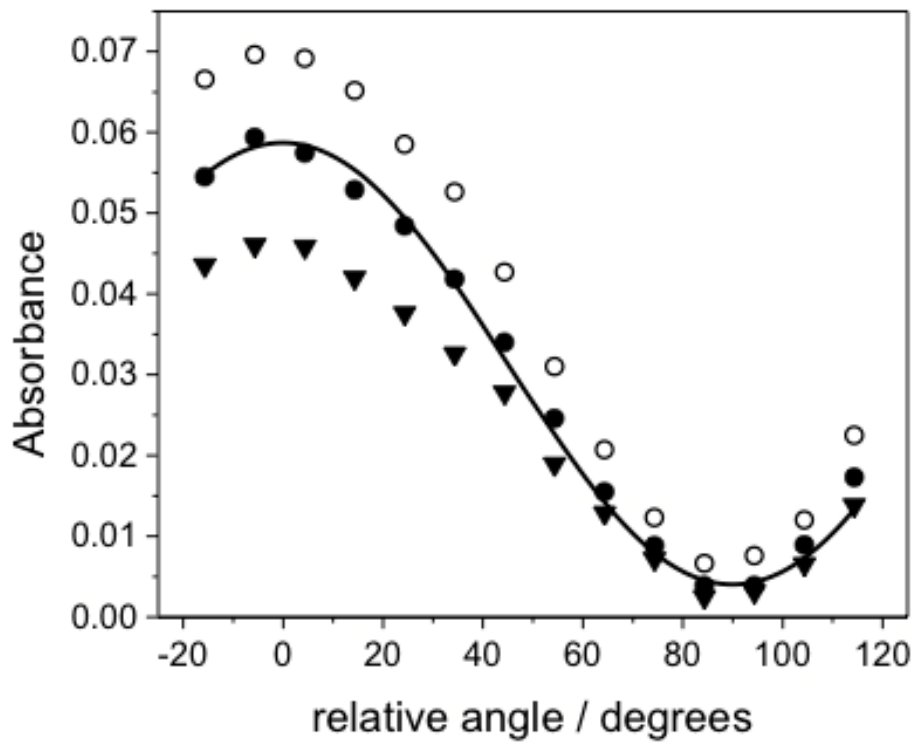
Figure 19: Absorbance at Several Wavelengths as a Function of the Angle Between the Polarization of the Light and the Liquid Crystal Director Axis. Absorbance points for 400 nm (open circles), 416 nm (solid circles), and 432 nm (solid triangles) are shown. Also shown is a sine squared fit to the 416 nm absorbances.
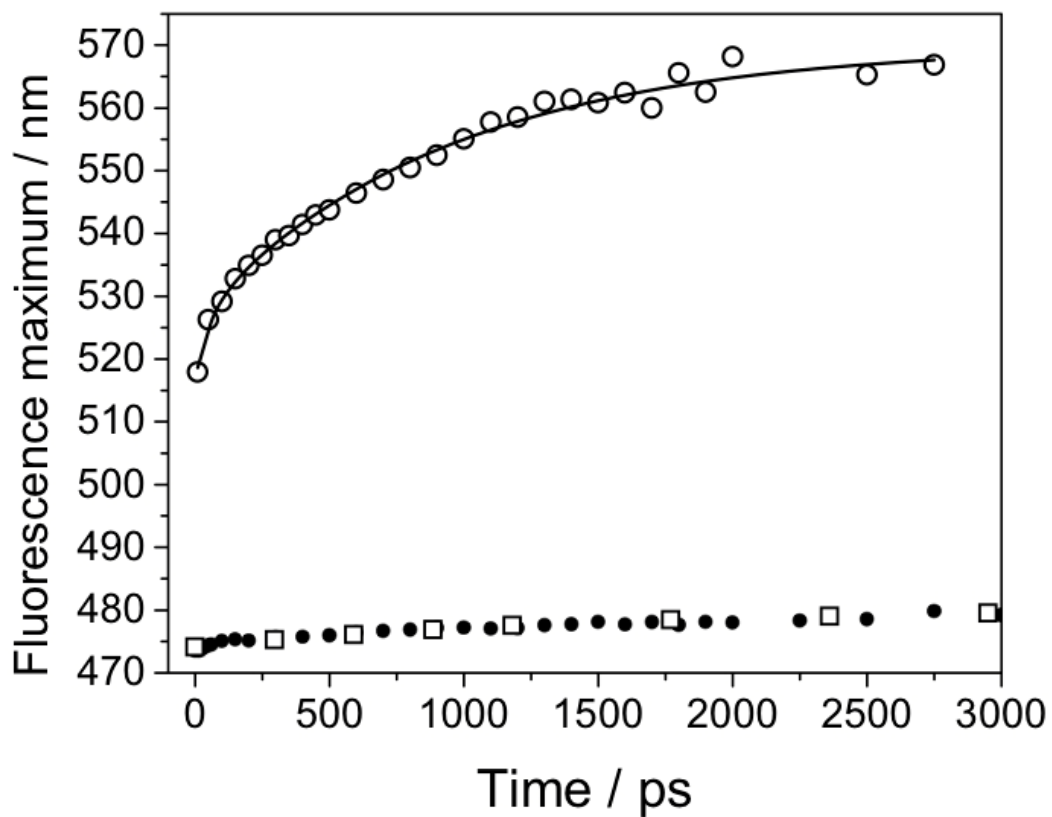
Figure 20: Time Dependence of the Fluorescence Maxima for GaSe Nanoparticles in Smectic-A 8CB (Open Circles). For comparison, results for GaSe nanoparticles in diluted 1:6 in liquid mixed solvent chemically analogous to 8CB (solid circles) and diluted 1:1.8 in octane (open squares) are also shown.
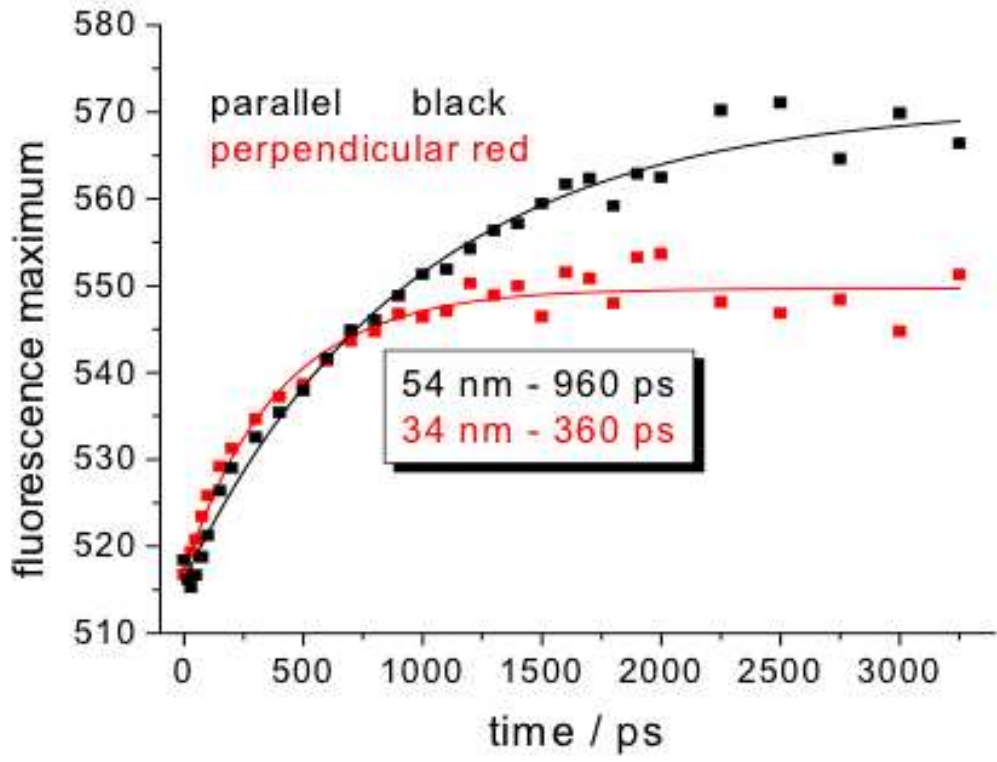
Figure 21: Time Resolved Fluorescence Maxima of 46-micron Thick GaSe/LC Samples That Are Identical Except for the Director Axes, Perpendicular (Red) and Parallel (Black).

PART II. CdTe/CdSe NANO-HETEROSTRUCTURES

Chapter One: Introduction

1.1. Importance of Nano-heterostructures (NHS).

Bulk semiconductor heterostructures have been around for a relatively long time, approximately since 1930s. In fact, we owe some of the most commonly used technology in our daily life to heterostructure-based electronic devices such as light-emitting diodes (LEDs), double-heterostructure lasers used in telecommunications, and high electron mobility transistors (HEMTs) used in satellite television. Heterostructures like AlGaAs have been used as solar cells for space program for years now[37]. Most of the research during this era focused on group III-V compound structures. In 1970s, Dingle *et al.* demonstrated quantum well effects by replacing the existent bulk GaAs section in a GaAs-AlGaAs with a GaAs thin film, showing a continuous shift in energies with progressively thinner films[38]. Following the scientific advancements in quantum well heterostructure devices, researchers started thinking of using structures with even lower dimensionality, and hence came the era of quantum wire and quantum dot heterostructures starting in 1980s[1]. Since then, extensive research has been done on synthesis, self-assembly, and optical and dynamical properties of these nano-heterostructures.

Modern nano-heterostructures (NHSs) are grouped into three categories, straddling gap (type I), staggering gap (type II), and a less common one, broken gap (type III) (Figure 22). Type I heterostructures such as CdSe/ZnSe or CdSe/ZnS are so that the band gap of one semiconductor, CdSe in this case, is sandwiched in the band gap of the other material. The larger band gap material usually passivates the surface of the smaller band gap semiconductor and

increases its quantum efficiency. In type II heterostructures such as CdTe/CdSe, CdSe/ZnTe, or ZnTe/ZnSe, both the conduction and valence bands of the structures lie lower in energy.

Type II NHSs are of particular interest because of the spatial separation of the electron and hole following photoexcitation. Upon excitation and creation of an electron-hole pair or an exciton in one of the sections of the NHS, either the electron non-radiatively relaxes down to the conduction band of the other section or the hole to the valence band of the other section. This leaves the electron in one section of the NHS and the hole in the other. This spatially charge separated state makes NHSs promising candidates for use in photovoltaics given 1) the band gaps are tuned to absorb most of the sunlight, 2) charge separated state is sufficiently small in energy that re-absorption of emitted light is minimized, and 3) the charge separated state has a long lifetime during which the electron and hole can be transported.

1.2. Properties of II-IV Semiconductor Heterostructures.

The electronic properties of II-IV semiconductor (Cd or Zn with S, Se or Te) nanoparticles are such that several different type-I and type-II junctions can be formed. Type-I junctions result in the electron and hole residing in the same material. Type-II junctions result in a lowest energy state in which the electron and hole are spatially separated. The relative energetics of the conduction and valence bands along with quantum confinement effects determine the extent to which charge separation occurs.

The II-IV semiconductors adopt either cubic (zincblende) or hexagonal (wurtzite) crystal structures. In the former case, the anions adopt a cubic-close-packed arrangement, and the cations go in every other tetrahedral hole, also forming a cubic-close-packed arrangement. The cubic lattice has no unique direction and the optical properties are isotropic. In the wurtzite case, the anions adopt a hexagonal-close-packed arrangement, and the cations go in every other

tetrahedral hole. The wurtzite lattice has a unique axis perpendicular to the hexagonal planes. The two lattices have the same nearest neighbor coordination and differ only at longer ranges. Similar physical properties are therefore obtained. ZnS, ZnSe, ZnTe and CdTe favor the zincblende structure; CdS and CdSe favor the wurtzite structure. The energy difference between the zincblende and wurtzite structures is small for all II-IV semiconductors and most of them will grow in either crystal structure. These considerations dictate which nanoparticle morphologies are most easily obtained and the synthetic methodologies used to obtain the more and the less favorable crystal structures.

The lattice parameters of the different materials (sizes of the unit cells and hence atomic spacings) greatly affect the properties of any junction. Coherent (defect free) growth of one material on another is possible only if the lattice mismatch is small. Large lattice mismatches result in excessive strain energy and coherent deposition is limited to a few layers. The lattice mismatch is the driving force that produces interfacial defects and/or island growth after deposition of several layers. Interfacial defects can act as carrier recombination centers and their presence can dramatically alter the photophysics of the junction.

Chapter Two: Control of Morphology in Synthesis of Various CdTe/CdSe and CdSe/CdTe

Chemicals. A list of chemicals used for all of the syntheses reported in this chapter is presented, as follows: Cadmium oxide (99.5%, Aldrich), oleic acid (technical grade, 90%, Alfa Aesar), tellurium (powder 200 mesh, 99.8%, Aldrich), selenium (powder, 99+%, Alfa Aesar), tributylphosphine (97%, Aldrich), toluene (>99.3%, Sigma-Aldrich), methanol (HPLC grade, 99.9%, Fisher Chemical), cyclohexane (HPLC grade, 99.9%, Fisher Chemical), and acetonitrile (99.9%, Fisher Chemical) were all used as received with no further purification.

n-Octadecylphosphonic acid (PCI Synthesis) and trioctylphosphine oxide (technical grade, 90%, Aldrich) were recrystallized two to three times from toluene and acetonitrile, respectively. 1-Octadecene (90%, Aldrich) was vacuum distilled at around 140 ^{o}C. Trioctylphosphine (technical grade, 90%, Aldrich) was prepared by vacuum distillation at around 180 ^{o}C. Small amounts distilling over at temperature lower than 180 ^{o}C were discarded. The purified TOP was sealed and kept in a glovebox to avoid any oxidation to trioctylphosphine oxide (TOPO). The distillation was performed using an apparatus in which all the joints have been ground together and sealed with Teflon O-rings, ensuring a leak-free vacuum.

Instrumentation. Particle syntheses reported in this chapter are characterized by absorption spectroscopy, static emission spectroscopy, and TEM imaging. Static fluorescence spectra were obtained using a Jobin-Yvon Fluorolog-3 spectrometer using the Horiba J-Y software. The instrument consists of a xenon lamp/double monochromator excitation source and a CCD detector. Quantum yields are determined by comparison of the nanoparticle spectra with

the spectrum of rhodamine B in methanol, with the appropriate spectral calibration factors. This comparison involves collection of the luminescence in a face-on geometry. The absorbances of the nanoparticles and rhodamine samples are small (typically about 0.3). The quantum yields are then determined by taking the ratio of areas under the luminescence spectra. These spectra are corrected for instrument response: monochromator throughput and detector efficiency.

Most TEM images were obtained on a FEI Technai 12 transmission electron microscope with an accelerating voltage of up to 120 kV and a magnification capability of up to 300,000 times. This instrument has a 2 Å TWIN line resolution. Other TEM images were obtained on a JEOL JEM-2010 transmission electron microscope equipped with a LaB_6 filament. This instrument is capable of 2.4 Å point-to-point image resolution and 1.4 Å lattice fringe resolution.

2.1. Various Possible Morphologies of NHSs of CdSe and CdTe.

CdSe/CdTe heterostructures are relatively easier to synthesize due to the low lattice mismatch between them. A zinc blende unit cell is defined by the a-axis lattice parameter and a wurtzite unit cell is defined by the a- and c-axis parameters. The lattice mismatch between CdTe and CdSe is about the same along both axes and is about 7.6%[39]. CdSe is the most versatile type of core particle and tremendous amount of research has been done on synthesis of a range of CdSe morphologies. Wurtzite nanoparticles can be grown as nearly spherical particles or as rods with an easily controllable size and aspect ratio[40,41,42,43]. Under highly non-equilibrium conditions, zincblende CdSe nanospheres can also be obtained[44]. CdTe can be grown with either spherical, tetrapod, or rod morphologies[45,46,47]. The spheres are zincblende. The zincblende crystal structure has four equivalent faces (the normals at tetrahedral angles) which match the face normal to the unique wurtzite axis. Thus, tetrapods are formed when a zincblende nucleus is formed, followed by growth of wurtzite arms. There are some publications in the literature that

report the successful synthesis of CdTe rods. However, it is extremely hard to nucleate CdTe in wurtzite form. The TEM images presented in these publications often depict polydisperse samples of tetrapods and rods. We have developed synthetic methods which improve on the control of the morphology of CdTe nanoparticles. These synthetic methods (discussed in section 2.3) produce CdTe nanospheres of narrow size dispersion and very high luminescence quantum yields (~80%). These methods can also produce CdTe tetrapods having arms with a controllable size.

Figure 24 shows cartoons of various possible heterostructures that can be synthesized from CdSe and CdTe semiconductors[48]. Core/shell heterostructures are the most common and the most researched type of heterostructures. Spherical shells are uniformly deposited over spherical cores. There are numerous reports on the synthesis of these particles. The spectroscopy, exciton dynamics and multi-exciton behavior has been somewhat studied as well[49,50]. It is also possible to synthesize particles with spherical cores that have tetrapod arms protruding from the four tetrahedral faces of the core[51], as in Figure 24 (c). For matters of simplicity, let's refer to this type of heterostructure as dot/tetrapods from now on. Chapter Three: Auger Dynamics and Electron Cooling Times in CdTe/CdSe Nano-heterostructures presents an in-depth discussion of multi-exciton dynamics in core/shell and dot/tetrapod CdTe/CdSe heterostructures. Dot/rod morphologies (Figure 24 (b)) exhibit interesting optical properties but are hard to synthesize. Rod/Rod heterostructures are of particular interest in that they can be considered one-dimensional structures for purposes of modeling the exciton behavior. Although minimal radial growth does occur in these heterostructures, most of the growth happens from either one or both end faces of the rod cores in axial directions. This type of structure is depicted in Figure 24 (d). Rod/rod structures can also be synthesized in multiple blocks[45]. Optical properties and dynamics

89

of these structures have been studied by various groups[46,52,53]. Another possible morphology is to start off with tetrapod cores and grow axial extensions on the arms of the tetrapod to grow "tetrapod/rod" structures[54], as in Figure 24 (g). Other less common morphologies such as nano-barbells and tetrapod/tetrapod can be synthesized as well.

There are several considerations when it comes to the various morphologies of heterostructures from CdTe and CdSe. As was mentioned earlier, type II nanoheterostructures serve as donor-acceptor systems with the electron localized in one section of the heterostructure and the hole in the other. The excitation band energy and the energy of the charge-separated state can be simply tuned by changing the size of each or both of the sections in the heterostructures. This tenability of the charge transfer state is the fundamental characteristic that makes type II NHSs ideal for use in photovoltaics. In the case of CdTe/CdSe or CdSe/CdTe heterostructures, CdTe serves as the electron donor (the hole is localized in the Te section) and CdSe serves as the electron acceptor. Upon excitation of the Te section and creation of the exciton, the electron is very quickly (less than 2 ps) transferred to the Se section. Figure 23 shows a schematic band diagram of the heterostructure. There are several important phenomena that can either boost or diminish the optical gain in a NHS photovoltaic, and they all depend on the extent of charge separation. Hot electron transfer and carrier multiplication are mechanisms that can be used to minimize the energy loss of a photovoltaic. Hot electron transfer is partly determined by electron cooling rate, which is a function of charge separation. Auger recombination, the opposite process of carrier multiplication and a major cause of energy loss in PVs, is also a strong function of charge separation. In light of this, if the heterostructures of CdSe and CdTe are to be used in photovoltaics, the morphology that results in the greatest amount of charge separation is ideal.

Accordingly, elongated morphologies are more suitable for use in PVs because they provide for a larger charge separation. A comparison between a CdTe/CdSe core/shell and a CdTe/CdSe dot/rod that both have the same size Te core and the same molar amount of Se shell should prove insightful. In both cases, the hole is tightly localized in the CdTe core and the electron is somewhat localized in the CdSe shell. For the same molar amount of CdSe, the electron wavefunction tunnels through the CdTe core to a much larger extent in core/shell particles in comparison to dot/rod particles. In other words, the overlap of the electron and hole wavefunctions is much larger in core/shell particles and thus, a lower amount of charge separation is obtained. A simple (and incomplete) way to visualize this is to compare the quantum confinement of the electron along the radial axis of the core/shell particle with electron confinement along the axial axis of the dot/rod structure. The same amount of Se corresponds to a smaller thickness of CdSe shell in core/shell, and a longer length of Se rod in dot/rod. In other words, since the electron is much more confined along the thickness (radial axis) of the Se shell in core/shell, its wavefunction spills into the CdTe core section to a larger extent and thus results in little separation of the electron and hole. In contrast, the electron is much less confined along the length of the Se rod shell and thus, in case of long rods, there is minimal overlap between the electron and hole wavefunctions, and almost complete charge separation is achieved. Keep in mind that this is an incomplete picture of the reality but helps the physical visualization of the charge separated states. It is incomplete in the sense that the comparison of electron confinements is made along one dimension only: radial-only confinement in core/shells, and axial-only confinement in dot/rods. In reality, the three-dimensional quantum confinement energy of a sphere is lower than that of a rod. Take a really large spherical shell, and a really long rod shell. The electron in the large spherical shell experiences minimal quantum

confinement, while the electron in the large rod shell (although not confined axially) will remain quantum confined in the two radial directions. And charge separation is always more facilitated in elongated morphologies. In decreasing order, rod/rods, dot/rods, dot/tetrapods, and core/shells, provide for the largest charge separation.

Another consideration in choosing the most ideal morphology for use in PVs is the effect of electron and hole effective masses on charge separation. Effective mass of an electron and a hole in CdSe is 0.11 and 0.44[55], respectively. Electron and hole effective masses in CdTe are very close to CdSe, about 0.1 and 0.4[56], respectively. Effective mass of a hole in CdTe is about four times higher than the effective mass of an electron in CdSe. Thus the hole is tightly localized in the Te section, whereas the electron moves a little more freely in the Se section. With this in mind, let's compare a CdTe/CdSe dot/rod structure with that of an identically sized CdSe/CdTe dot/rod structure. Let's assume that in both cases, the rods are long enough to allow for complete localization of the charged particle in the rod section. In case of the CdTe/CdSe, the hole has a larger effective mass and it is, to a large extent, confined within the Te core. Thus, a higher degree of charge separation is obtained. Whereas in the case of CdSe/CdTe, the electron, having a lower effective mass, is not as confined within the core, and thus the charges don't fully separate. Following this logic, in order to achieve better charge separation, it is favorable to have the CdTe as the core and CdSe as the shell. This is especially true for elongated morphologies.

2.2. Se/Te Rod/Rods: CdSe Rod Cores Covered with a Rod-like CdTe Shell.

Out of the morphologies discussed in the previous section, rod/rods are of particular interest because they provide for the most effective charge separation. Considering the fact that CdSe is the most versatile type of core synthesis, and the fact that the wurtzite structure in CdSe is energetically favored, it is very straightforward to grow CdSe rod cores. The aspect ratio of the

rods can be easily controlled by changing the Cd:Se ratio in the reaction[42,43]. In general, CdSe

rods are grown by cadmium/ODPA precursors. The hexagonal lattice of CdSe rod nuclei is such

that the radial surfaces are covered with Cd but the axial planes are covered with Se. Once the

wurtzite nuclei form, the long-chain phosphonic acid molecules tightly bind the radial surfaces of

the rod and growth is only allowed in the axial directions.

Slightly modified procedures for the growth of these Se/Te rod/rods are adapted from

methods by which Scholes et al. and Herman et al. synthesize their particles. This method

consists of preparing a CdO/ODPA precursor in TOPO with a 1:2 Cd:ODPA ratio. Appendix B:

Selected Synthesis Protocols describes the details of the synthetic procedure. The precursor is

heated to 320 $^\circ$C until completely clear. This precursor is generally aged for about 24 hours

before use in the reaction. The aging of the precursor allows for the complete formation of

Cd/ODPA precursor and thus reduces the reactivity of the reaction solution. A percentage of

octylphosphonic acid (20% or less), a shorter chain ligand is used in some of the reactions to

grow longer aspect ratio rods. Octylphosphonic acid is not as tight-binding as ODPA, but for

steric reasons, it can bind the radial surfaces more effectively to produce longer rods. However,

use of OPA has the downside of formation of surface defects that cause branching of the

particles. This effect can be neglected as all of data presented in this dissertation are from OPA-

free syntheses.

Figure 25 shows the absorption and emission spectra of a typical synthesis of Se/Te

rod/rod heterostructures. To monitor the progress of the size growth of the particles, aliquots are

taken out at equally spaced time intervals. For lack of a better name, we refer to these

consecutive aliquots as layers of the Te shell. It is important to notice that these Te "layers" do

not correspond to monolayers. In this particular synthesis, CdSe cores are about 4 nm in diameter

and 10-12 nm in length. The lowest absorption band is at 635 nm with a corresponding photoluminescence band at about 660 nm. Upon deposition and growth of CdTe over the CdSe rod cores, the charge transfer band appears in the absorption spectrum and it shifts to the red consistently. Looking at the emission spectrum, the emission of the CdSe cores is completely quenched with growth of the first Te layer. Instead, emission from the charge transfer band appears. With further growth of the Te rod, the CT band consistently moves to the red as the exciton becomes less confined, and it loses intensity.

All of these spectral features can be explained by a simple particle in a box model, as presented in Figure 26. When the Te cap is still small, the hole wavefunction is tightly quantum confined, and thus, a significant part of the wavefunction tunnels into the Se section, as depicted by the shaded area in the right column of Figure 26. At this point, the overlap between the electron wavefunction in the Se section and the hole wavefunction in the Te section (shaded areas) is quiet large. Thus, the oscillator strength f of the CT transition, which is proportional to $f \propto [|<\varphi_{1e}|\mu|\varphi_{1h}>|]^2$, is also relatively large. As the name suggests, the intensity of a transition is proportional to the oscillator strength. As the Te section grows longer, the hole energy levels get closer to each other as a result of decreased quantum confinement, which causes the continuous red shift of the absorption and emission spectra. In addition, the hole also becomes more localized in the Te section, which results in further separation of charges and reduced overlap. This reduced overlap, and thus reduced oscillator strength explains the diminishing intensity of the CT emission band. Recall that the rate of spontaneous emission in a transition is defined by Einstein A coefficient, which is directly proportional to the oscillator strength and frequency of the transition cubed. Therefore, the radiative lifetime of the CT transition, which is inversely proportional to Einstein A, increases as the Te section grows. It is

important to note that the quantum yield of the particles approaches almost zero by the end of the reaction as the CT band has no intensity.

Going back to the emission spectra in Figure 25, there is also a second emission peak that appears to the blue of the charge transfer band. That peak is assigned to the emission of the individually nucleated CdTe particles. As soon as TOP/Te is injected into the CdSe cores solution, some independent CdTe nuclei are formed. Of course, it is expected that most of the Te precursor is deposited onto the cores but individual homogeneous nucleation of CdTe particles cannot be avoided. This is in part due to the high reactivity of the TOP/Te precursor. In syntheses with CdTe cores, where TOP/Se is used to grow Se shells, CdSe nucleation is not observed at all. This is because TOP/Se is intrinsically a less reactive precursor than TOP/Te. As will be noted later, one way to inhibit the reactivity of the Te precursor is the addition of ODPA to the Te precursor. This was discovered later when working on growing CdTe spherical cores. The addition of ODPA to the Te precursor was never tried in Se/Te rod/rod syntheses. However, we strongly speculate that addition of ODPA should suppress the CdSe nucleation, if not completely, but to a great extent. The spectral interference from CdTe individual particles contaminates any dynamical data obtained from the samples. The only way to resolve this issue is to photo-select the heterostructures from the individual CdTe particles by exciting the sample right at the CT band edge, which is beyond the capabilities of our lab. Several attempts were made to physically separate the heterostructures from the CdTe particles by size selective precipitation. In this method, a minimal amount of methanol is added to the particles (that have been washed and redissolved in toluene) until the solution becomes slightly turbid. The addition of methanol changes the polarity of the solution only sufficiently so that the larger particles, that are the heterostructures, precipitate out of the solution while smaller particles, that are the CdTe,

remain in solution. After repeating this method a few times and measuring the emission again, the ratio of the CdTe emission band intensity to CT emission band intensity drops from almost 1:1 to 1:10. So, this method is very effective but does not remove the CdTe completely (Figure 27). Considering the fact that the quantum yield of the individual CdTe particles is unknown, one cannot safely neglect their presence in the solution. Size selective precipitation has another downside too; in each cycle, a percentage of the heterostructures are lost too.

Another problem that was commonly encountered in syntheses of Se/Te rod/rods was the issue of optical clarity. In all Se/Te and Te/Se heterojunction syntheses, it is a standard purification method that the freshly synthesized particles are washed with methanol, and then redissolved in toluene. However, for a reason that remains unknown to us, some of these Se/Te heterostructures would not dissolve in toluene very well. The problem of sample turbidity, and more importantly, the issue of CdTe nucleation instigated the idea of synthesizing heterostructures that have CdTe as their core, and are covered with various shapes of Se shells. As mentioned earlier, TOP/Se is a less reactive precursor that often does not result in homogenous nucleation of CdSe.

2.3. Synthesis of Various Morphologies of CdTe Nanoparticle Cores.

Before launching into the synthesis of Te-Se heterostructures, it is important to first discuss how to control the morphology and size of Te cores. There are several available techniques to control the morphology and size of a semiconductor nanoparticle. The most significant effects come from the reactivity of the cadmium precursor or the ligands used to make the cadmium complex. In case of CdSe, loosely binding ligands such as oleic acid result in a more reactive Cd precursor, and are known to grow spherical zinc blende morphologies. On the

other hand, use of tight radial binding ligands such as ODPA or tetradecylphosphinic acid (TDPA) are known to produce the thermodynamically favored rods.

Temperature and monomer concentration are among the important factors that can control the size and morphology. Upon injection of reactants, a certain initial concentration of monomers is formed, which will further react with each other to form nuclei. The nuclei react with the remainder of monomers to grow into particles. In order to obtain a specific morphology or crystal structure, the chemical potential of monomers has to be higher in energy than the energy of the nuclei's crystal structure. Chemical potential is a function of two variables, temperature and concentration: $\mu = \mu_0 + RT \ln(\text{conc})$. Thus, at any given time during the reaction, the monomer concentration determines the chemical potential of monomers. Monomer concentration immediately after chalcogen precursor injection determines the nucleation type. Monomer concentration is governed by their reactivity and the reactivity of the reactant precursors. The temperature of the reaction determines the equilibrium concentration of monomers. Changing the temperature has both thermodynamic and kinetic effects. It affects the relative chemical potential of the monomers and the already formed nuclei and particles. Consider the example of CdSe, in which the wurtzite crystal structure is lower in energy than the zinc blende. Thermodynamics favors the nucleation and growth of a wurtzite structure. In order to grow zinc blende CdSe, the monomer chemical potential should be increased to above the energy of a zinc blende CdSe. This can be attained by boosting the monomer concentration to a higher supersaturated level. A higher supersaturated monomer concentration can be obtained by increasing the reactivity of the Cd or Se precursors, which causes a flash formation of many monomers. Alternatively, decreasing the reaction temperature will lower the relative equilibrium concentration of monomers, so that a lower concentration of monomers at any given time is

sufficient to raise the chemical potential of monomers above the zinc blende's energy. Therefore, a combination of increasing precursor reactivity and decreasing reaction temperature assures growth of zinc blende CdSe. Leaving the temperature variable aside, the reactivity of the chalcogen precursor can be varied to obtain the right monomer concentration required for nucleation of a specific crystal structure. For example, in case of CdTe, addition of ODPA can efficiently inhibit the reactivity of the Te precursor to promote spherical growth.

With regards to variations in size, generally speaking, increasing the precursor injection temperature leads to the formation of more nuclei centers that run out of reactants faster, and therefore don't grow as large. Decreasing the temperature initiates formation of a smaller number of nuclei that have the chance to grow much larger before the reactants run out.

2.3.1. Rods and Tetrapods.

In contrast to CdSe where the wurtzite crystal structure lies lower in energy than the zinc blende structure, the energetically favored crystal structure of CdTe is zinc blende. Thus, CdTe naturally nucleates in zinc blende form, unless chemically forced otherwise. However, the difference between the wurtzite and zinc blende energies in CdTe is very small. The zinc blende nuclei are tetrahedrons where each face of the tetrahedron is equivalent to the (1 0 0) plane of a wurtzite structure. So, CdTe tends to nucleate in zinc blende and then grow wurtzite arms off of the equivalent (1 0 0) faces to form tetrapods (Figure 28a). It is certainly beneficial to be able to grow CdTe rod cores for synthesis of Te/Se rod/rods as they provide for greater charge separation. However, wurtzite nucleation of CdTe does not happen under reaction conditions that are usually used for growth of CdSe rods – that is use of ODPA or TDPA as ligands in the Cd precursor. At the very best, a polydisperse sample of tetrapods and rods is obtained. Literature

publications that report the successful synthesis of CdTe rods often show TEM images that depict a high percentage of tetrapods and defected tetrapods that are missing one or two arms, and thus look like rods. Figure 28b and c show a couple of examples[45,46].

Considering the fact that zinc blende is the thermodynamically favored crystal structure of CdTe, in order to get wurtzite nucleation, the chemical potential of monomers should be raised above the energy of wurtzite CdTe. In addition, the kinetics of the reaction would have to favor wurtzite as well. Chemical potential of CdTe monomers can be increased by boosting the reactivity of the reactant precursors. So, a reactive Cd precursor such as Cd/OA and a reactive Te precursor such TBP-Te should result in wurtzite nucleation of CdTe. However, this does not happen. The CdTe still nucleates in zinc blende form but does grow wurtzite arms to form tetrapods. At this point, a reliable method to grow high quality monodisperse CdTe rods remains unknown to us. Nonetheless, monodisperse reproducible synthesis of CdTe tetrapods can be achieved by use of a Cd/ODPA precursor. Figure 29 shows the corresponding absorption and emission spectra of such tetrapods. This is demonstrated by TEM imaging and the fact that no polarized luminescence from particles is measured.

Static anisotropy measurements add some insight in terms of assigning particle morphologies. In static anisotropy experiments, a population of particles is first photo-selected by polarized excitation light. The rotation time of particles is slow in comparison to the emission lifetime, meaning that the particles do not change their orientation before luminescing. The photoluminescence collected from the excited particles is detected, once after passing through a polarizer parallel to the polarization of the excitation source, and another time through a polarizer perpendicular to the excitation light. In this method, polarization of the emitting oscillators is measured. Static anisotropy measurements on these tetrapods, where they are

excited at the edge of the lowest transition, give anisotropy values of zero meaning the particles are isotropic. Given that growth of spheres is highly unlikely under heavy presence of ODPA, the only other feasible isotropic morphology is tetrapods. The lowest energy transition in wurtzite CdTe and CdSe rods is polarized along the c-axis or the long axis of rods. Thus, the fact that the observed luminescence from the particles is not polarized eliminates the possibility of rod-like morphology.

In contrast to the synthetic methods followed for synthesis of zinc blende CdSe spheres, where it is expected that use of a loosely-binding ligand such as oleic acid (OA) should prompt the growth of spherical particles, a Cd/OA precursor yields CdTe tetrapods. Appendix B: Selected Synthesis Protocols lists the complete details of representative syntheses from both methods of tetrapod growth: from a Cd/ODPA precursor, and a Cd/OA one. Surprisingly, a Cd-OA precursor results in the growth of tetrapods too. Formation and growth of tetrapods happens almost instantaneously after injection of the Te precursor. The only difference seems to be the aspect ratio of the tetrapod arms. A crude comparison between the two Cd precursors suggests that a Cd-ODPA complex results in tetrapods with longer aspect ratio rods. In absence of radially-binding ligands, tetrapod arms grow in both the radial and axial directions. Figure 29 shows the TEM image, absorption, and emission spectra of tetrapods produced by use of a Cd/OA precursor. Based on the TEM image, the size of the tetrapods are estimated to be about 12 – 15 nm with low aspect ratio arms. We note that there is very little spectral difference between the absorption and emission bands of the two types of tetrapod syntheses.

2.3.2. Spherical Quantum Dots.

CdTe nanospheres are prepared by slightly changing the synthetic procedures reported in literature[57]. The Te precursor is prepared by dissolving 12.8 mg (0.1 mmol) of Te and 50.1 mg (0.15 mmol) of ODPA in 0.143 mL (0.313 mmol) of TOP and 1 mL of ODE. This mixture is heated and stirred for 10 minutes at 80 ^{o}C to obtain a clear lime colored solution. The presence of ODPA in the Te precursor is the key to producing monodisperse spherical particles. In the absence of ODPA, TOP/Te, a very reactive precursor, reacts almost instantaneously with the Cd precursor to form tetrapods. The Cd precursor is made by dissolving 25.6 mg (0.2 mmol) of CdO in 0.252 mL (0.8 mmol) of oleic acid and 3 mL of octadecene (ODE) as the solvent. This mixture is heated to 220 to 230 ^{o}C until completely clear. The heating is continued to 280 ^{o}C at which point the Te precursor is injected. Upon injection, the temperature is dropped to 260 ^{o}C and maintained there for the duration of the reaction. The reaction is run for 10 minutes before shut down. Immediately after cooling down, the sample is diluted in 5 mL of anhydrous toluene and kept under nitrogen for later use. Optical properties of the sample such as absorption spectra, emission spectra, and time-resolved emission decays are measured using the sample as is, with no further processing. However, for transient absorption measurements that will be presented in Chapter Three, the sample is precipitated in a 2:3 methanol:toluene solution only once to get rid of excess Cd and other reactants in the sample. The precipitate is then redissolved in anhydrous cyclohexane and bubbled with nitrogen gas to eliminate any oxygen that is introduced as a result of processing. Excessive use of methanol (more than 40%) in the precipitation procedure strips off any ligands leaving the surface of the particles exposed and can cause irreversible agglomeration or surface oxidation.

TEM images confirm the morphology of CdTe cores to be spheres of about 3.55 +/- 0.5 nm (Figure 35). As mentioned earlier, use of ODPA in the Te precursor is the key to synthesizing monodisperse core particles with spherical morphology. With no ODPA in the Te precursor, TOP/Te, a very reactive precursor, reacts almost instantaneously with Cd to form tetrapods. Addition of ODPA sufficiently inhibits the reactivity of the TOP/Te precursor (and thus, lowers the chemical potential of monomers closer to the energy of zinc blende structure), which allows for a slower nucleation rate and continuous spherical (zinc-blende) growth. This synthesis protocol for cores is very reproducible leading to particles with very sharp spectral features (Figure 30) and unprecedented quantum yields of up to 90%. The FWHM of the cores' emission peak is about 30 nm. Figure 30 also shows a sample of the cores held against a hand-held UV lamp. The green photoluminescence emitted from particles can be easily detected by naked eye. The samples almost look like rhodamine!

Systematic variation in several parameters of CdTe core synthesis was researched in detail. The major tunable parameters in the synthesis are Te:ODPA ratio, use of TOP versus TBP, and precursor concentration. It was found that the relative amount of ODPA in the Te precursor plays a pivotal role in the quality of synthesis. A Te: ODPA ratio of 1:1.5 is the optimum ratio for synthesizing monodisperse spherical core particles. Figure 31 presents the absorption and emission spectra of three syntheses where the ratio of the Te:ODPA is varied systematically. A low amount of ODPA (Te:ODPA of 1:0.5, corresponding to black curves) inhibits the reactivity only enough to produce some spherical particles but does not efficiently suppress growth of tetrapod particles. The result is a polydisperse sample of both spheres and tetrapods. The dual emission in the fluorescence spectra confirms the existence of two species of particles. A 1:1 ratio (represented by red curves) yields only spheres, but the spectral features are

not as sharp, indicating a larger particle size distribution. In order to focus the size distribution as tightly as possible, a Te:ODPA ratio of 1:1.5 (green curves) is ideal. Figure 31 is self-explanatory in this regard. It is also noted that this ratio results in particles with the highest quantum yield.

The shorter chain phosphine, TBP, is known to be more reactive than TOP. This fact is used to tune the reactivity of the Te precursor to obtain the desired particle morphology[57]. In the previous section, we have already discussed how a TBP-Te precursor with no ODPA results in tetrapods (Figure 29). A TOP-Te precursor with no ODPA is still reactive enough that it yields tetrapods, but the reaction is much slower. Referring to Figure 32, sample aliquots from a TBP-Te and a TOP-Te synthesis (light blue, and blue curves, respectively) are taken at the same time. However, the tetrapods from the TOP-Te synthesis have not fully grown yet. As a result of lower reactivity, nucleation does not happen instantaneously, and thus two or more types of nuclei can be developed at differing rates. This can cause the growth of two or more particle species that are different either in size or morphology. Polydispersity in samples can be detected by broad or dual emission peaks. Based on this logic, the emission spectrum from the TOP-Te synthesis suggests that the sample is quite polydisperse. A TBP-Te precursor with ODPA, and a 1:1 mix of TOP and TBP Te precursor with ODPA are much less reactive, but clearly result in the production of two particle species, tetrapods and spheres. The Te precursors can be listed in order of decreasing reactivity as follows: TBP-Te, TOP-Te, TBP-Te with ODPA, 1:1 TBP-TOP-Te with ODPA, and TOP-Te with ODPA. As evident from Figure 32, the only way to obtain monodisperse CdTe spherical nanoparticles is to use a TOP-Te precursor with ODPA.

Particle size is slightly dependent on the concentration of the precursors. In general, diluting the reaction by use of a higher amount of ODE slows the reaction and results in slightly

bigger particles. In fast syntheses, there is a flash of nucleation immediately upon precursor injection. The large number of nuclei can only grow so much before running out of reactants. When the reaction is slowed down, in this case by lowering the concentration, a smaller number of nuclei are formed, and thus can grow bigger. The effect of concentration on reaction kinetics is significant. Figure 33 compares the progression of two CdTe reactions; the reaction volume is doubled in one of the syntheses. In the concentrated synthesis, the particles are finished growing 2 minutes into the reaction. Reducing the concentration by only a factor of two, prolongs the reaction time to twenty minutes, an increase by a factor of approximately 2^3. This could imply that the reaction follows third order kinetics.

There are other minor considerations that influence the quality of the synthesis. In general, it is better to inject the Te precursor in one injection. Multiple or slow injections result in the production of two or more species of particles. It is also noted that a Cd:Te ratio of 2:1 is ideal. Variations in Cd:Te ratio from 1:1 to 3:1 do not have significant effects on the quality of particles, but higher ratios cause polydispersity. Shorter chain phosphonic acids such as octylphosphonic acid (OPA) do not have the same inhibitory strength as ODPA, and thus lead to polydisperse samples too.

2.4. Te/Se Tetrapod/Rods: CdTe Tetrapod Cores with CdSe Rod Extensions.

Since reproducible and robust synthesis of CdTe rods is practically impossible, CdTe tetrapod cores with sufficiently long enough CdSe rod extensions on the tetrapod arms can potentially serve as an alternative structure for excellent charge separation. This type of morphology can only be synthesized by use of Cd/ODPA for growing both sections of the heterostructure: the CdTe tetrapod core and the CdSe rod extensions. CdSe will not grow as rod extensions if the radial surfaces of tetrapod arms are not already ligated by ODPA. Reaction of

104

Cd/ODPA and a Se precursor with CdTe tetrapods, that are grown by use of Cd/OA precursor, does not result in rod extension. Instead, TEM images have confirmed that the CdSe grows uniformly all over the tetrapod cores, making the tetrapods just "fatter". This is justifiably expected because the radial surfaces of the tetrapod arms are not bound and growth is unidirectional. Detailed synthetic procedures of both syntheses are listed in Appendix B: Selected Synthesis Protocols.

Figure 34 shows the progression of the absorption and emission spectra as Te/Se tetrapod/rods are grown. The lowest absorption band of the Te cores is at 670 nm with a corresponding photoluminescence band at about 690 nm. Similar to all other type II heterostructures, upon deposition and growth of CdSe over the cores, the charge transfer band appears in the absorption and emission spectra and it shifts to the red consistently. Emission from the CdTe cores is completely quenched with growth of first Se layer. With further charge separation as the particles grow, the CT band loses intensity and quantum yield of particles drops. These spectral changes were interpreted in section 2.2 for a very similar case, the Se/Te rod/rods.

A comparison between the Se/Te rod/rods (that was fully explored in section 2.2) with Te/Se tetrapod/rods presented in the current section reveals the benefits of a Te/Se rod-rod morphology even further. The molar ratio of the core chalcogenide to the shell chalcogenide in the synthesis of Se/Te rod/rods is 1:2. This same core:shell chalcogenide molar ratio in the Te/Se tetrapod-rods is 1:5.3. Looking at Figure 25, in case of Se/Te rod/rods, which have a shell that has twice as many moles of chalcogenide as the core, the charge transfer band has shifted all the way to 1 micron and has almost zero intensity. In case of Te/Se tetrapod/rods (Figure 34), which have a shell that has 5.3 times more moles of chalcogenide than the core, the charge transfer

band is shifted to only 925 nm and still has considerable intensity. Why is it that a much larger shell in Te/Se tetrapod/rods results in less charge separation in comparison to Se/Te rod/rods with relatively much smaller shells? The first obvious answer to this question involves morphology. Although a much larger amount of chalcogenide is reacted for growth of the shell in tetrapod/rods, that amount is actually split equally between the four arms of the tetrapods. Thus the correct comparison should be made between one arm of the tetrapod/rods and a rod/rod particle. However, this factor can be easily eliminated from the equation by comparing the spectra at the same quantum confinement; that is comparing a rod-rod particle to a tetrapod arm that is equal in size. Having this in mind, the green emission curve in Figure 25 shows a charge transfer band at 890 nm with barely 5000 counts. On the other hand, the blue emission curve in Figure 34 indicates a CT band at also 895 nm but has 25000 counts of intensity. Notice that the data in Figure 25 are obtained by having the entrance excitation and exit detection slits open much wider than the settings for data measurements in Figure 34. This will enhance the difference in intensity even more. However, since only a qualitative argument is being made, no proportional adjustments are needed to obtain the actual intensities. In any event, this comparison goes to show that even at the same quantum confinement (same size), better charge separation is observed in Se/Te rod/rods. This phenomenon is due to the relative size of the CdTe and CdSe sections and the electron and hole effective masses in CdTe versus CdSe. Although both discussed heterostructures are the same size, the CdSe section is the larger section in Se/Te rod/rods, and the smaller section in Te/Se tetrapod/rods. Electron and hole effective masses in CdTe and CdSe are very close to each other, about 0.1 for the electron and 0.4 for the hole. Because the effective mass of a hole is larger than the effective mass of an electron, the hole is tightly localized in the Te section, whereas the electron moves a little more freely in the Se

section. In case of the Se/Te rod/rods, even though the Te section is small, the hole is efficiently confined within the Te shell due to its larger effective mass. Thus, a higher degree of charge separation is obtained. Whereas in the case of Te/Se tetrapod/rods, the electron, having a lower effective mass, is not localized in the smaller Se section, and thus the charges don't fully separate. Building on this reasoning, Se/Te rod/rods have three advantages over Te/Se tetrapod/rods. First, a much lower molar amount of precursors is needed to achieve the same extent of charge separation. Second, having Se as the larger section of the heterostructure makes up for the low effective mass of electron in Se. And third, rod/rods are much easier to model mathematically than tetrapod/rods. Rods can be simply and accurately modeled by imposing cylindrical geometry, whereas tetrapods pose a more complicated mathematical problem.

2.5. Te/Se Core/Shells: CdTe Spherical Cores Covered with a Spherical CdSe Shell.

So far, we have discussed heterostructures that start with rod or tetrapod cores. Considering the fact that we are able to grow highly luminescent spherical Te cores that to the best of our knowledge have not been reported in the literature, it is of interest to investigate the properties of heterostructures that can be synthesized using these cores. Te/Se core/shells are prepared by putting a spherical shell over the Te spherical cores that were characterized in section 2.3.2. The Se precursor is prepared by dissolving 71.1 mg (0.9 mmol) of Se in 1.6 mL of TOP and 9 mL of ODE. This mixture is heated and stirred for 10 minutes at 80 $^{\circ}$C to obtain a clear colorless solution. The Cd precursor is made by dissolving 128.4 mg (1 mmol) of CdO in 1.26 mL (4 mmol) of oleic acid and 9 mL of ODE. This mixture is heated to 220 to 230 $^{\circ}$C until completely clear and allowed to cool to room temperature. The cores of the heterostructures are prepared just as explained before. 10 minutes after the Te injection, 0.5 mL of the Se precursor is injected drop-wise taking 1-2 minutes. The temperature is dropped to 230-240 $^{\circ}$C. Because there

is excess Cd left over in the reaction from the core precursor, there is no Cd injected the first round. Every round of injection after this consists of 0.5 mL of each of the Cd and Se precursors. The reactants are allowed to react for ten minutes after each round of Cd/Se injection and there are a total of eleven Cd/Se injections. Right before each round of injection, a 1 mL aliquot is drawn, diluted in 1 mL of toluene, and stored under nitrogen. Except for transient absorption (TA) experiments, these samples are used with no further processing. Sample purifications for TA studies are carried out exactly like the cores (explained in section 2.3.2).

TEM images have confirmed the growth of spherical CdSe shells over the Te core particles with each injection. Presence of cadmium in form of $Cd(OA)_2$ increases the reactivity of the precursor sufficiently to promote zinc blende growth of CdSe. The size of the final core/shell sample (i.e. 11th injection) is determined to be about 6.28 +/- 1 nm. Figure 35 shows TEM images from the cores, two subsequent core/shell samples, and an electron diffraction pattern of the final core/shell particles. By a comparison with previous literature[58,59], the diffraction pattern is determined to be that of a zinc-blende crystal structure confirming that the CdSe is deposited over the cores in spherical shells. Figure 37 shows the evolution of the absorption and emission spectra as more spherical Se layers are added. With the addition of the first Se shell, an intense charge transfer band appears in both the absorption and emission spectra. In addition, CdTe emission is completely quenched. With more Se shells deposited, the charge-transfer band shifts to the red consistently. The CT band also loses intensity which is consistent with the fact that as more Se shells are deposited, the hole becomes localized in the Te section while the electron is localized more in the Se section. As a result of the decreasing overlap of the electron and hole wavefuntions, the CT band loses oscillator strength and therefore intensity. As shown in Figure 37, by the eleventh injection where a Se shell of about 1.4 nm thick

is deposited, the CT band has almost no intensity.

The quantum yield of the particles also diminishes with increasing number of shells. Table 3 provides quantum yield numbers from the particular set of particles that is used to obtain the data presented in this chapter. As shown in the table, this particular set of cores has a QY of 58%. However, it should be emphasized that synthesizing cores with quantum yields of 70 to 80% can be easily achieved by following the synthetic method presented above. It was observed that, in general, the quantum yield increased with the first Se shell, probably due to the fact that the first shell passivates the surface of an already emissive core particle and suppresses non-radiative processes.

Table 3: Quantum Yield Measurements from CdTe Cores to Eleven CdSe Shells.

	Core-Spherical Shell QY (%)
CdTe Cores	58.4
1st Se Shell	66.5
2nd Se Shell	62.6
3rd Se Shell	42.8
4th Se Shell	32.4
5th Se Shell	21.7
6th Se Shell	18.2
7th Se Shell	13.5

8th Se Shell	9.3
9th Se Shell	8.6
10th Se Shell	6.4
11th Se Shell	5.2

2.6. Te/Se Dot/Tetrapods: CdTe Spherical Cores Covered with a Tetrapod CdSe Shell.

In order to achieve better charge separation than core/shells, one can attempt to synthesize Te/Se dot/rods by using a Cd/ODPA precursor for selenium growth. However, even under heavy presence of ODPA, dot/rod morphology is not attained. Instead, the particles have a dot/tetrapod morphology. In this case, after growing the spherical Te cores, the Se precursor is prepared by dissolving 189.3 mg (2.4 mmol) of Se and 801.6 mg (2.4 mmol) of ODPA in 1.0 mL of TOP, 1.0 mL of TBP and 9.6 mL of ODE. This mixture is heated and stirred for 10 minutes at 80 $^{\circ}$C to obtain a clear colorless solution. The Cd precursor is made by mixing 460.8 mg (3.6 mmol) of CdO, 2.405 g (7.2 mmol) of ODPA and 9 g of TOPO. This mixture is heated to 325 to 340 $^{\circ}$C until clear and allowed to cool. 12 mL of ODE is added to the mixture upon cooling to avoid solidification of the Cd precursor. The cores of the heterostructures are prepared just as explained in section 2.3.2. 10 minutes after the Te injection, half of the Cd precursor is injected into the reaction. The temperature is dropped but quickly brought back to 260 $^{\circ}$C. One twelfth of the Se precursor (approximately 1 mL) is injected as soon as the temperature reaches 260 $^{\circ}$C. The reactants are allowed to react for eight minutes before the next Se injection. There are a total of twelve Se injections. The other half of the Cd precursor is injected before the sixth Se

injection. Right before each Se injection, a 1 mL aliquot is drawn, diluted in 1 mL of toluene, and stored under nitrogen. Except for transient absorption (TA) experiments, these samples are used with no further processing. Sample purifications for TA studies are carried out exactly like the cores.

Figure 36 shows a TEM image of the final aliquot from the dot/tetrapod synthesis, confirming that use of the more tightly-binding ligand ODPA in the Cd precursor results in growth of wurtzite CdSe arms from the spherical zincblende CdTe cores. The reason for not forming dot/rods is that zinc blende Te cores are actually not exactly spherical. As explained earlier, the nuclei are tetrahedrons with four faces equivalent to the (1 0 0) plane in wurtzite, and thus four CdSe arms are grown from those planes to give a dot/tetrapod morphology. The final morphology of the heterostructure depends critically on the size of the CdTe core[60]. According to Scholes et al., smaller zinc blende Te cores tend to be more spherical, whereas larger ones tend to have more defined crystallographic faces on their surface. Thus, it is easier to obtain uni- or bi-directional growth from the smaller cores but, in larger Te cores, the growth direction is solely determined by the crystallographic planes. Although the starting Te cores in our case are relatively small (3.3 nm in diameter), a dot/rod morphology could still not be obtained. All syntheses with this protocol led to the formation of dot/tetrapod particles.

Figure 38 shows the consistent red-shift of the CT absorption and emission bands in addition to continuous loss of intensity as more CdSe is deposited to eventually grow dot/tetrapods. A comparison of the emission spectra in Figure 37 and Figure 38 reveals that for the same amount of Se deposited, the CT band in a core/ spherical shell heterostructure is more red-shifted than that of dot/tetrapod morphology. This is consistent with the fact that the three-dimensional quantum confinement energy of a spherical particle is smaller than that of an

elongated particle such as nanorods or tetrapods. One of the advantages of the dot/tetrapod synthesis is the complete suppression of CdSe individual nucleation. In the core/shell synthesis, there is always a small amount of individually nucleated CdSe towards the end of the reaction. This amount of nucleation can be safely neglected as it does not interfere with any of the spectroscopy. The next chapter presents transient absorption and emission data, radiative lifetimes, Auger and electron cooling dynamics in core/shell and dot/tetrapod heterostructures.

Chapter Three: Auger Dynamics and Electron Cooling Times in CdTe/CdSe Nano-heterostructures

Existing photovoltaics (PVs) produce band edge electron-hole pairs from the absorption of solar photons. The solar spectrum is broad and many of the absorbed photons have energies greatly exceeding the semiconductor bandgap. Upon relaxation of the electron and hole to the band edge, the excess photon energy is dissipated into the phonons and lost. Use of the photon energy in excess of the bandgap could make for far more efficient PVs. One of the ways in which the loss of this energy could be avoided is carrier multiplication. Carrier multiplication is a process in which the excess energy in a single electron-hole pair is used to create additional electron-hole pairs. This process can, in principle, increase the current in a PV cell. This chapter will address the rates and mechanisms of Auger recombination of multiple excitons. Multiple excitons are produced by carrier multiplication. Auger recombination is the opposite process of carrier multiplication: two excitons produce one exciton with excess energy. Thus, Auger recombination is a process that diminishes the gains brought about by carrier multiplication. This chapter elucidates the electronic properties of CdTe/CdSe semiconductor core/shell and dot/tetrapod nanoparticles that control the dynamics of Auger recombination. Auger processes are partly controlled by the electronic coupling between the spatially separated electron and hole and it is this aspect of the dynamics that will be studied.

Another way to avoid the loss of the energy of absorbed photons in a PV is to enhance hot electron transfer, a process in which the nascent electron is extracted from the semiconductor prior to its energy being lost to heat. However, there are competing processes such as electron

cooling (EC) that occur on a much faster timescale than hot electron transfer. Previous studies indicate that EC in strongly quantum confined semiconductor nanoparticles typically occurs in 1 to few ps[61,62,63,64]. EC rates strongly depend on the coulombic interaction between the electron and hole. The morphology of the heterostructures determines the extent of charge separation. It is expected that as the electron and hole become more spatially separated in type II heterojunctions, EC processes should get inhibited. A study on the rates of EC as a function of electron-hole coupling is presented.

Instrumentation. Time-resolved luminescence measurements presented in this chapter are obtained by time-correlated single-photon counting (TCSPC), using an MPD (Micro Photon Devices) PDM series single photon counting detector and a Becker-Hickel SP-630 board. The light source is a cavity-dumped Ti:sapphire laser (Coherent Mira) operating at 410 nm with a 1 MHz repetition rate. In all cases, the fluorescence is focused through a 0.25 m monochromator with a 150 groove/mm grating and onto the detector. The monochromator has a polarization scrambler in front of the entrance slit, which almost completely eliminates the polarization dependence of the monochromator throughput. Transient absorption spectra are obtained by a pump-probe method, with a Clark-MXR YAG-laser pump source that generates 150 femtosecond pulses allowing for sub-picosecond resolution.

3.1. Modeling the Electron and Hole Wavefunctions and Auger Rate Calculations

One of the main goals of this chapter is to understand what properties of the nanoparticles control the electron cooling, electron transfer and Auger recombination dynamics. Calculations are particularly relevant to the Auger recombination dynamics. Comparisons of calculations with experimental results will help elucidate the role of electron and hole overlap and interaction energies in determining Auger recombination and electron cooling rates. Auger calculations

require reasonably accurate electron and hole wavefunctions. Electron and hole wavefunctions are calculated by modeling the system as a simple particle-in-a-sphere that has the Hamiltonian of the following terms: $H = \frac{p^2}{2m} + V(r)$, where p is the momentum operator, m denotes the mass of the particle, and V(r) is the spherically symmetric potential well with soft outside walls. These wavefunctions will be calculated using the effective mass approximation (EMA), in which the effective mass of the charge carrier is the mass it seems to carry while being transported in a crystal lattice. Once the electron and hole wavefunctions are calculated, the overlap between the electron and hole wavefunctions can be obtained. This calculated overlap value must be directly proportional to the intensity of the CT absorption band and to the energy of the absorption/emission band (absorption/emission peak position), and inversely proportional to experimental radiative lifetimes. Thus, the accuracy of these relatively simple calculations will be assessed by comparison of calculated and experimental absorption or emission onsets, absorption intensity, and radiative lifetimes.

Following Cragg and Efros[65], the Auger recombination rate is proportional to $|\Psi(k_A)|^2$ where $\Psi(k)$ is the Fourier transform of the receiving particle (electron or hole) wavefunction and k_A is the wavevector corresponding to the Auger (in this case bandgap) energy. Following Fourier transformation of the electron and hole wavefunctions, the magnitude of $|\Psi(k_A)|^2$ can be evaluated. The procedures used to calculate these quantities are discussed below. All calculations are performed by a FORTRAN program. The raw FORTRAN code is presented in Appendix C: FORTRAN Code. This code is a more general program that also calculates Raman spectra, band-bowing effects, and other optical properties that are not directly relevant to this dissertation. All of the program in presented anyway to keep the integrity of the code.

Before discussing the details of the calculation, it is necessary to consider the compression effects that result from depositing a smaller-lattice shell onto a larger-lattice core. The lattice parameter of CdTe's crystal structure is 0.65 nm, while that of CdSe is 0.61 nm. Since CdTe's lattice is about 7.6% larger than that of CdSe, depositing a layer of CdSe shell over CdTe cores, compresses the cores, and stretches the shell (Figure 39). The core is under uniform radial compression while the shell experiences tensile strain in tangential directions and compressive strain in the radial direction. At first, it might seem that the compression effects resulting from this lattice mismatch can be safely neglected in calculations. However, a significantly better match with experimental data is obtained when compression effects are taken into account. CdTe's bandgap energy increases because of compression and CdSe's gap energy decreases due to tensile strain. And in general, effects are larger for smaller cores as they are more compressible. Effects can be as large as 3000 cm^{-1} for thicker shells. Lattice compressibility is high in both CdTe and CdSe due to their low bulk moduli (42.4 GPa for CdTe and 53.1 GPa for CdSe). Lower moduli means that the particle can endure more stress and compress elastically instead of breaking or relaxing by forming defects.

The change in bandgap energies is proportional to the induced strain. That is, $\Delta E_g = C\,P$, where C is a constant and P is the pressure induced from the compression/ tensile strain. A continuum elasticity model is applied to calculate the compression or strain in the core and shell material and then bandgap of the heterostructure is calculated using the model-solid theory[66]. In these calculations, bulk material parameters are used. The strain caused by the lattice mismatch is calculated by Weller's method[67] where the core/shell system is modeled as a sphere enclosed in a concentric sphere of different lattice parameter and elastic moduli.

Within the effective mass approximation (EMA), the usual way of calculating a

wavefunction for a core/shell particle is to express the wavefunction on both sides of the core-shell interface as a linear combination of spherical Bessel and Neumann functions[68]. The constants are evaluated by imposing continuity of the wavefunction and probability current at the interface. It is difficult to handle diffuse interfaces with this method. However, this is not a problem in this case as the junction between the Te and Se sections is a sharp interface. The calculations discussed below are done in a more general way: the wavefunction is expanded in a series of zero-order Schrödinger wave equation (SWE) solutions, and the constants then evaluated. This calculation has the problem of a position dependent effective mass. (This problem may be neglected in Te/Se heterostructures because the electron and hole effective masses are basically the same in CdTe and CdSe, respectively. The equations below model a more general type of heterostructure.) Thus, simply writing the SWE in the usual way with a position dependent mass, results in a non-Hermitian kinetic energy operator. The SWE may be written as follows.[41]

$$-\frac{\hbar^2}{2m_0}\nabla\frac{1}{m*(r)}\nabla\Psi + V(r)\Psi = \left(-\frac{\hbar^2}{2m_0}\right)\left((1/m*(r))\nabla^2\Psi + \nabla(1/m*(r))\bullet\nabla\Psi\right) + V(r)\Psi = E\Psi$$

Where m_0 and m* are the electron mass and the effective masses (in units of electron mass), respectively. The effective mass can be taken to be a linear function of the radially-dependent composition. Specifically,

$$m*(r) = m_{core}^* + (m_{shell}^* - m_{core}^*)C(r)$$

The wavefunction is expanded in a set of zero'th order spherical Bessel functions.

$$\Psi = \sum_n C_n j_0(k_n r) \text{ where, as above, } k_n = \sqrt{2mE_n}/\hbar \text{ and } k_n R = n\pi$$

Unlike the case in which the mass is position independent, this generates off-diagonal kinetic energy matrix elements. The C_n coefficients are obtained by diagonalizing the sum of the kinetic

and potential energy operators. Specifically,

$$V(i,j) = \int_0^{R_f} r^2 dr \, V(r) \, j_0(i\pi r/R_f) \, j_0(j\pi r/R_f)$$

$$T(i,j) = \frac{\pi^2 \hbar^2}{2m_0 R_f^2} \int_0^{R_f} r^2 dr \, (1/m^*(r)) \, j_0(i\pi r/R_f) \, j_0(j\pi r/R_f), \text{ and}$$

$$T_1(i,j) = \frac{\hbar^2}{2m_0} \int_0^{R_f} r^2 dr \, j_0(j\pi r/R_f) \, d(1/m^*(r))/dr \, d\left(j_0(i\pi r/R_f)\right)/dr \quad \text{where } R_f \text{ is the outer}$$

radius of the calculation. These integrals are performed numerically, with R_f taken to be sufficiently larger than the shell radius that the exact choice of R_f doesn't matter – it is larger than the extent to which the wavefunction penetrates out of the particle. The matrix to be diagonalized is the sum $V+T+T_1$. The eigenvalues are the electron or hole energies and the eigenvectors are the C_n coefficients of the electron or hole wavefunctions. This approach gives continuity of the wavefunction and of probability current without explicitly considering the core/shell boundary conditions. Electron-hole coulombic interactions give a relatively small term that is added as a perturbation. EMA calculations often over-estimate the extent of quantum confinement, that is, the calculated kinetic energy terms are often too large. Because of this, it may be necessary in some cases to scale these terms to get the correct core particle absorption onset. If this is necessary, then the same scaling should be applied to the core/shell particle calculation. While the problems associated with the effective mass approximation are well known, the bottom line is that these calculations provide sufficiently accurate electron and hole wavefunctions that meaningful relative Auger rates can be calculated.

Once the electron and hole wavefunctions are calculated, the relative Auger rates can be obtained by Fourier-Bessel transformation of the wavefunctions. The basic assumption is that the wavefunctions can be described as linear combinations of spherically symmetric (l=0) particle-

in-a-sphere functions. The different amounts of the high frequency components necessary for momentum conservation are derived from these wavefunctions and are related to the sharpness of the core-shell interface. To evaluate these momentum components, momentum representations of the electron and hole wavefunctions are needed. These are obtained by a Fourier-Bessel transformation: $\bar{\Psi}(k) = \int_0^\infty r^2 dr\, \Psi(r)\, j_0(kr)$

To obtain the relative Auger recombination rates, $\left|\bar{\Psi}(k)\right|^2$ is evaluated at the momentum, k_A, corresponding to the band-gap energy, E_a. Specifically, $k_A = (m_0)^{1/2}\,(2m^*E_A)^{1/2}/\hbar$, where m_0 and m^* are defined as above and E_A is the Auger (in this case bandgap) energy. Interface sharpness, surface defect states, and charged ligands adsorbed on the surface can contribute to producing significant amplitudes of $\left|\bar{\Psi}(k)\right|^2$ at k_A. Because of the differences in effective mass, different values of k_A are obtained for the electrons and holes. CdTe-CdSe (II-IV in general) semiconductors have much lighter electrons than holes. Larger values of k_A are therefore calculated for the holes. This suggests that it is the electrons that are the receiving particles in an Auger recombination process. For a typical particle having a bandgap energy of 17240 cm^{-1} (580 nm) and an electron effective mass of $0.11m_0$, a k_A value of 2.49 nm^{-1} is calculated.

The above discussion is specific to calculations on spherical particles. Thus, Te/Se core/shells can be easily modeled by this method. Similar calculations can be performed for nanorods, having cylindrical morphologies. In the cylinder case, the z and r coordinates separate and the total wavefunction is simply the product of the radial and longitudinal wavefunctions. However, calculating the electron and hole wavefunctions in a dot/tetrapod particle is a much more difficult problem mathematically, and has been avoided.

Dynamics in CdTe/CdSe core/shell heterostructures characterized in section 2.5 are

modeled using the method described above. Experimental emission onsets, CT band absorption intensity, and radiative lifetimes are assessed to assure the accuracy of the calculated electron and hole wavefunctions via this approach. In order to input the radius of the core and shell sections into the FORTRAN program, particle sizes are determined from TEM images. Figure 40 shows a graph of particle size determined from TEM images as a function of number of Se shells. Figure 40 also shows a calculated curve of emission peak position generated by entering different particle sizes into the program. This generated curve matches the experimental emission peaks closely. The particle size measurements obtained from TEM imaging, entered into the program as starting parameters, determine the potential well boundaries for wavefunction calculations. Figure 41 shows a comparison between the experimental CT band absorption intensities and the calculated overlap functions, and experimental and calculated radiative lifetimes. The close agreement between the experimental and calculated values confirms that the calculated wavefunctions using a simple EMA model are accurate.

Experimental radiative lifetimes are obtained by measuring the total time-resolved fluorescence decay curves, fitting them into a bi-exponential, and then extracting the radiative lifetime using quantum yields. Assuming that the fluorescence decay curves have two components then the curve can be expressed in terms of a bi-exponential function, where k_1 and k_2 are the total fluorescence rates from each component:

$$y(t) = A_1 e^{-k_1 t} + A_2 e^{-k_2 t}$$

A_1 and A_2 are the respective decay amplitudes of each component. Quantum yield is defined as the ratio of radiative rate to total decay rate. Total decay rate is the sum of k_{rad} and k_{n-rad}, which are the radiative and non-radiative rates, respectively.

$$QY = \frac{k_{rad}}{k} = \frac{k_{rad}}{k_{rad} + k_{n-rad}}$$

Quantum yield can also be expressed as the weighted sum of two quantum yields, corresponding to the two components in the bi-exponential.

$$QY = \frac{A_1}{A_1 + A_2}QY_{(1)} + \frac{A_2}{A_1 + A_2}QY_{(2)}$$

This can be expanded further by expressing the quantum yields as the ratio of radiative rate over total decay rate. Substituting $t = {}^1/_k$ yields:

$$QY = \frac{A_1}{A_1 + A_2}\left(\frac{k_{rad}}{k_1}\right) + \frac{A_2}{A_1 + A_2}\left(\frac{k_{rad}}{k_2}\right) = \frac{A_1}{(A_1 + A_2)(t_1 \cdot k_{rad})} + \frac{A_2}{(A_1 + A_2)(t_2 \cdot k_{rad})}$$

Solving for k_{rad} gives radiative lifetime, τ_{rad}, as follows:

$$\tau_{rad} = \frac{1}{k_{rad}} = \frac{1}{QY\left(\frac{A_1 t_1 + A_2 t_2}{A_1 + A_2}\right)}$$

Thus, the experimental radiative lifetimes shown in Figure 41 are obtained by simply measuring the quantum yield, and decay curve of each sample, and then using the equation above to solve for τ_{rad}.

Calculated radiative lifetimes are obtained by solving for the overlap function numerically using the FORTRAN code discussed above, and multiplying that value by frequency cubed. Recall that the rate of spontaneous emission, or the radiative rate, in a transition is defined by Einstein A coefficient, which is directly proportional to the oscillator strength and frequency of the transition cubed.

$$k_{rad} = A_{12} = \frac{v^3 |\mu_{12}^2|}{3\pi\varepsilon_0 \hbar c^3 \, \boxed{\boxed{}}}$$

, where v is the frequency of the transition, μ_{12} is the transition dipole moment or the overlap function, ε_0 is the permittivity of free space, $\hbar$ is the reduced Planck constant, and c is the speed of light. Upon calculation of the wavefunctions and their overlap value, values of $\frac{1}{v^3 |\mu_{12}^2|}$ for

each core/shell sample with a specific shell thickness are obtained. $\frac{1}{v^3 |\mu_{12}|^2}$ is proportional to and scales like the radiative lifetime. Radiative lifetime of the charge-transfer transition in Te/Se heterostructures, which is inversely proportional to Einstein A, increases as the Te section grows due to diminishing overlap of electron and hole wavefunctions.

It is expected that in dot/tetrapods, the radiative lifetime should be longer than core/shells due to a smaller overlap of the wavefunctions. However, the experimental results show that, for the same amount of quantum confinement, a generally shorter radiative lifetime for dot/tetrapods in comparison to core/shells. As seen in Figure 42, this experimental result is in contradiction with what is expected. As mentioned previously, modeling dot/tetrapods is a much more difficult problem mathematically, and thus no attempt has been made to do a numerical calculation of the wavefunctions in dot/tetrapods. One point to realize is that final heterostructures evolve from a dot-in-a-tetrahedron and eventually grow into a dot/tetrapod. As seen in Figure 36, even the fully grown dot/tetrapods have a very low aspect ratio and remain "pointy". The higher electric field intensity at the tips of the dot/tetrahedrons or pointy corners of dot/tetrapods could potentially have significant effects on the electron wavefunction.

3.2. Experimental and Calculated Auger Dynamics in Core/Shells and Dot/Tetrapods

Auger recombination is a process by which an electron and hole recombine, giving the excess energy to another particle, either an electron or a hole. Auger processes occur when the particle has more than one exciton. Te/Se heterostructure particles can undergo Auger recombination of bi-excitons or multi-excitons, produced by having absorbed more than one photon. Multi-excitons can also be produced by carrier multiplication (CM), a process whereby a

semiconductor absorbs a high-energy (blue) photon and undergoes an inverse Auger process to produce two or more excitons[62]. Auger recombination dynamics are the main loss mechanism for biexcitons and are therefore of central importance in PVs based on semiconductors in which CM occurs. Auger processes reduce the efficiency of carrier multiplication and it is therefore important to understand what nanoparticle properties control the Auger rates.

Despite their importance in several aspects of nanoparticle photophysics, Auger processes in nanoparticles are not well understood[69]. Very fundamental questions have not been resolved and an attempt is made to address these questions here. In the case of Auger recombination following multi-photon excitation or carrier multiplication, it is not even clear what the 'receiving particle' is. It could be the electron. Electron excitation to the continuum causes ionization and hence is believed to cause particle charging in single-particle studies[70]. Alternatively, it could be the hole. Which is the receiving particle is unknown because there is very little direct evidence regarding what aspects of the nanoparticle control the Auger rates in any type of semiconductor nanoparticles.

There are two main factors that influence the Auger rate in a semiconductor: electron and hole interaction, and momentum conservation. Since an Auger process involves both electrons and holes, the extent of electron-hole overlap is an important factor and the Auger rates will be slower in type-II particles[71,72]. However, factors such as the nature of the interface in core/shell particles may also be relevant. This inference is consistent with a 2010 theoretical paper by Cragg and Efros which is particularly insightful in understanding momentum conservation in Auger processes[65]. The basic considerations are as follows. Auger processes are very slow in bulk materials because of momentum conservation. Specifically, a biexciton has both electrons and holes in zero momentum states. Following receiving the recombination energy, the excited

electron or hole must have the appropriate momentum, p=(2mE)$^{1/2}$. In bulk materials, this momentum must come from the phonons, which is why Auger recombination is slow. However, in nanoparticles the Auger excited particle can conserve momentum by its initial wavefunction having the appropriate momentum components. These momentum components result from rapid spatial changes in the ground state wavefunction. In the case analyzed by Cragg and Efros, the hole is the receiving particle in an ionized particle. The Auger rate is found to be proportional to $\left|\bar{\Psi}_{(k_A)}\right|^2$ where $\bar{\Psi}_{(k)}$ is the Fourier transform of the receiving particle (electron or hole) wavefunction and k_A is the wavevector corresponding to the Auger (in this case bandgap) energy. This paper considers the possibility that the high frequency Fourier components are due to the sharp core/shell boundary and shows that the magnitude of $\left|\bar{\Psi}_{(k_A)}\right|^2$ decreases rapidly as the core/shell interface becomes diffuse. Another possibility is that the high frequency Fourier components result from surface defects and or charged surface ligands, which put rapidly varying kinks in the electron wavefunction. A graduate student in our lab, Cory Sobotta is currently varying the sharpness of the interface and the density of surface defects systematically and independently. By studying Auger dynamics in different types of particles, the effects of having a high barrier confining the electron to the core are compared to a high barrier confining the hole. For example, in the case of CdTe/CdSe, the electron is weakly confined to the shell. It will therefore have minimal high-frequency components in the lowest conduction band wavefunction. Thus, the crucial factor determining Auger rates in Te/Se heterostructures is not momentum conservation, but rather the electron-hole interaction. Data presented in this section reveals the role of electron-hole interaction energy in Auger dynamics.

Femtosecond transient absorption (TA) measurements are used to elucidate the relaxation and recombination dynamics of multiexcitons in CdTe dots and CdTe/CdSe core/shells and

dot/tetrapods. The transient spectra show the effects of state filling and exciton-exciton coulomb interactions. State filling, i.e. when the state cannot take any more electrons, leads to bleaching of the allowed optical transition and gives a diminished absorbance. Coulombic interactions between excitons result in a decrease in the energy of the biexciton state, thereby red shifting the absorption. The absorption difference (transient minus static) spectra are typically reported and simply referred to as "TA spectra". These spectra usually exhibit a derivative-like feature due to the combination of state filling and coulomb interactions. In the case where the lowest conduction band level is only partially filled (having one, rather than two, electrons), then the bleach and the red-shifted positive absorbance band are both observed. Due to overlap of these positive and negative spectral features, the bleach will appear shifted to the blue of the static absorption peak. Complete filling of this level results in only the bleach feature in the TA spectra. The kinetics of these spectral features gives the time-dependent electron populations in different conduction band levels. Thus, the analysis of TA kinetics at different wavelengths can be used to extract the dynamics of excitons in the corresponding conduction band states. The degeneracy of the valence band is such that the kinetics are insensitive to the hole dynamics. Thus, TA dynamics at the charge transfer band (or the X0 band) help determine the rates of Auger recombination in the cores and the heterostructures. Because the CT band has almost no intensity after the sixth shell, TA measurements are performed on cores and first six core/shells and dot/tetrapods.

Upon excitation and creation of multiexcitons, the bottom of the conduction band state is filled almost instantaneously (less than 10 ps). This is indicated by the fast appearance of the bleach feature in the TA spectra. At this point, no more electrons can be excited/ relaxed to the bottom of the conduction band unless some of the already formed excitons recombine via Auger

recombination to "empty" the lowest conduction band state. Thus, the rate of continuing state filling (or exciton creation) should be equal to Auger rate. This continuous but at the same time decreasing rate of state filling is signified by the diminishing bleach feature in the TA data. Therefore, the decay rate of the bleach feature is the Auger rate. In this context, Auger time can be thought of as the lifetime of the biexciton or multiexciton state. Figure 43 shows sample absorption difference spectra obtained from CdTe cores and the corresponding TA dynamics at the bleach position (~ 550 nm). The bleach feature at about 550 nm corresponds to the filling of the charge-separated state. The X0 (or charge-transfer state) bleach dynamics curves obtained for cores and first six core/shells are each fitted to a bi-exponential function. The short component of the bi-exponential function represents the Auger recombination times, and the rise time (delayed filling of the lowest conduction band state) of the dynamics curve corresponds to electron cooling times, which will be discussed in the next section. Figure 44 depicts the experimental and calculated Auger times. As expected, the Auger time increases with decreasing electron-hole overlap as the Se shell becomes thicker. However, it was found that the overlap alone does not predict the experimental Auger times accurately. Rather, the coulombic interaction energy between the 1s electron and the 1s hole wavefunctions closely matches the experimental results. It is this calculated interaction energy that is presented in Figure 44.

Dot/tetrapods or any other elongated morphology of Te/Se heterostructures are expected to have longer Auger times due to larger charge separation and thus smaller overlap. However, as presented in Figure 45, the increasing trend of Auger times in dot/tetrapods is generally similar to that of core/shells. As mentioned previously, the dot/tetrapods discussed here are not large aspect ratio and therefore, electron and hole wavefunctions cannot be calculated using a particle-in-a-cylinder model. Ultimately, without having any reliable calculations to back up the

measurements, it is hard to interpret the experimental data.

Depending on the monochromator window, the TA data from core/shells and dot/tetrapods show other bleach features. Figure 46 is an example of TA data from a dot/tetrapod sample with three Se shells. The lowest energy bleach (or the X0 band) is easily assigned to the charge transfer state. However, the assignment of higher energy states (X1 and X2 bands) remains unknown. It is of particular interest to be able to assign the higher bands as they exhibit interesting dynamics. Preliminary analyses performed on X1 band TA data suggests that the dynamics remain constant with varying shell thickness. In contrast, the X2 band exhibits size dependent dynamics. If X2 band is assigned successfully, the dynamics can shed light on the behavior of multi-excitons in semiconductor heterostructures.

3.3. Electron Cooling Time Measurements

There are two main processed that control the dynamics of the electron and hole: Auger recombination discussed in previous section and interfacial hot electron transfer (ET). The latter is depends on the rate of electron cooling and rate of carrier trapping at surface defects or adsorbed species, both of which compete with the rate of ET. For hot electrons to be efficiently captured by adsorbed acceptors, the electron transfer rate must exceed the electron cooling rate. Since interfacial electron transfer is a mechanism for raising the efficiency of PV cells, it is desirable to suppress the competing electron cooling and carrier trapping processes to maximize ET.

The rates of electron cooling (EC) can be examined using several different types of femtosecond methods. Most commonly, EC rates are determined by measuring the kinetics of state filling of higher lying conduction band states, delayed filling of the lowest conduction band level and the kinetics of the red-shifted band edge absorption or by intraband absorption

127

measurements. It was originally expected that this process would be very slow because of a "phonon bottleneck"[73,74,75]. However, many studies have shown that electron cooling in II-VI semiconductor nanoparticles is mediated by electron-hole (and in some cases, electron-electron) interactions[76,77]. Previous studies indicate that EC in strongly quantum confined semiconductor nanoparticles typically occurs on the timescale of 1 to a few ps[61,62,63,64]. In the absence of electron-hole interactions, much slower EC is observed. The rate gets progressively slower as the hole becomes more deeply trapped and hence more localized[78,79]. When the hole is completely removed, the EC rate depends on the nature of the surface ligands[80,81]. The question of the relaxation mechanism in the absence of, or with limited interaction with the holes can be addressed by studies of electron cooling in type-II heterostructures. Type-II heterostructures have little electron-hole overlap and little coupling, so EC will be much slower in type-II particles. Electron cooling in type-II Te/Se particles with varying degrees of charge separation is examined in this section. Initially, CdTe/CdSe core/shell spheres having different shell thicknesses are studied. CdTe/CdSe dot/tetrapods are also examined. In the latter case, greater charge separation occurs, while holding the amount of CdSe constant. Greater charge separation is expected to result in slower dynamics[82,83].

Femtosecond studies on the spherical core/shell particles show that TA features to the blue of the absorption onset (the bandgap excitation for thin shells and the CdSe localized excitation for thick shells) decay rapidly, but the decay rate decreases with increasing shell thickness. The same may be said of the Stark-shifted band edge absorption. This indicates that electron cooling slows dramatically in these type-II CdTe/CdSe core/shell particles as the shell gets thicker and the extent of charge separation increases. Figure 47 (top graph) shows the experimental electron cooling times measured in these core/shells. These preliminary results

suggest that hot electron transfer to surface adsorbed acceptors may dominate electron cooling even in well passivated particles. Thus, it may be possible for ET to effectively compete with electron cooling in Te/Se systems, even when the particle surface is passivated with a thin shell of another semiconductor.

Figure 47 (bottom graph) shows a comparison between the electron cooling times in core/shells and dot/tetrapods as a function of shell thickness or quantum confinement. Contrary to expectation, dot/tetrapods not only do not exhibit slower EC dynamics than their core/shell counterparts, but show much faster EC rates especially for thicker shells. At this point, it should be abundantly clear that the dot/tetrapods are peculiar in that experimental data such as radiative lifetimes, Auger rates, and electron cooling rates all produce results that are counterintuitive. It seems that a simple prediction of dynamics based on morphology can be misleading. This highlights the need for the exact calculations of wavefunction in these structures, which is unfortunately mathematically extremely complicated.
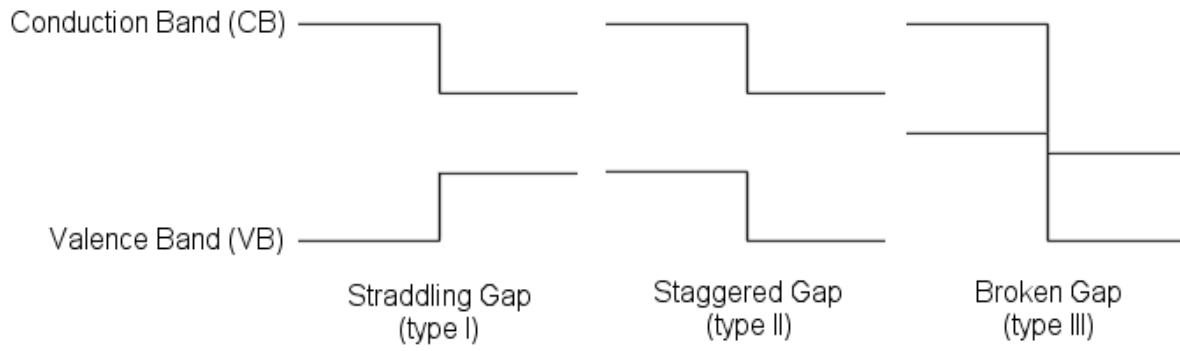
Figure 22: The Band-gap Alignment in Three Possible Types of Semiconductor Heterostructures.
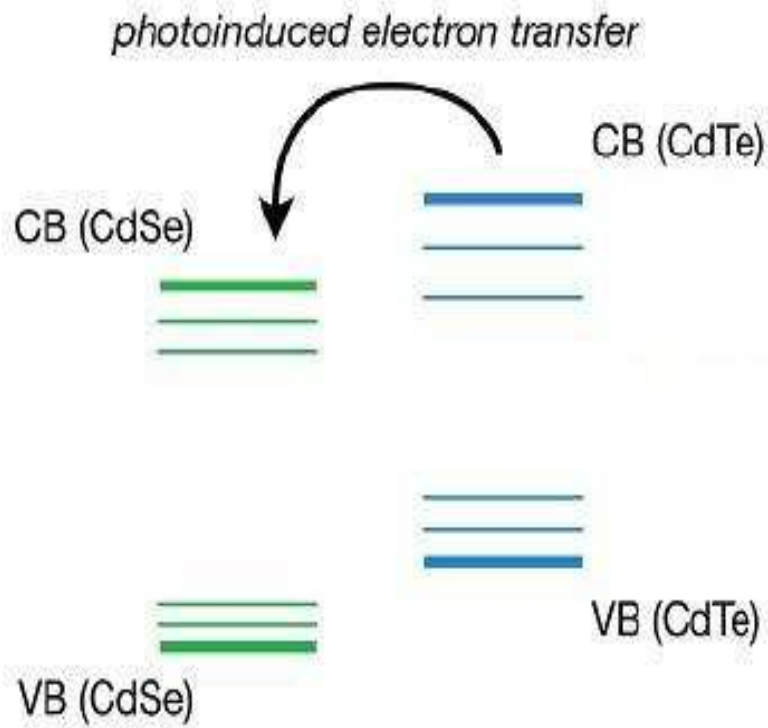
Figure 23: Schematic Band Diagram of CdTe/CdSe Nanoheterostructures. Multiple lines show the various levels in the conduction and valence bands.
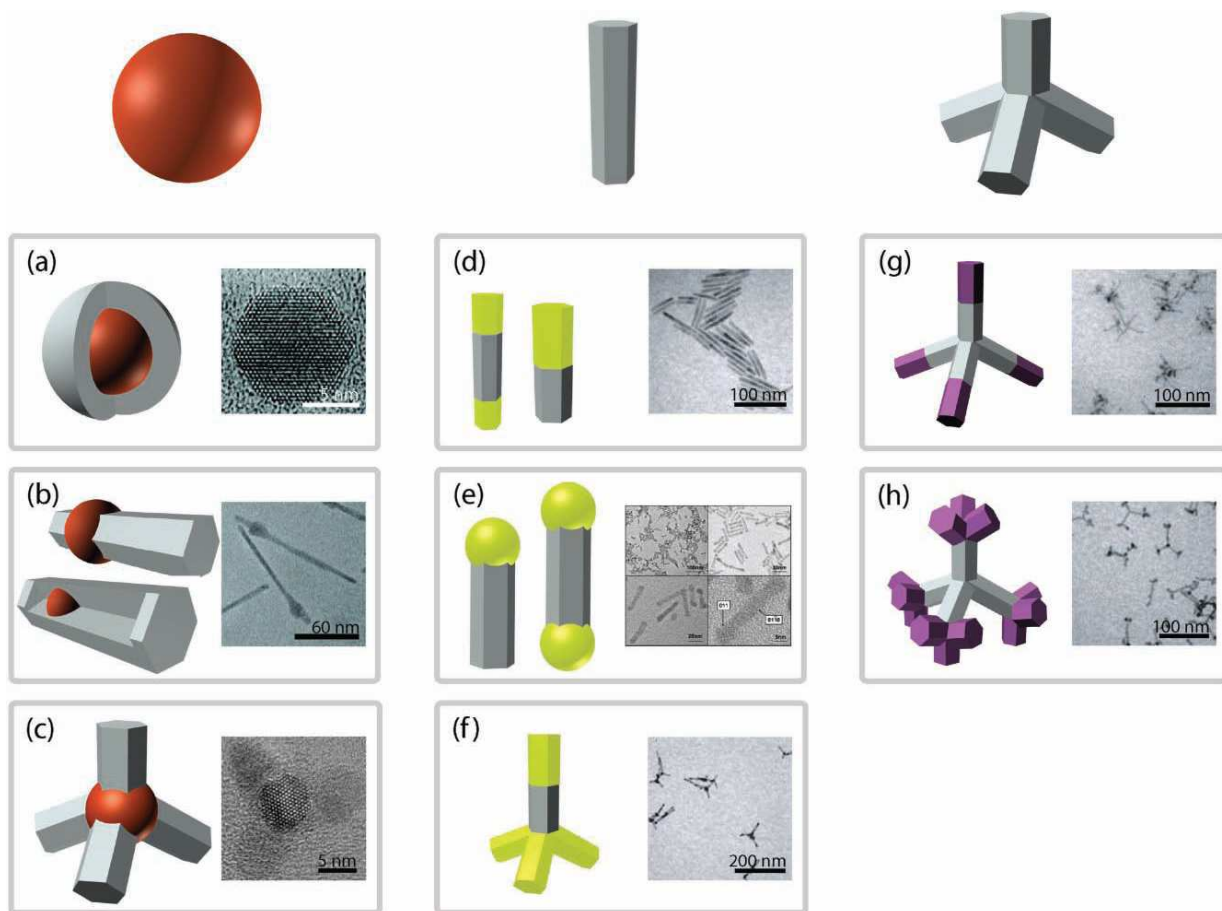
Figure 24: Various Possible Morphologies of CdTe/CdSe Nanoheterostructures, With the Morphology of the Core Shown at the Top of Each Column*.

*Adv. Mater. **2011**, *23*, 180
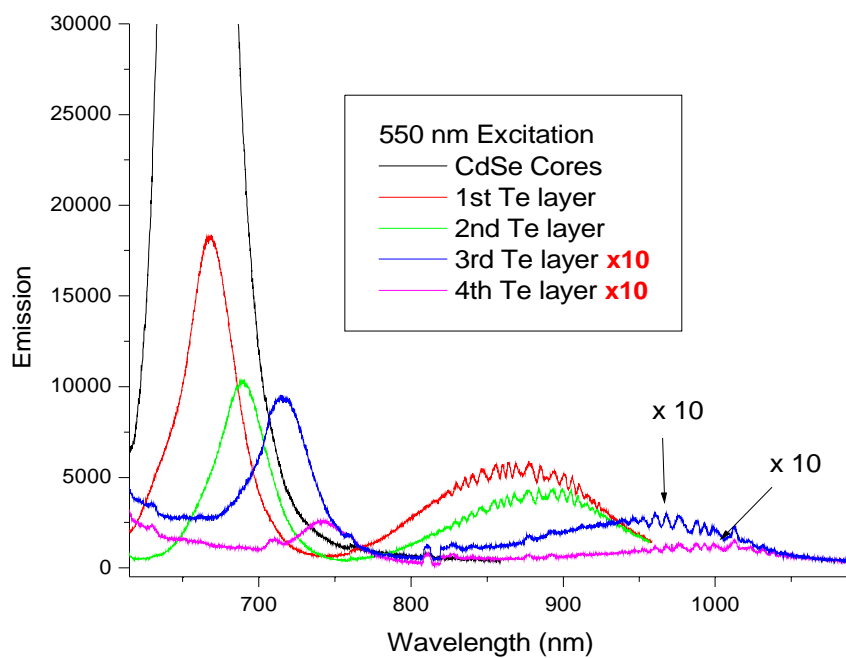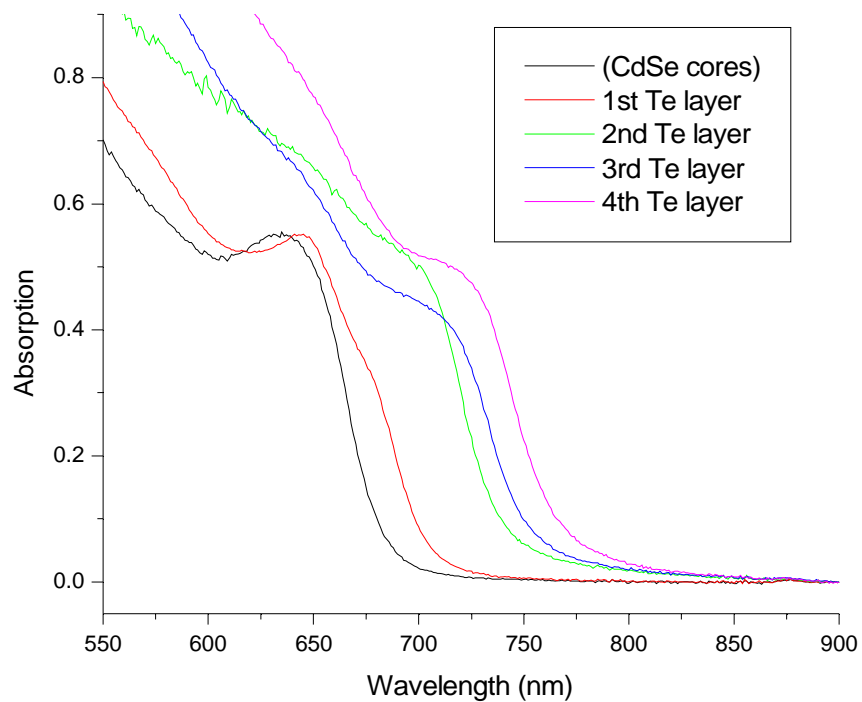
Figure 25: Absorption and Emission Spectra of CdSe/CdTe Rod/Rods. Layers do not correspond to monolayers but rather to each injection shell.
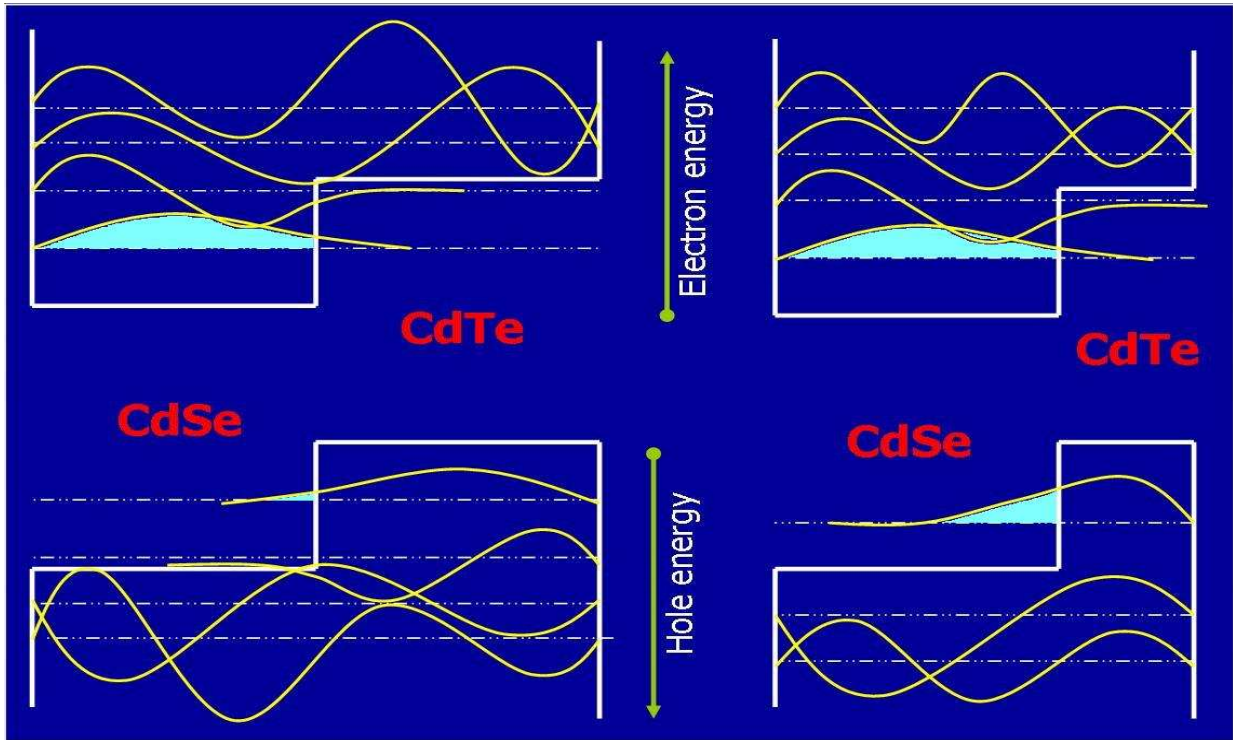
Figure 26: Schematic Diagram of Electron and Hole Wavefunctions in CdSe/CdTe Rod/Rods. Right column represents a smaller Te cap and left column represents a full grown Te rod shell.
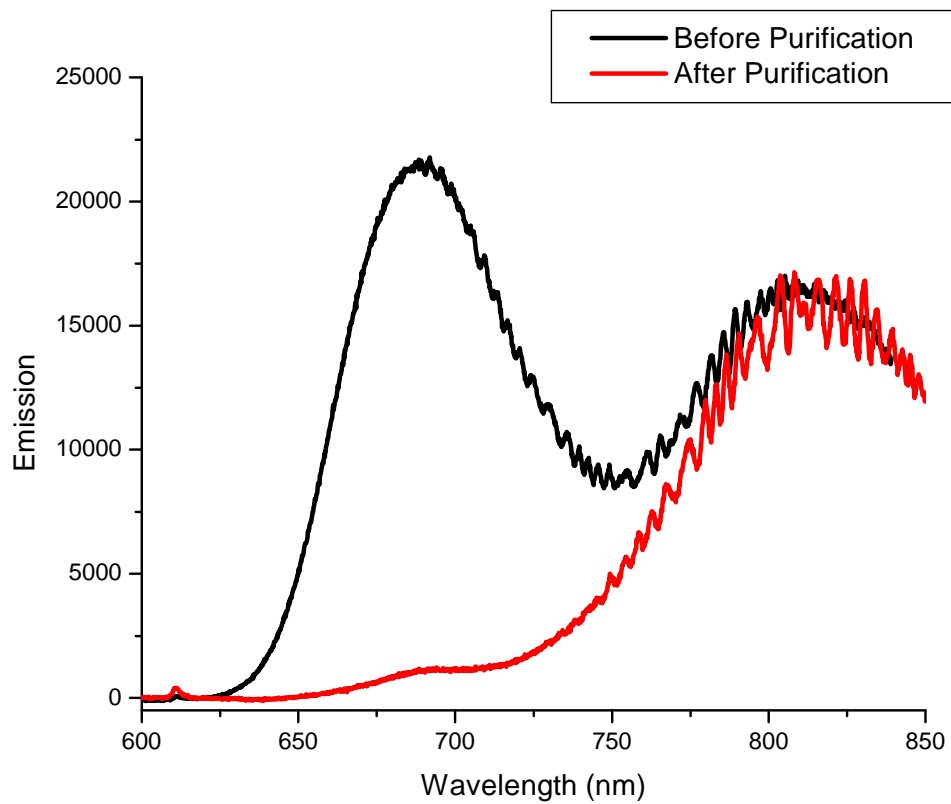
Figure 27: CdSe/CdTe Heterostructures Before and After Purification by Size-selective Precipitation.
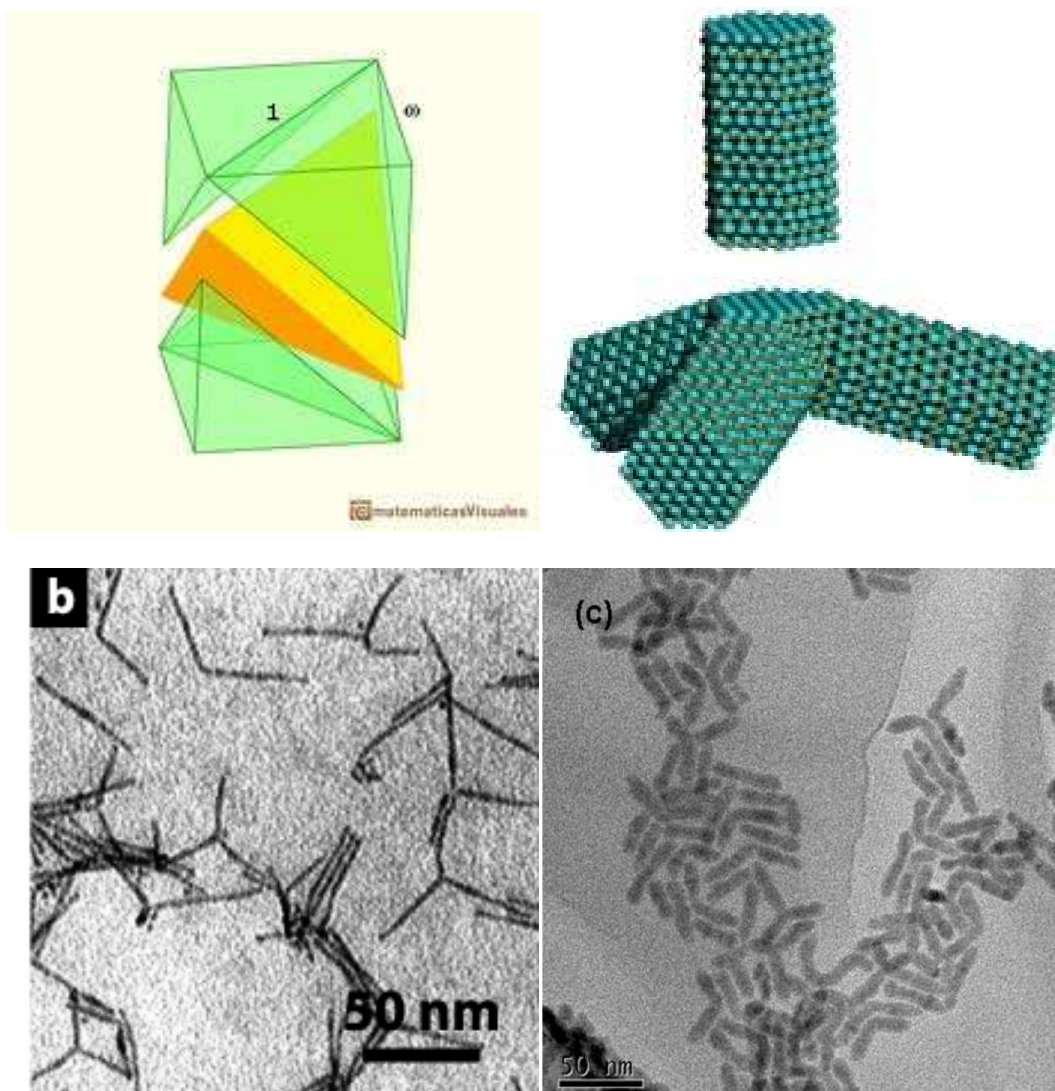
Figure 28: A Schematic of Zinc Blende Tetrahedron CdTe Cores and the Successive Growth of Wurtzite Arms (a) and TEM images of CdTe rods (b,c)[*][†].

J. Phys. Chem. B. **2005,** *109,* 8539
† *Chem. Mater.* **2009,** *21,* 1467
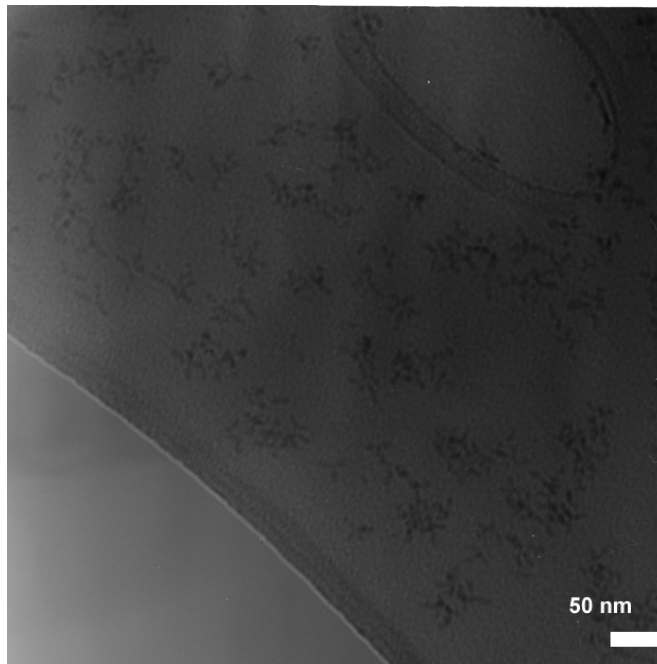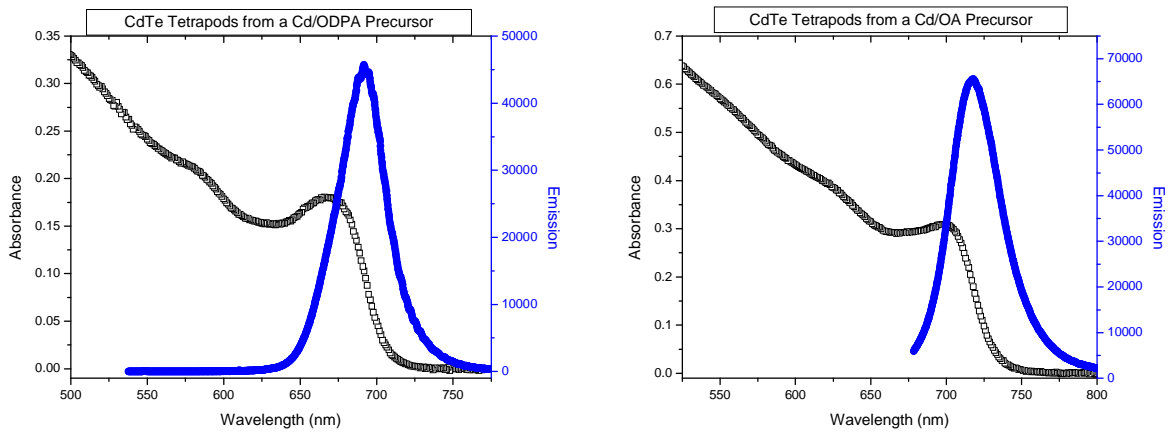
Figure 29: Absorption and Emission Spectra from CdTe Tetrapods Synthesized from a Cd/ODPA Precursor (Top Left) and a Cd/OA Precursor (Top Right) and the TEM Image of CdTe Tetrapods Grown from a Cd/OA Precursor, Corresponding to Spectra Presented in the Top Right.
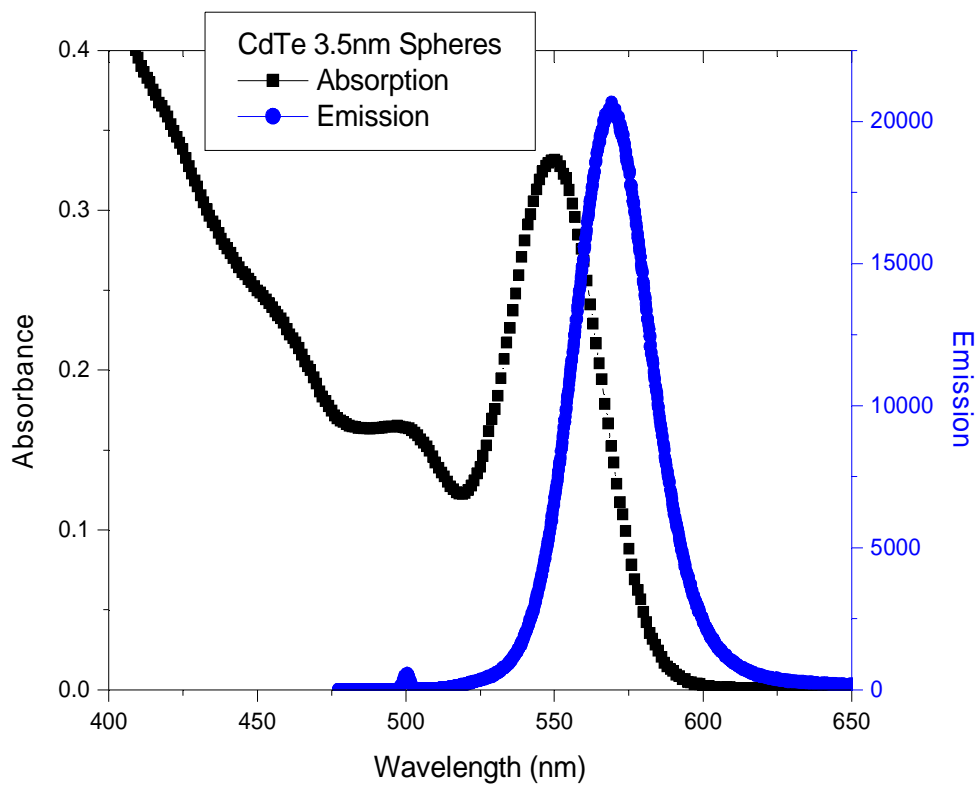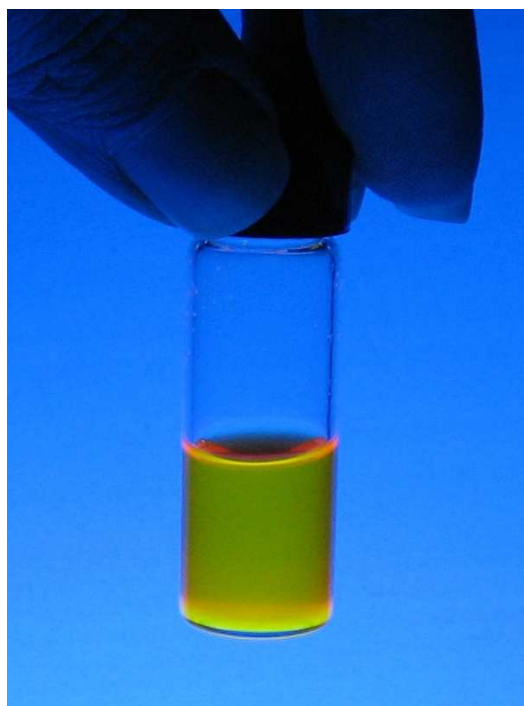
Figure 30: A Picture and Absorption and Emission Spectra of CdTe Spherical Cores.
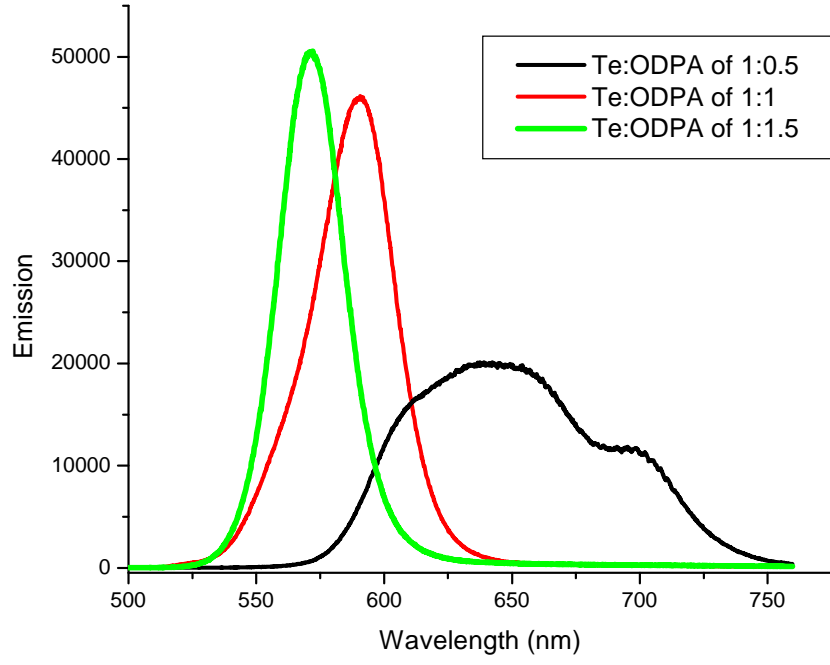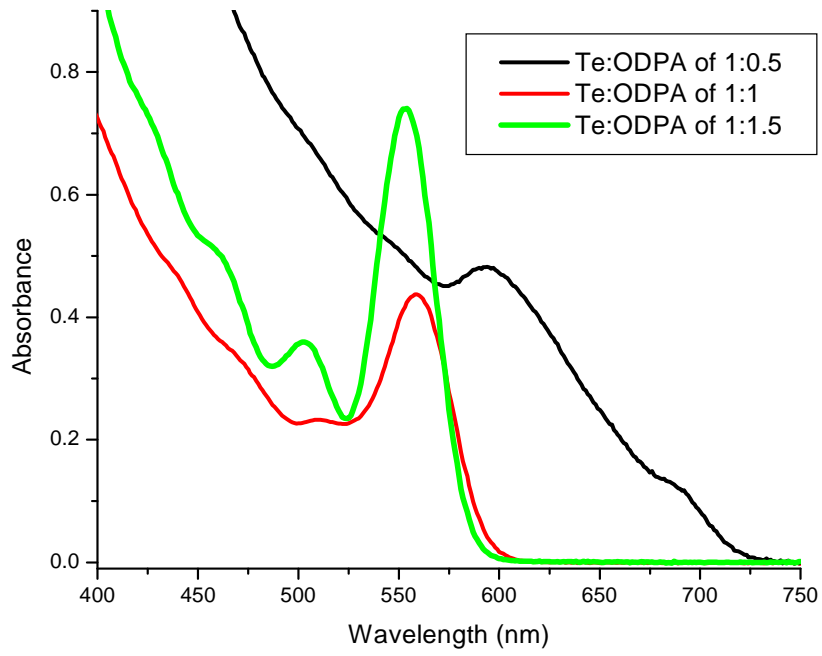
Figure 31: Absorption (Top) and Emission (Bottom) Spectra from CdTe Spherical Nanoparticle Syntheses Done by Varying the Te:ODPA Ratio. Emission data are obtained by exciting the samples with 500 nm light.
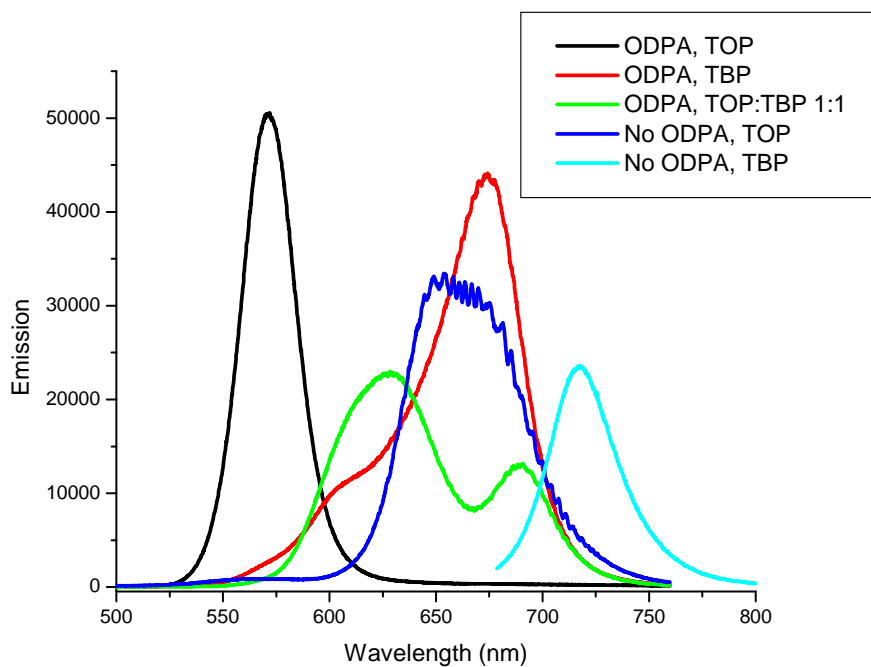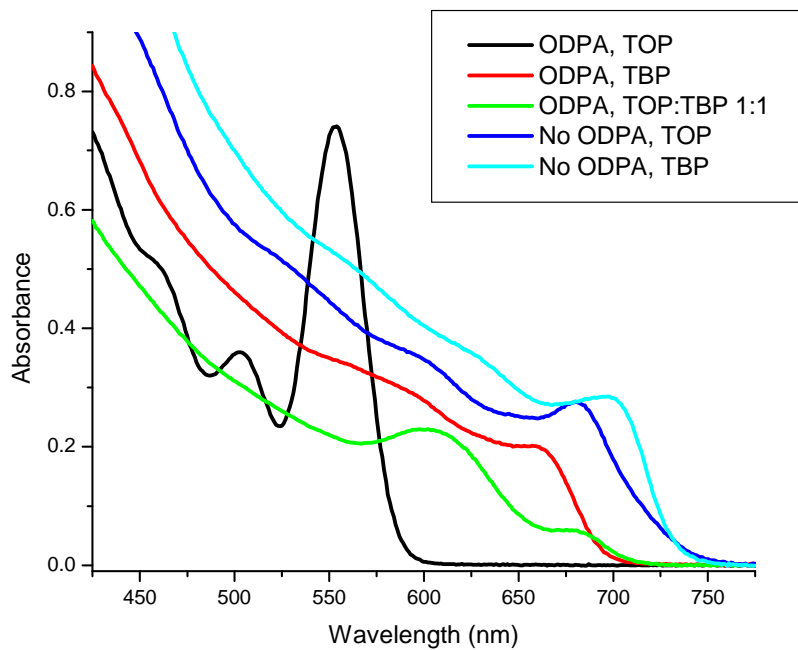
Figure 32: Absorption (Top) and Emission (Bottom) Spectra from CdTe Core Nanoparticle Syntheses Done by Using TOP Versus TBP. Emission data are obtained by exciting the samples with 500 nm light.
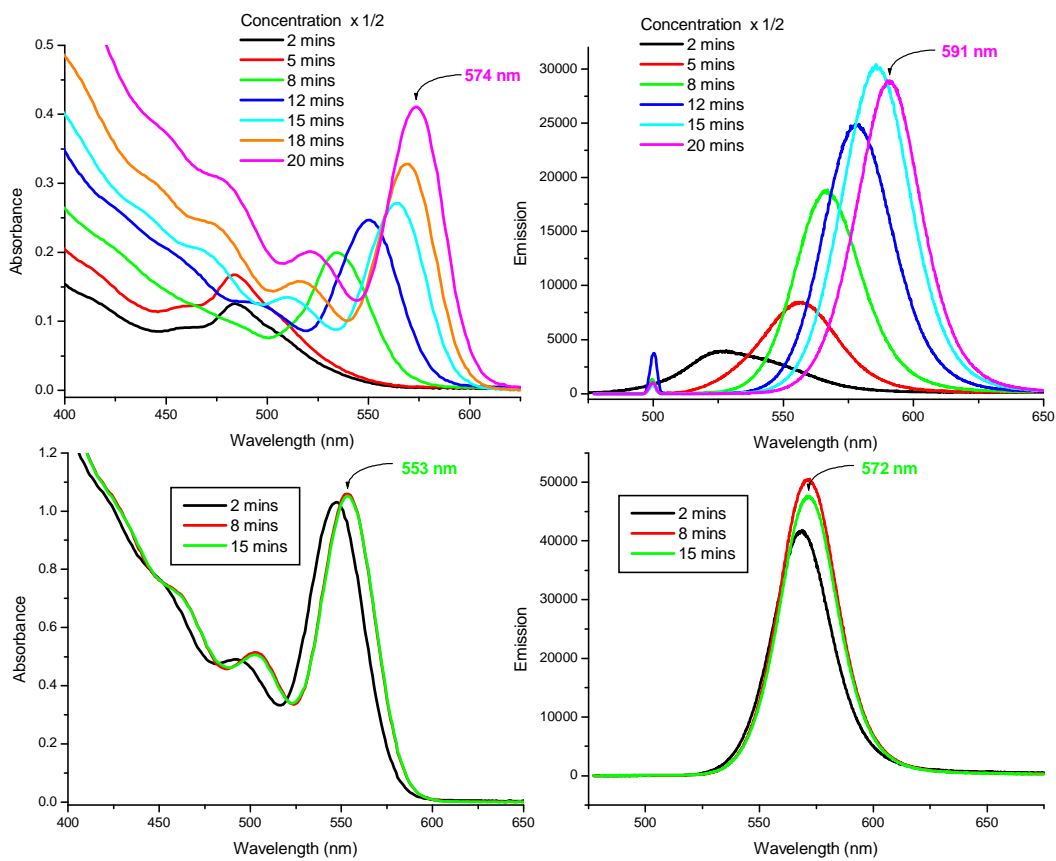
Figure 33: Concentration Effects on the Synthesis of CdTe Spherical Nanoparticles. Absorption and emission spectra from the control CdTe core synthesis (bottom) and a synthesis in which reaction volume was doubled (top) are shown. Emission data are obtained by exciting the samples with 500 nm light.
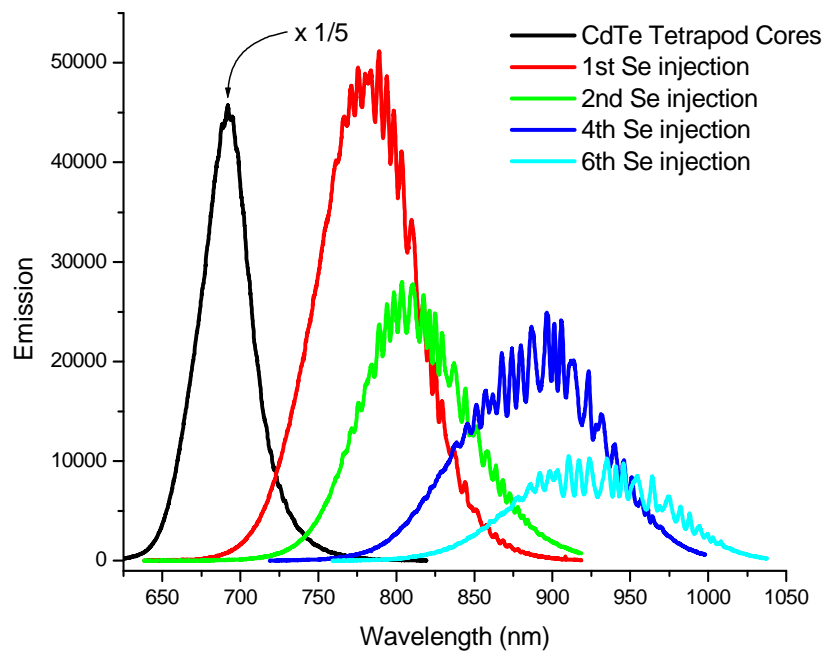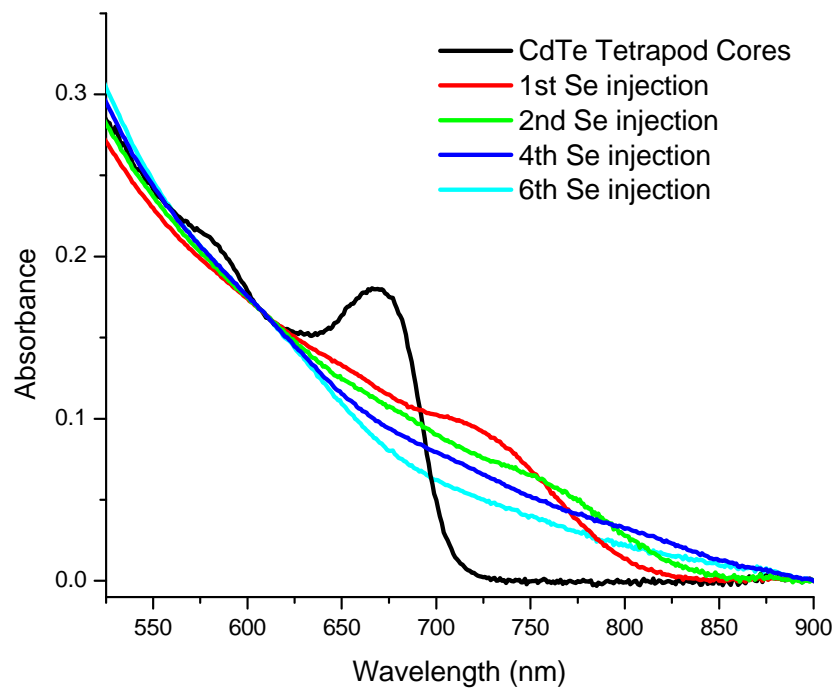
Figure 34: Absorption and Emission Spectra of Te/Se Tetrapod/Rods. The emission spectra are obtained by exciting the samples with 550 nm light.
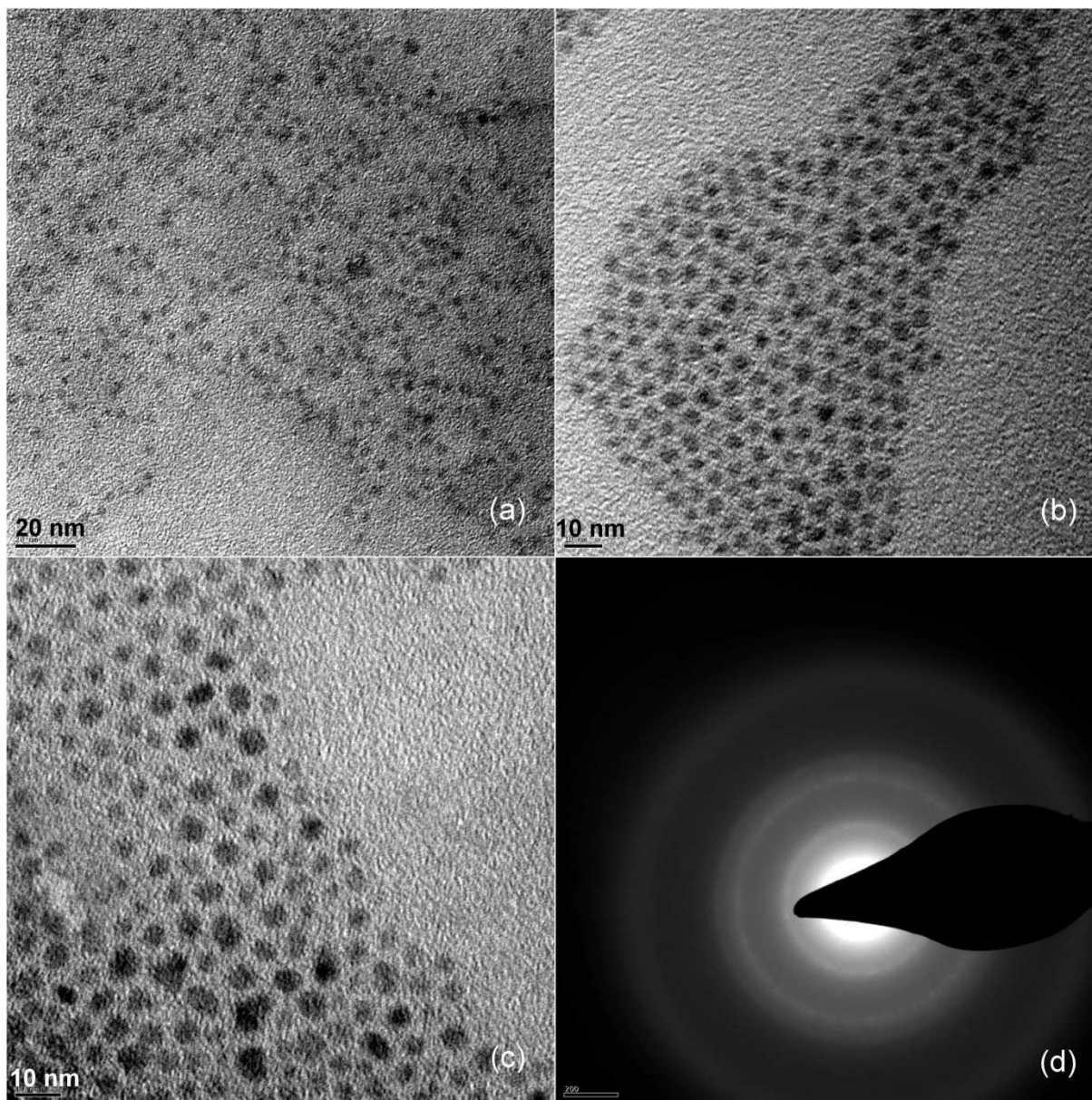
Figure 35: TEM Image of (a) 3.5 nm CdTe Cores, (b) 5.2 nm CdTe/CdSe Core/Shells with Five Injections of CdSe Shell, (c) 6.3 nm CdTe/CdSe Core/Shells with Eleven Injections of CdSe Shell, and (d) Electron Diffraction Pattern on Core/Shell Particles with Eleven CdSe Injections.
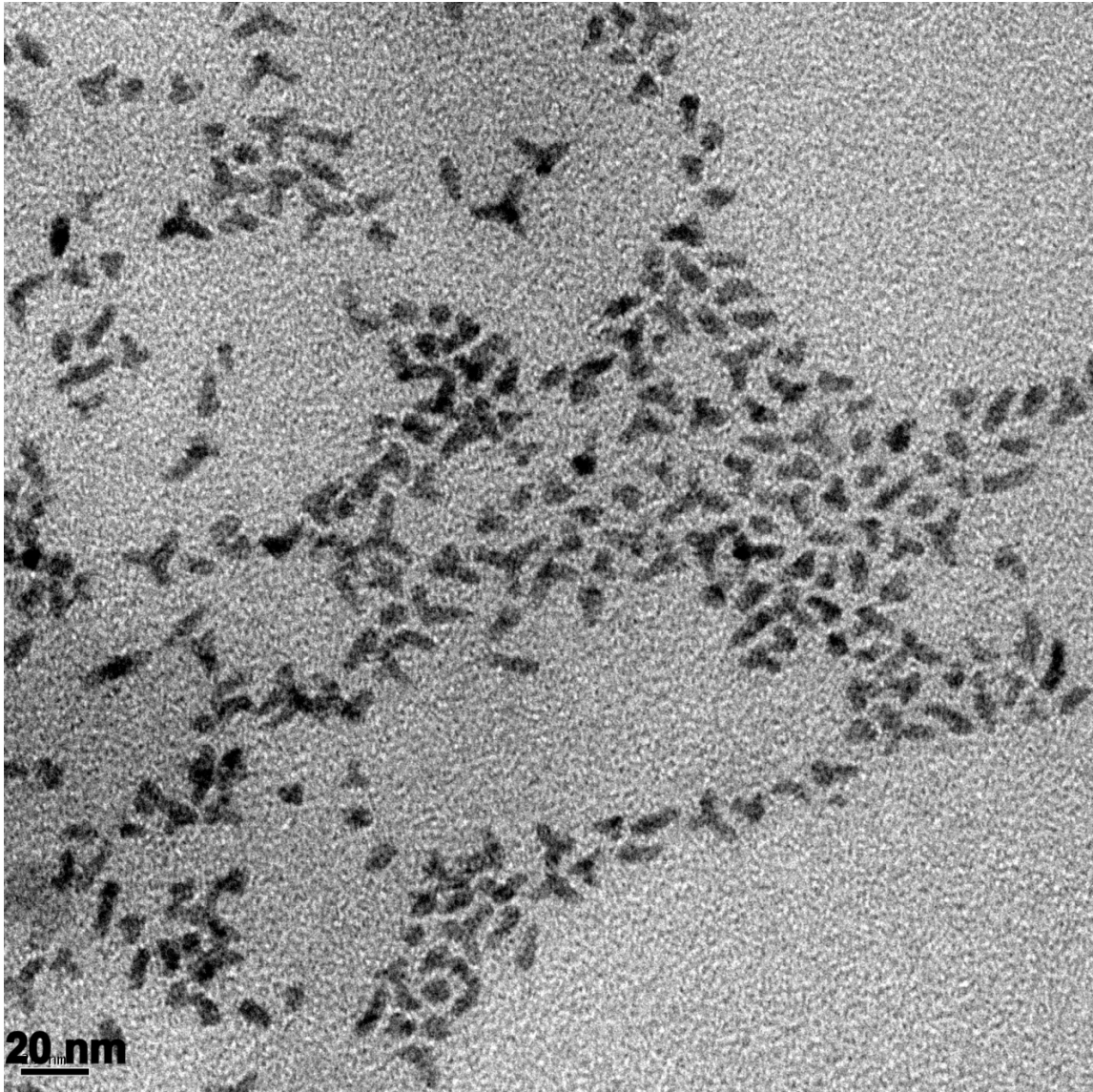
Figure 36: TEM Image of CdTe/CdSe Dot/Tetrapod Heterostructures with Twelve Injections of CdSe.
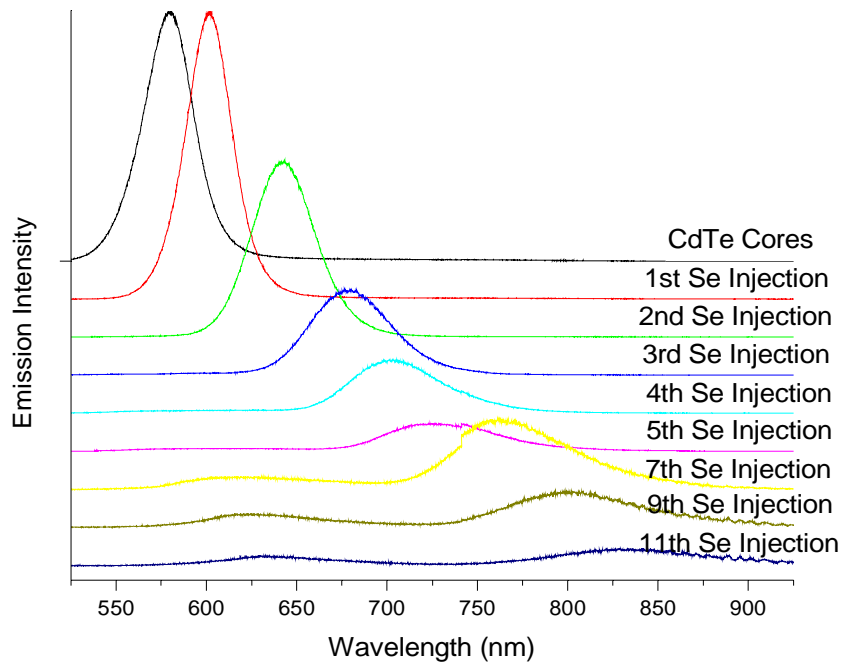
Figure 37: Progression of the Absorption and Photoluminescence Spectra from CdTe Cores to Eleven Injections of CdSe Spherical Shells. Spectra for the 7th, 9th, and 11th injections are multiplied by 5 to show the progression of the CT band clearly.
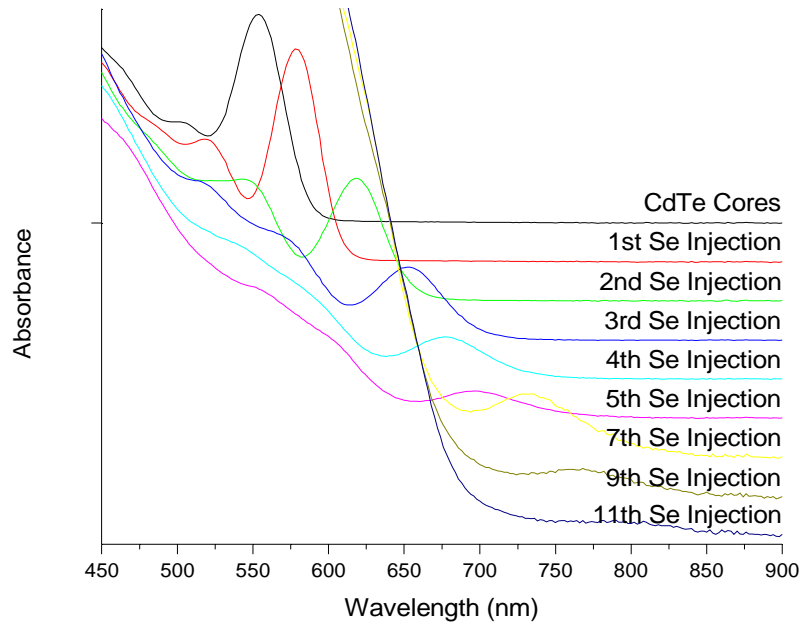
145
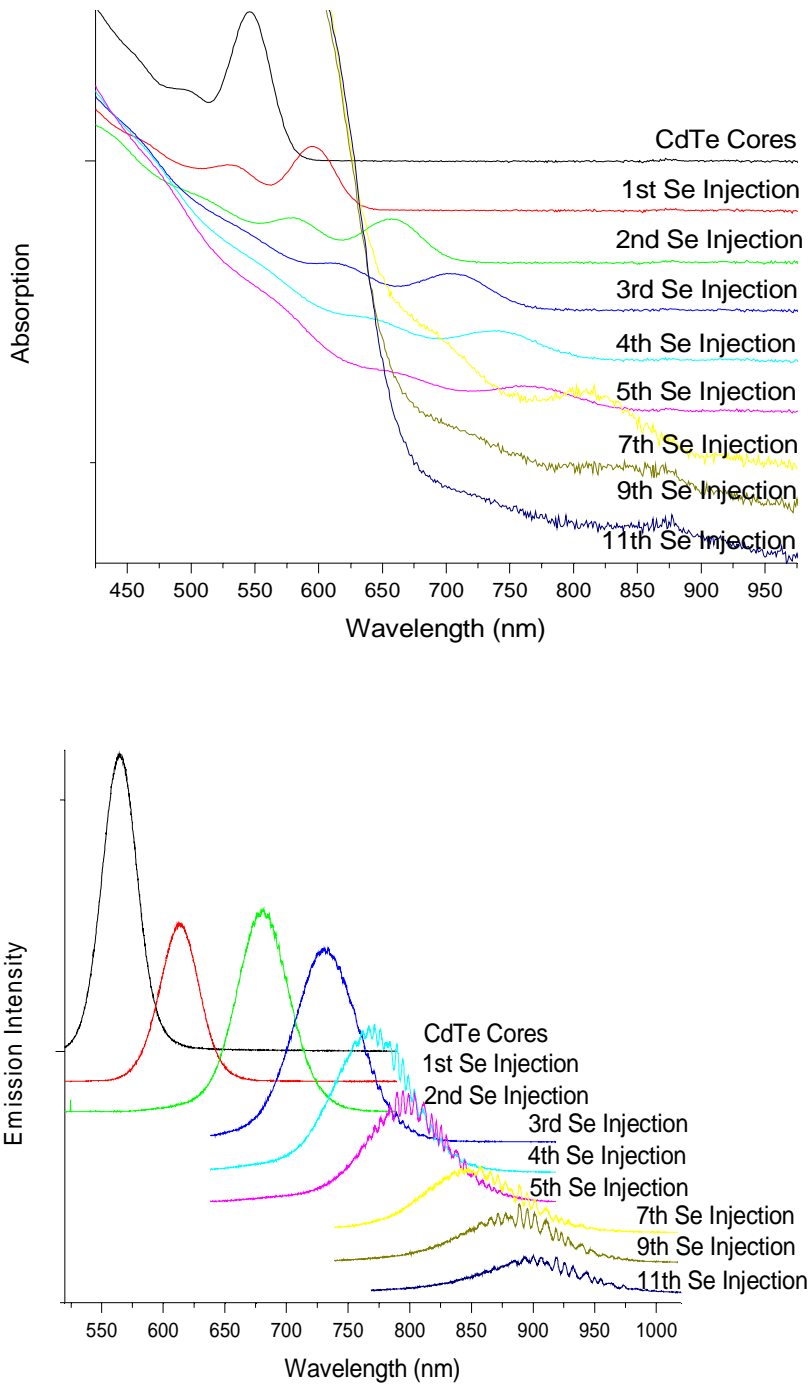
Figure 38: Progression of the Absorption and Emission Spectra from CdTe Cores to Eleven Injections of CdSe Tetrapod Shells. Absorption spectra for the 7th, 9th, and 11th injections are multiplied by 5 to show the progression of the CT band clearly.

146
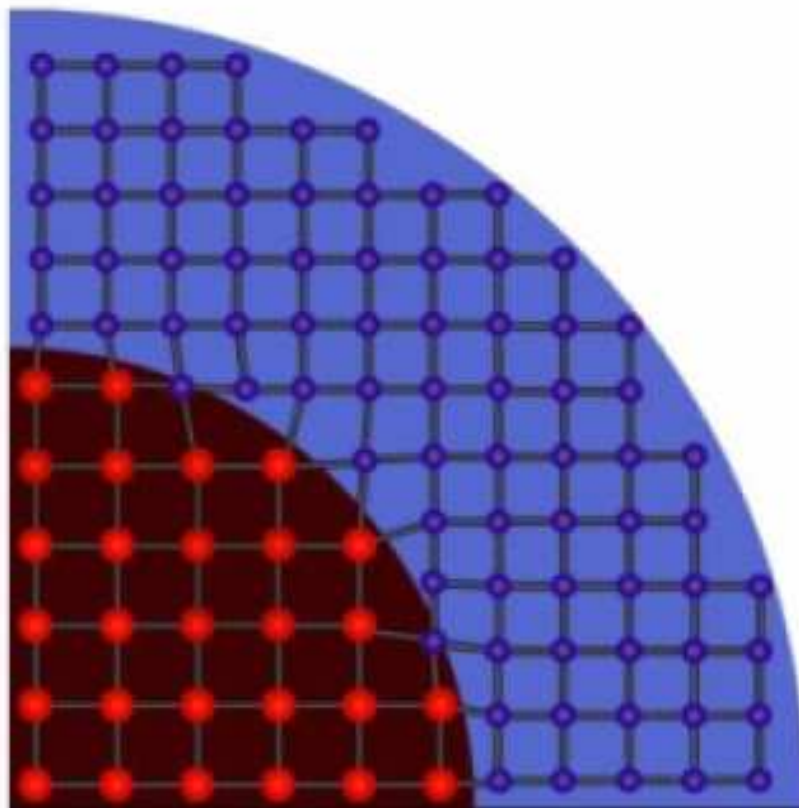
Figure 39: Schematic Showing the Strain Induced by a Smaller-lattice Shell (CdSe) onto a Larger-lattice Core (CdTe)*.

*Nature Nanotechnology **2009**, *4*, 56
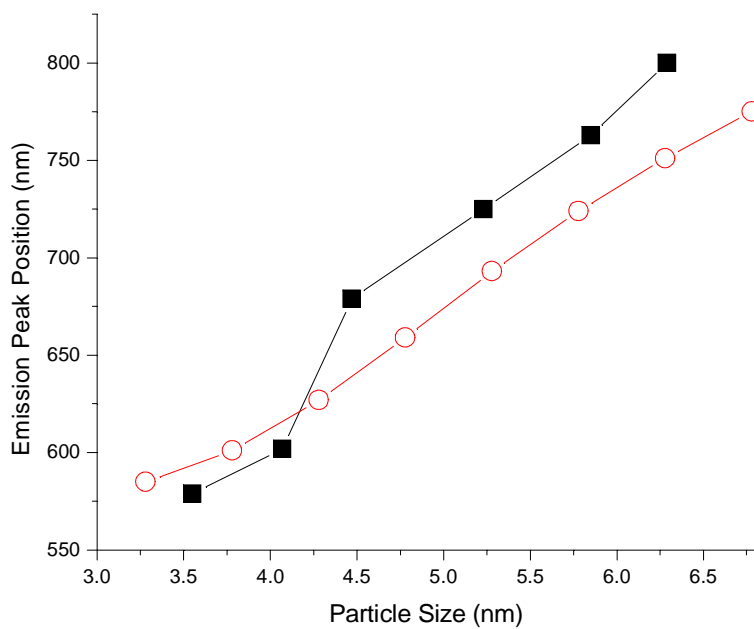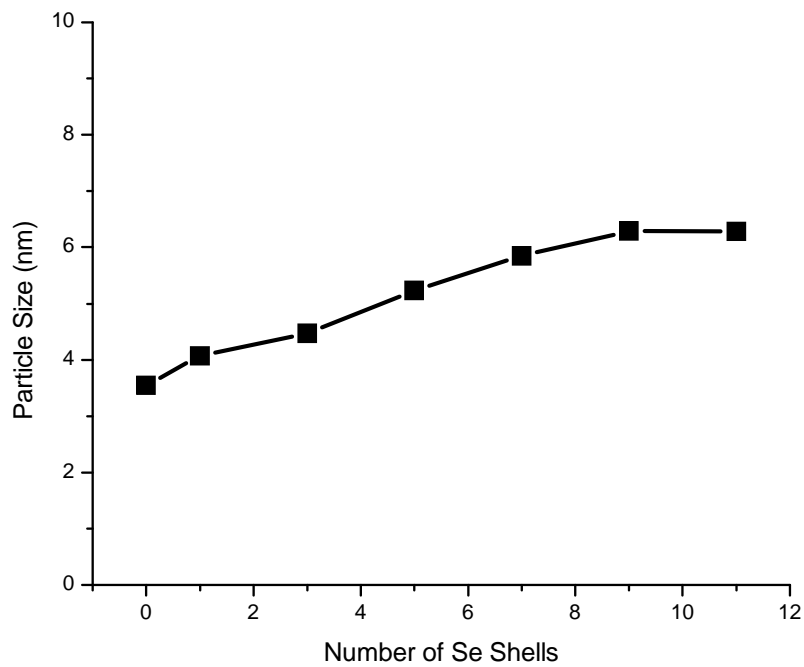
Figure 40: Top: Experimental Particle Size Determined from TEM Images. Bottom: Experimental Emission Peak Positions Measured from Luminescence Spectra (Solid Squares) Versus Calculated Emission Peak Positions (Hollow Circles).
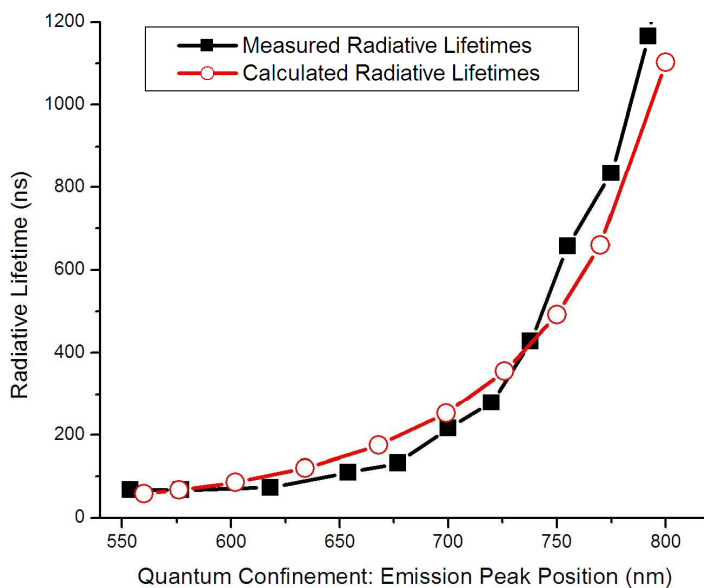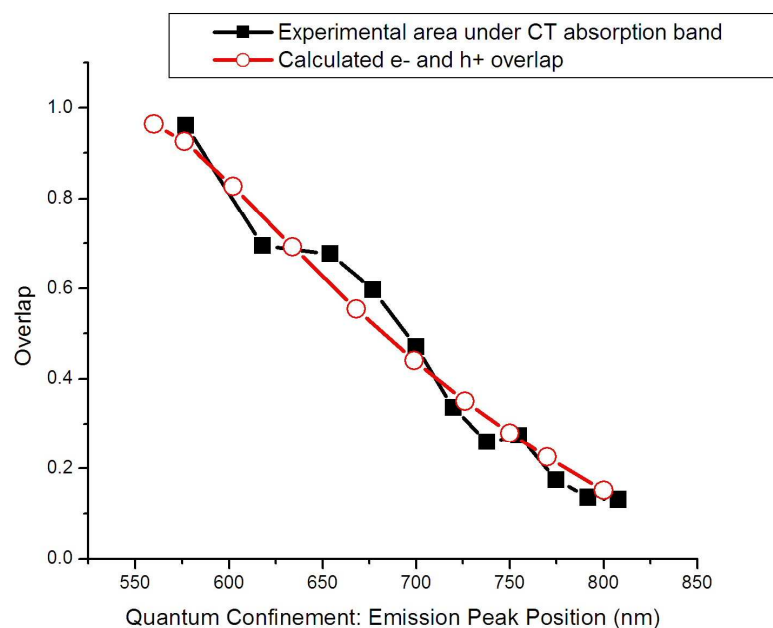
Figure 41: Top: Experimental Intensity of the CT Absorption Band Measured from Absorption Spectra (Solid Squares) Versus Calculated Overlap of Electron and Hole Wavefunctions (Hollow Circles). Bottom: Experimental Radiative Lifetimes Measured from Decay Curves and Quantum Yields (Solid Squares) Versus Calculated Radiative Lifetimes (Hollow Circles).
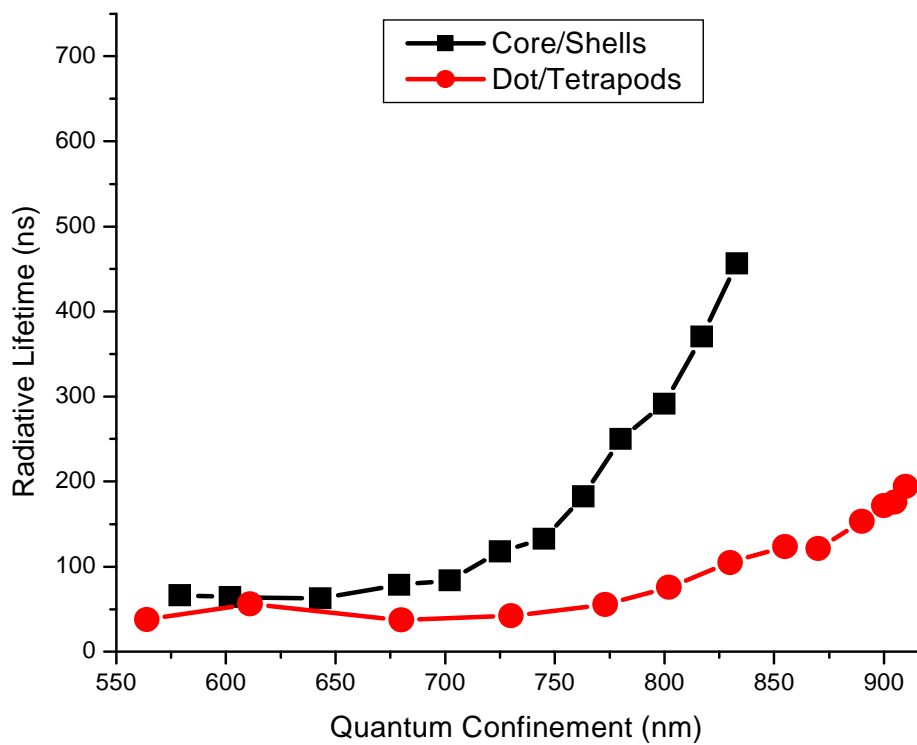
Figure 42: A Comparison between Radiative Lifetimes of CdTe/CdSe Core/Shells and Dot/Tetrapods.
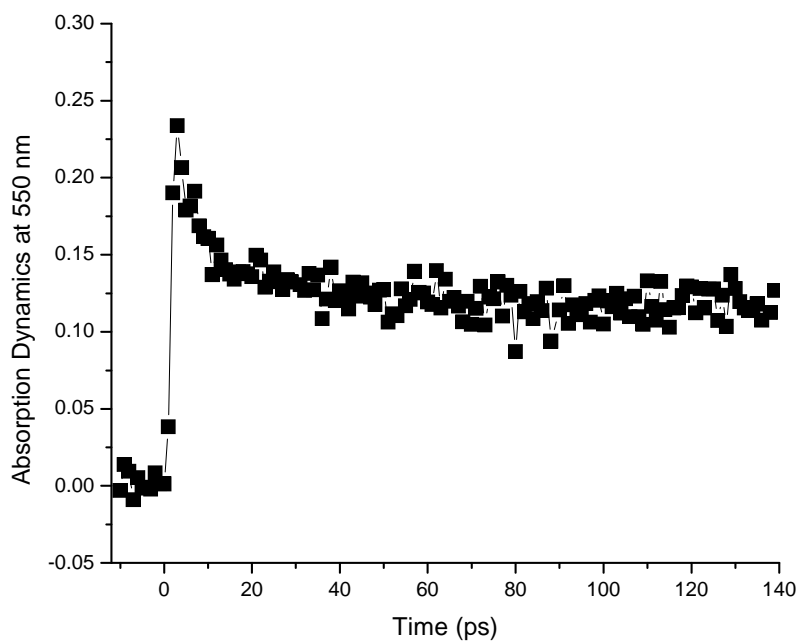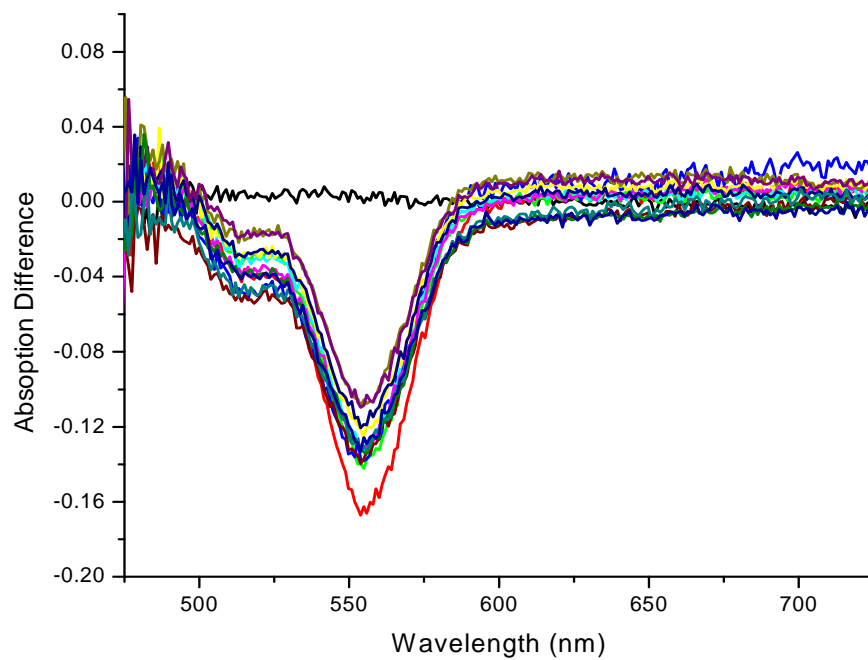
Figure 43: Top: Sample Raw Transient Absorption Spectra from CdTe Spherical Cores (curves are separated by approximately 15 ps). Bottom: Absorption Dynamics Derived from the Transient Absorption Data on Cores.
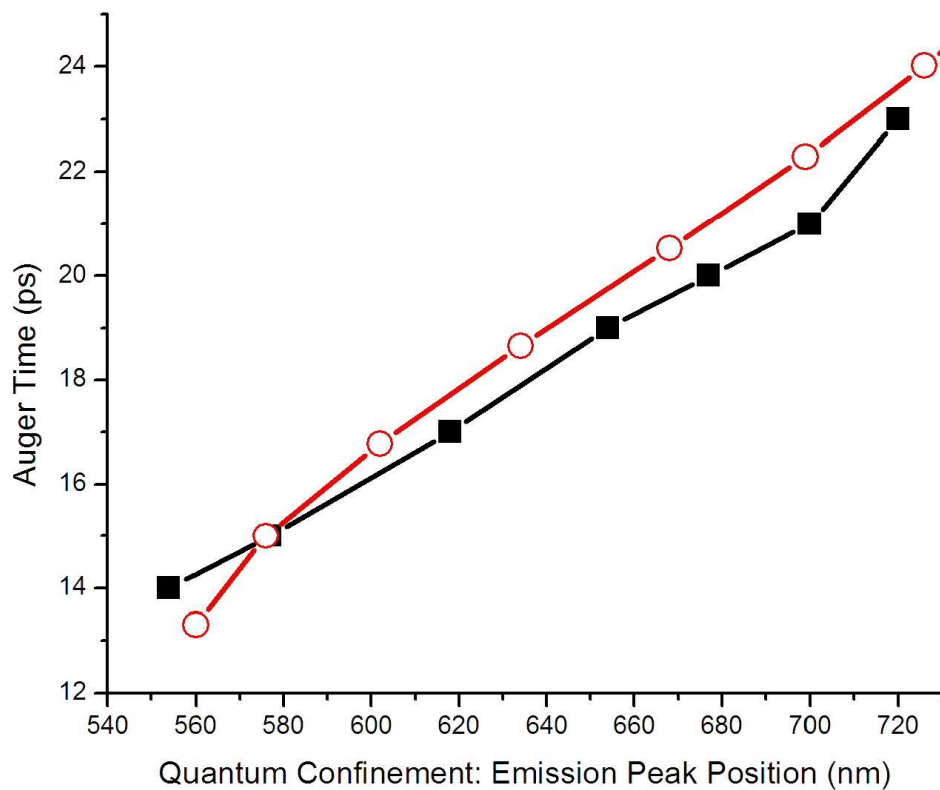
Figure 44: Experimental Auger Times Derived from Transient Absorption Dynamics (Solid Squares) Versus Calculated Interaction Energy Between the 1s Electron and the 1s Hole States (Hollow Circles).
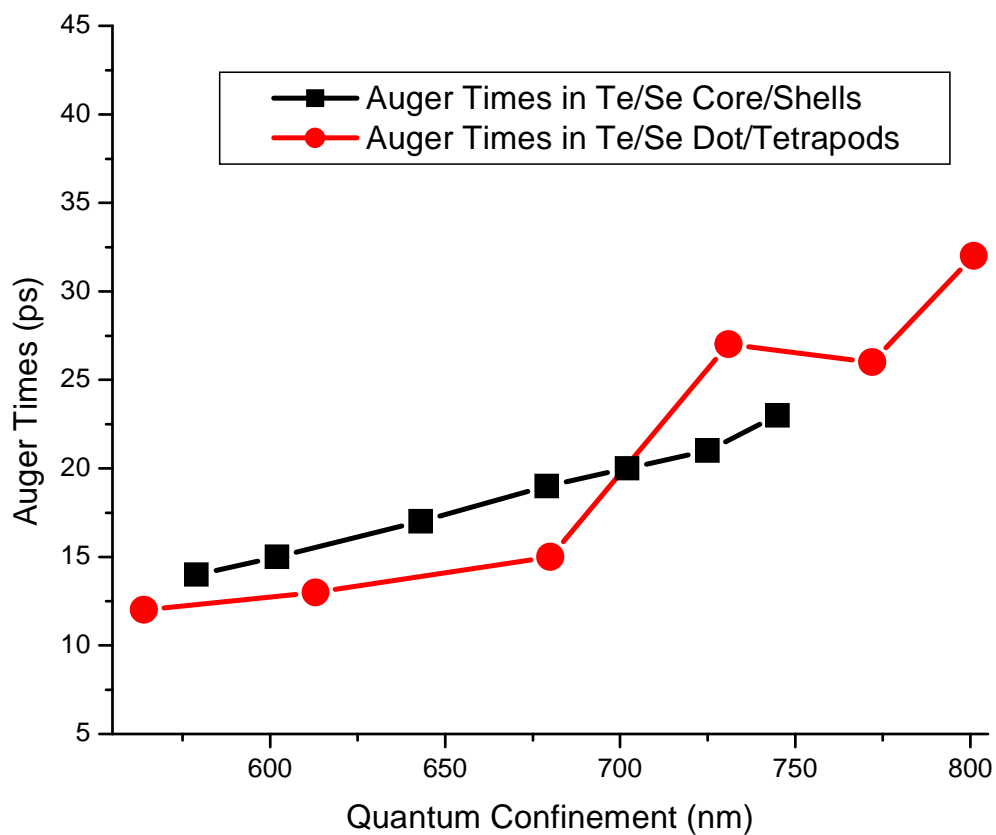
Figure 45: A Comparison Between the Experimental Auger Times in Te/Se Core/Shells (Black Squares) and Dot/Tetrapods (Red Circles)
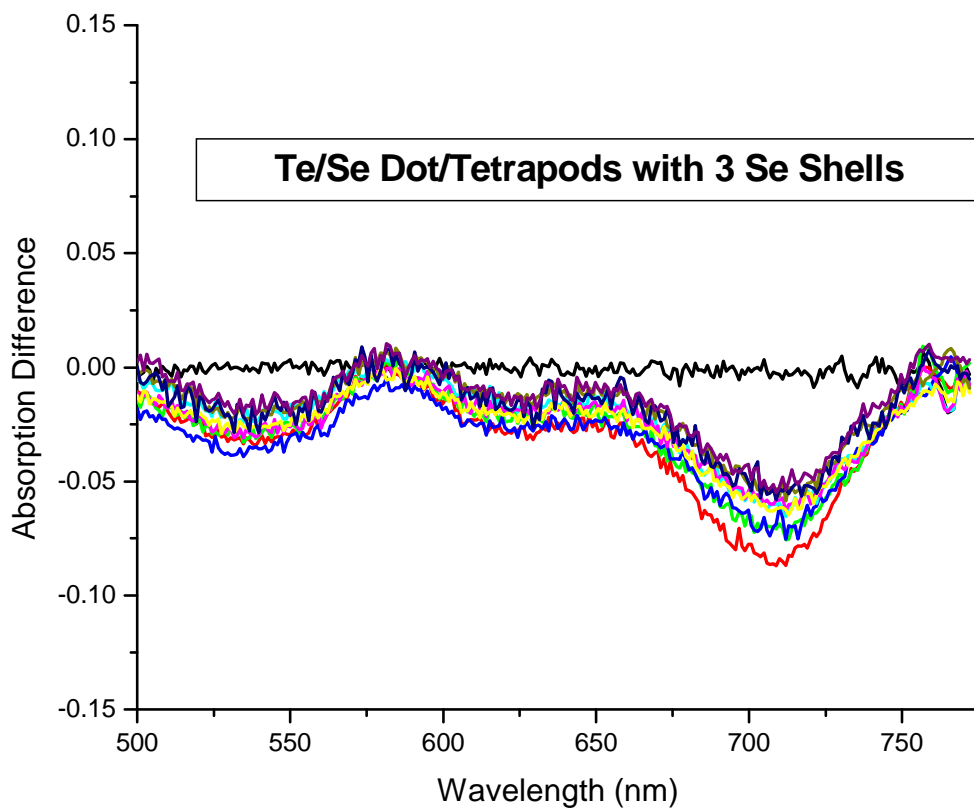
Figure 46: Raw Transient Absorption Spectra from CdTe/CdSe Dot/Tetrapods with Three Se Shells (curves are separated by about 15 ps).
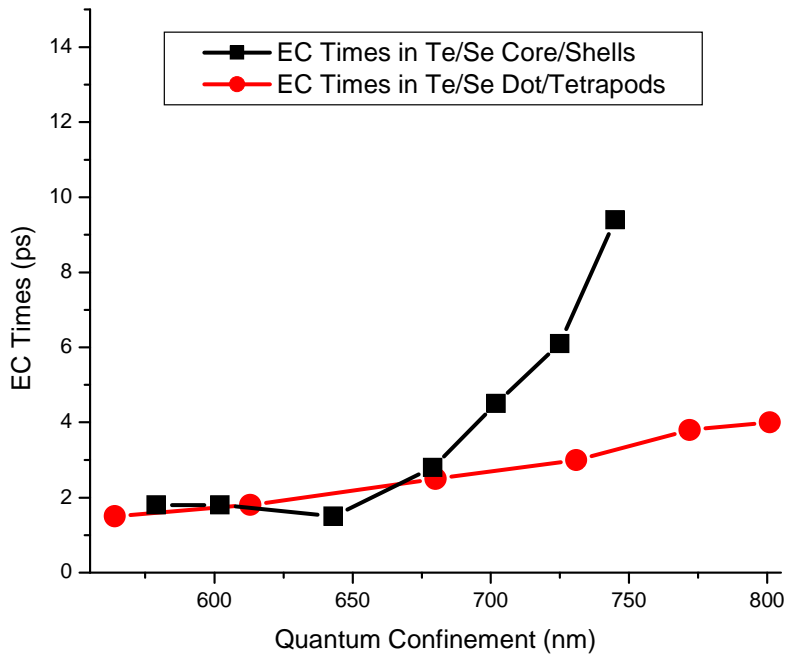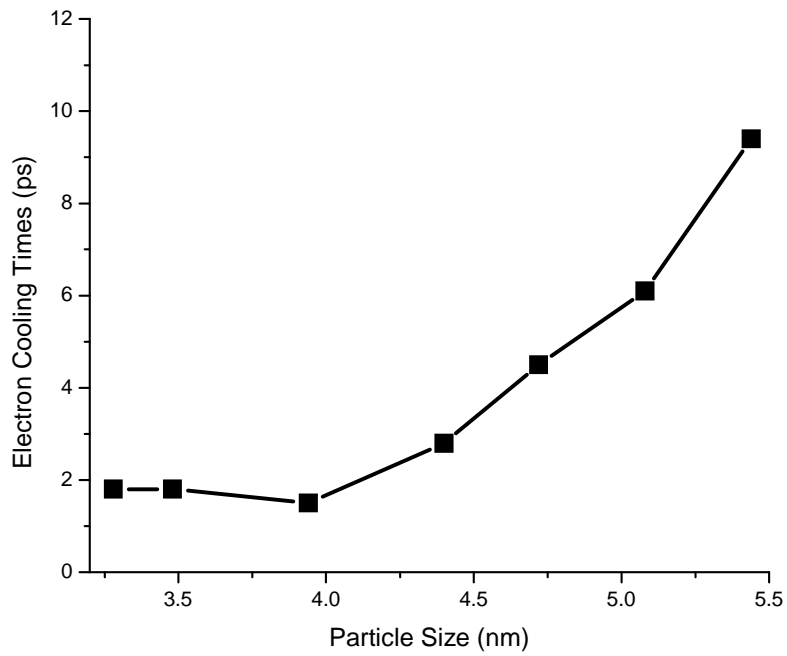
Figure 47: Top: Electron Cooling Times as a Function of Shell Thickness in Te/Se Core/Shell Heterostructures. Bottom: A Comparison between the Electron Cooling Times in Te/Se Core/Shells and Dot/Tetrapods. EC times are derived from the rise times of TA dynamics data.

Appendix A: Deconvolution Procedure for Correcting Fluorescence Kinetics

The 460 nm polarized fluorescence kinetics are obtained using an 80 MHz repetition rate light source. The analysis of these kinetics is complicated by the fact that when an excitation pulse arrives, fluorescence from the previous pulse has not completely decayed. The raw fluorescence data are presented in Figure . Fluorescence anisotropy results can be obtained by a procedure in which the parallel and perpendicular fluorescence components are corrected separately and subsequently used to calculate the anisotropy. In the time interval between successive pulses the observed parallel fluorescence component may be expressed as

$$I_{\parallel}(t) = f_{\parallel}(t) + C_{\parallel}\exp(-t/\tau_{\parallel}) \qquad \text{Equation A1}$$

with an analogous expression for the perpendicular component. The decay time $\tau_{\parallel}$ is obtained by fitting the last part of the decay, prior to the arrival of the next pulse. The function $f_{\parallel}(t)$ reflects the more rapidly decaying fluorescence components. It is important to note that these components decay rapidly. As a result, we make the approximation that $f_{\parallel}(t+t_p)\ ;\ 0$, where t_p is the time between pulses, 12.26 ns. In the absence of multiple pulses, the parallel fluorescence intensity would be given by

$$I'_{\parallel}(t) = f_{\parallel}(t) + C'_{\parallel}\exp(-t/\tau_{\parallel}) \qquad \text{Equation A2}$$

This and the analogous perpendicular quantity may be used to calculate the appropriate fluorescence anisotropies, so $I'_{\parallel}(t)$ in equation A2 is what we want to extract from the results, equation S1. These quantities are related by

$$I_{\parallel}(t) = I'_{\parallel}(t) + I'_{\parallel}(t+t_p) + I'_{\parallel}(t+2t_p) + \dots\ . \qquad \text{Equation A3}$$

Using the approximation $f_{\parallel}(t+t_p); \; 0$, equation A3 may be written as

$$I_{\parallel}(t) = f_{\parallel}(t) + C'_{\parallel} \exp(-t/\tau_{\parallel})\{1 + \exp(-t_p/\tau_{\parallel}) + \exp(-2t_p/\tau_{\parallel}) + ...\} \,.$$

The constant $C_{//}$ may therefore be expressed as

$$C_{\parallel} = C'_{\parallel}\{1 + \exp(-t_p/\tau_{\parallel}) + \exp(-2t_p/\tau_{\parallel}) + ...\} \quad \text{or} \quad C'_{\parallel} = C_{\parallel}\{1 - \exp(-t_p/\tau_{\parallel})\}\,.$$ This value of $C'_{\parallel}$

along with $f_{//}(t)$ and $\tau_{//}$ obtained from equation A1 may be used to evaluate equation A2. This analysis has a very simple interpretation: the parallel and perpendicular intensities that would be obtained in the absence of the high laser repetition rate are obtained by simply subtracting off the exponentially-decaying fluorescence from the previous pulses. This is illustrated in Figure . The corrected time-dependent parallel and perpendicular intensities obtained from equation A2 are used to calculate the anisotropy results presented in Figure 14.
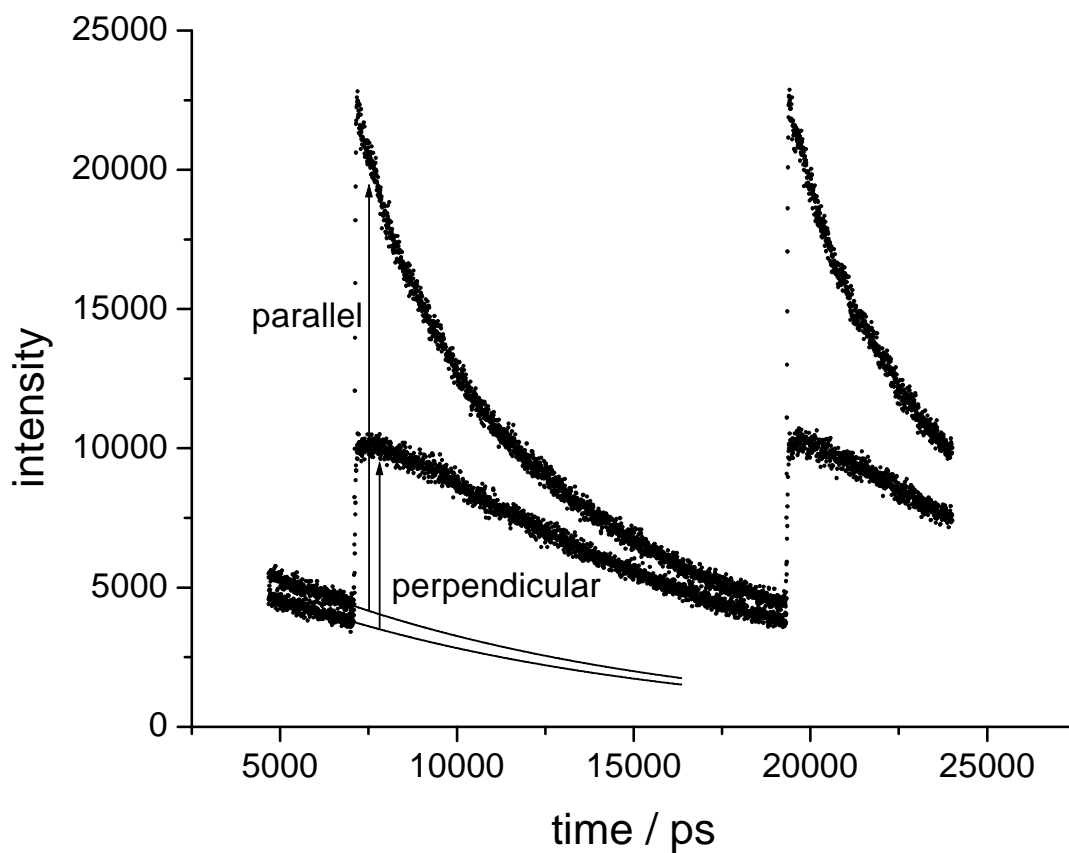
Figure A1: Polarized Fluorescence Results Obtained form Dodecanal-ligated Particles Following 460 nm Excitation at 80 MHz. Also shown are exponentially-decaying curves obtained by fitting the long-time decay of each polarization.

Appendix B: Selected Synthesis Protocols

A. Synthesis of Se/Te Rod/Rod Heterostructures:

- **CdSe rod cores**

  - Cd/ODPA precursor: 205 mg of CdO (1.6 mmol) + 1.07 g of ODPA (3.2 mmol) + 2.90 g of TOPO

  - Se precursor: 63.2 mg of Se (0.8 mmol) + 267 mg of ODPA (0.8 mmol) dissolved in 2 mL of TOP

For all syntheses presented, ODPA and TOPO are recrystallized twice to ensure purity. TOP is carefully vacuum distilled as explained in the beginning of Chapter Two: Synthesis of Part I.

The Cd/ODPA precursors are always heated to 320 to 340 ^{o}C until an optically clear solution is obtained. Te and Se do not dissolve easily in low amounts of TOP at room temperature. To facilitate the dissolution process, the Se precursor is heated to 80 to 100 ^{o}C for about twenty minutes until a clear colorless solution is obtained. The Cd/ODPA precursor is allowed to slightly cool to 300 ^{o}C before the Se precursor is injected. Upon injection, the temperature decreases to 280 ^{o}C and is maintained there for the duration of reaction time. The reaction is terminated about 4 to 6 minutes after Se injection depending on what size rods are desired.

- **CdTe rod shells**

  - Cd/ODPA precursor: 102 mg of CdO (0.8 mmol) + 0.669g of ODPA (2 mmol) + 1.45g of TOPO

o   Te Precursor: 204 mg of Te (1.6 mmol)

dissolved in 4mL TOP

The Te precursor is heated to 80 to 100 ^{o}C for about twenty minutes until a clear lime-colored solution is obtained. Since the Cd/ODPA is solid at room temperature, the previously prepared CdSe cores are added to the Cd precursor and heated to 120 ^{o}C until liquid. One fourth (or 1 mL) of the Te precursor is injected at 120 ^{o}C and the reaction is brought to temperature (260 ^{o}C). The reaction is run for twenty minutes before the next 1 mL injection of the Te precursor. This process is repeated for two more injections. In order to monitor the synthesis progress, sample aliquots are taken right before each Te injection.

B. Synthesis of CdTe Tetrapods from a Cd/ODPA Precursor:

o   Cd/ODPA precursor: 269 mg of CdO (2.1 mmol) + 1.172 g of ODPA (3.5 mmol) + 2.90 g of TOPO

o   Te precursor: 38.3 mg of Te (0.3 mmol)

dissolved in 1mL TOP

Cd/ODPA precursor is heated to 325 ^{o}C for 20 minutes until optically clear. The Te precursor is heated to 80 to 100 ^{o}C for about twenty minutes until a clear lime-colored solution is obtained. The entire Te precursor is injected fast into the Cd precursor at 325 ^{o}C. Upon injection, the temperature is decreased to 305 ^{o}C and maintained there for three minutes before quenching the reaction.

C. Synthesis of CdTe Tetrapods from a Cd/OA Precursor:

- Cd/OA precursor: 0.2 mmol CdO (25.7 mg) + 0.8 mmol OA (0.252 mL) + 3 mL ODE

- Te precursor: 0.1 mmol Te (12.8 mg) + 0.143 mL TBP + 1 mL ODE

Octadecene is vacuum distilled to ensure purity. Oleic acid (OA) and TBP are used as received from commercial vendors. The Te precursor is heated to 80 to 100 ^{o}C for about twenty minutes until a clear lime-colored solution is obtained. The Cd/OA precursor is heated to 280 ^{o}C (it turns into a clear colorless solution at around 230 ^{o}C). The entire Te precursor is injected at 280 ^{o}C. Once the temperature decreases to 260 ^{o}C, the reaction is kept at this temperature for three minutes before shut down.

D. Synthesis of Te/Se Tetrapod/Rod Heterostructures:

- **CdSe tetrapod cores**

  - Cd/ODPA precursor: 269 mg of CdO (2.1 mmol) + 1.172 g of ODPA (3.5 mmol) + 2.90 g of TOPO

  - Te precursor: 38.3 mg of Te (0.3 mmol) dissolved in 1mL TOP

Cd/ODPA precursor is heated to 325 ^{o}C for 20 minutes until optically clear. The Te precursor is heated to 80 to 100 ^{o}C for about twenty minutes until a clear lime-colored solution is obtained. The entire Te precursor is injected fast into the Cd precursor at 325 ^{o}C. Upon injection, the temperature is decreased to 305 ^{o}C and maintained there for three minutes before injecting the Se precursor.

- **CdSe rod shells**

161

o   Se Precursor: 126.3 mg of Se (1.6mmol)

dissolved in 2.4 mL TOP

The Se precursor is heated at 80 to 100 ^{o}C until a clear colorless solution is obtained. The Se precursor is injected in six equal injections (0.267 mmol per injection) with three minutes in between each injection. Injections are done slow (20 – 30 seconds). The first injection is done at 305 ^{o}C. After that, the reaction is maintained at 260 – 265 ^{o}C for the duration of CdSe growth. To monitor the extent of shell growth, sample aliquots are syringed out of the reaction immediately before each Se injection.

E. Synthesis of Te/Se Tetrapod/Uniform Shell Heterostructures:

- **CdSe tetrapod cores**

  o Cd/OA precursor: 0.2 mmol CdO (25.7 mg) + 0.8 mmol OA (0.252 mL) + 3 mL ODE

  o Te precursor: 0.1 mmol Te (12.8 mg) + 0.143 mL TBP + 1 mL ODE

Octadecene is vacuum distilled to ensure purity. Oleic acid (OA) and TBP are used as received from commercial vendors. The Te precursor is heated to 80 to 100 ^{o}C for about twenty minutes until a clear lime-colored solution is obtained. The Cd/OA precursor is heated to 280 ^{o}C (it turns into a clear colorless solution at around 230 ^{o}C). The entire Te precursor is injected at 280 ^{o}C. Once the temperature decreases to 260 ^{o}C, the reaction is kept at this temperature for three minutes before shut down.

- **CdSe rod shells**

  o Cd/ODPA precursor: 128.4 mg of CdO (1 mmol) + 0.644 g of ODPA (1.93 mmol) + 3.2 g of TOPO

- o   Se Precursor: 47.4 mg of Se (0.6mmol) dissolved in 1 mL TOP

The Se precursor is heated at 80 to 100 ^{o}C until a clear colorless solution is obtained. Cd/ODPA precursor is heated at 320 ^{o}C for ten minutes and then, cooled down to 170 ^{o}C. Previously prepared Te tetrapod cores are added to the Cd/ODPA precursor. The temperature is lowered to 130 ^{o}C due to injection. At this point, the Se precursor in injected, and temperature is quickly increased to 250 ^{o}C. The reaction is maintained at 250 ^{o}C for 20 minutes before shut down.

Appendix C: FORTRAN Code

```
Program FourierSPH
!Considers band bowing effects on valence band
!Does not consider valence band degeneracy
DIMENSION
Z0(300),Z1(30),Z2(30),zp(30),V(50,50),T(50,50),T1(50,50),AN0(50),AN1(50),A0(50),ACN(50
),C0(2000),C1(2000)
DIMENSION
CBAND(2000),VBAND(2000),VELEC(2000),VHOLE(2000),AHMASS(2000),AEMASS(2000
)
DIMENSION FE(3000,10),FE1(3000,10),
FH(3000,10),EE(150),EE1(150),EH(150),FELEC(2000),FHOLE(2000),RS(2000)
DIMENSION EVAL(50),EVEC(50,50)
DIMENSION FKE(2000), FKE1(2000),FKE2(2000),FKE3(2000),
FKET(2000),FKH(2000),AMIX(10),AMIX2(10)
LDA=50;LDEVEC=50
PI=3.1415926535

!core radius
R1=1.64
!shell thickness
TSHELL=1.5

R2=R1+TSHELL
R3=R2+2.0
X1=R1/R2

!valence and conduction band offsets, vacuum level and dielctric constant.
VE=-2400.
VH=4600.
CORX=12100.
VAC=24000.
DCONST= 8.
! pos value of VE or VH localizes the wavefunction on the inside of the particle
!Diffusion parameter
D=.3

NTCOMP=25
!core and shell electron effective masses
SCALE=1.0
CMASSE=SCALE*.10
SMASSE=SCALE*.11
!core and shell hole effective masses
CMASSH=SCALE*.40
```

SMASSH=SCALE*0.44

!calculate compression shifts

DBAR=TSHELL/R1
!lattice mismatch
AMATCH=.076
!strain tensor from eqn A4
EPP=AMATCH*DBAR*(0.666*(3.+3.*DBAR+DBAR**2)/(1+DBAR)**3)*0.55
! 704 wavenumbers/GPa, bulk modulus = 53 GPa
PSHIFT=704.*EPP*3.0*53.0
!PSHIFT=0.
!Raman winewidth
GAMMA=8.

NUM=500
NUM2=NUM*R3/R2
WRITE (*,*) NUM, NUM2
DX=1./NUM
DX2=1./NUM2
DR=DX2*R3
NT=25
NS=5
!NT is the number fourier terms, NS is the number of states calculated
CONST=307.0
EHCONST=11610.
! const is simply h-bar**2/(2*electron mass) in in units of wavenumbers and nanometers
! ehconst is (electron charge)^2/(4 pi epsilon-zero) in units of wavenumbers and nanometers

! zeros of j1
z1(1)= 4.49341
z1(2)= 7.72525
z1(3)= 10.90412
z1(4)= 14.06619
z1(5)= 17.22076
z1(6)= 20.3713
z1(7)= 23.51945
z1(8)= 26.66605
z1(9)= 29.8116
z1(10)=   32.95639

do j=8, 28
z1(j) = 1.36592 + 3.17771*j - 0.00218*j**2 + .000040105*j**3
end do
!   y=1.36592 + 3.17771 X - 0.00218 X^2 + .000040105 X^3

! calculate normalization factors for the spherical bessel functions

```
DO N=1,NT
DO J=1,NUM2
X=J*DX2
R=X*R3
AN0(N)=AN0(N)+(SIN(N*PI*X)/(N*PI*X))**2*R**2*DR
AN1(N)=AN1(N)+SB1(X*Z1(N))**2*R**2*DR
END DO
END DO
DO N=1,NT
AN0(N)=1.0/SQRT(AN0(N))
AN1(N)=1.0/SQRT(AN1(N))
END DO


!-------------------------------------------------------------------------------
! set up initial composition step function
X=0
DO I=1, NUM
X=X+DX
IF(X > X1) THEN
C0(I)=0.0
ELSE
C0(I)=1.0
ENDIF
END DO
X=0.
DO I=1,NUM
X=X+DX
AVE=AVE + X**2*DX*C0(I)
TOT=TOT + X**2*DX
END DO
AVE=AVE/TOT
!average composition

DO N=1,NTCOMP
NM1=N-1
X=0.0
DO I=1,NUM
X=X+DX
A0(N)=A0(N)+X**2*DX*C0(I)*SB0(X*Z1(N))
ACN(N)=ACN(N)+X**2*DX*(SB0(X*Z1(N)))**2
END DO
A0(N)=(A0(N)/ACN(N))
END DO
```

```
DO N=1,NTCOMP
X=0.
DO I=1,NUM
X=X+DX
C1(I)=C1(I)+A0(N)*SB0(X*Z1(N))*EXP(-D*(Z1(N)/R2)**2)
END DO
END DO


AVE0=0.
AVE1=0.
AVET=0.
DO I=1,NUM
X=I*DX
AVE1=AVE1 + X**2*DX*C1(I)
AVE0=AVE0 + X**2*DX*C0(I)
AVET=AVET + X**2*DX
END DO


AVE=(AVE0-AVE1)/AVET
DO I=1,NUM
C1(I)=C1(I)+AVE
END DO


! calculate the position dependent effective masses
DO I=1, NUM2
IF (I <= NUM) THEN
AEMASS(I)=CMASSE + (1.0-C1(I))*(SMASSE-CMASSE)
AHMASS(I)=CMASSH + (1.0-C1(I))*(SMASSH-CMASSH)
ELSE
AEMASS(I)=1.
AHMASS(I)=1.
END IF
END DO
!---------------------------------------------------------------------------
EELEC=CONST/R3**2
EHOLE=CONST/R3**2

WRITE (*,*) "core radius", R1
WRITE (*,*) "shell thickness", TSHELL
WRITE (*,*) "diffusion parameter", D
WRITE (*,*) "conduction and valence band offsets and compression shift",VE,VH,PSHIFT
WRITE (*,*)
! Eg(x)=(1-x)Eg(CdX)+xEg(CdY) + b x(1-x)
! b=1.84 eV for CdSe/CdTe
bow=0.75*8065.
```

```fortran
! calculate the potentials
corx=corx+pshift*(c1(1)-c1(num-1))
DO I=1,NUM2
IF(I <= NUM)  THEN
VELEC(I)=-C1(I)*VE+PSHIFT*(C1(I)-C1(NUM-1))
ELSE
VELEC(I)=VAC
END IF
END DO


DO I=1,NUM2
IF(I <= NUM)  THEN
!VHOLE(I)=(1.0-C1(I))*VH
VHOLE(I)=(1.0-C1(I))*VH - bow*C1(I)*(1.0-C1(I))
!x=C1= composition fraction of the core
ELSE
VHOLE(I)=VAC
END IF
END DO

OPEN (1,NAME='COMPOSITION.DAT')
X=0.
DO I=1,NUM2
X=X+DX2*R3
WRITE (1,50) X, C0(I),C1(I),VELEC(I),VHOLE(I),AEMASS(I),AHMASS(I)
END DO
CLOSE(UNIT=1)

!ELECTRON WAVE FUNCTION-------------------------------------
! S states
!calculate the V matrix
DO I=1,NT
DO J=1,I
V(I,J)=0.
DO IC=1,NUM2
X=IC*DX2
R=X*R3
BSLJ=AN0(J)*SIN(J*PI*X)/(J*PI*X)
BSLI=AN0(I)*SIN(I*PI*X)/(I*PI*X)
V(I,J)=V(I,J)+BSLJ*BSLI*R**2*DR*VELEC(IC)
END DO
V(J,I)=V(I,J)
END DO
END DO
```

```fortran
! calculate the T matrix
DO I=1,NT
DO J=1,I
T(I,J)=0.
DO IC=1,NUM2
X=IC*DX2
R=X*R3
BSLJ=AN0(J)*SIN(J*PI*X)/(J*PI*X)
BSLI=AN0(I)*SIN(I*PI*X)/(I*PI*X)
T(I,J)=T(I,J)+BSLJ*BSLI*R**2*DR*(1.0/AEMASS(IC))
END DO
T(I,J)=T(I,J)*EELEC*(J*PI)**2
T(J,I)=T(I,J)
END DO
END DO

! calculate the T1 matrix
DO I=1,NT
DO J=1,I
T1(I,J)=0.
DO IC=1,NUM2-2
X=IC*DX2
R=X*R3
BSLJ=AN0(J)*SIN(J*PI*X)/(J*PI*X)
BSLI=AN0(I)*(SIN(I*PI*(X+DX2))/(I*PI*(X+DX2))-SIN(I*PI*X)/(I*PI*X))/DR
T1(I,J)=T1(I,J)-(1.0/AEMASS(IC+1)-1.0/AEMASS(IC))*BSLJ*BSLI*R**2
END DO
T1(I,J)=T1(I,J)*EELEC
T1(J,I)=T1(I,J)
END DO
END DO

DO I=1,NT
DO J=1,NT
V(I,J)=V(I,J)+T(I,J)+T1(I,J)
END DO
END DO

CALL EVCSF(NT,V,LDA,EVAL,EVEC,LDEVEC)

DO I=1,NT
EE(I)=EVAL(NT-I+1)
END DO

! FE is the electron wavefunction
DO JS=1,NS
```

```fortran
DO IC=1,NUM2+1
FE(IC,JS)=0.0
END DO
END DO
DO JS=1,NS
DO IC=1,NUM2+1
X=IC*DX2
DO J=1,NT
FE(IC,JS)=FE(IC,JS)+EVEC(J,NT-JS+1)*AN0(J)*SIN(J*PI*X)/(J*PI*X)
END DO
END DO
END DO

DO JS=1,NS
TOT=0.
DO IC=1,NUM2
X=IC*DX2
R=X*R3
TOT=TOT+FE(IC,JS)**2*R**2*DR
END DO
DO IC=1,NUM2
FE(IC,JS)=FE(IC,JS)/SQRT(TOT)
END DO
END DO

!write the amplitude of the wavefunction at the particle surface
!do js=1,ns
!write (*,*) fe(num,js)**2
!end do

!P STATES
!calculate the V matrix
DO I=1,NT
DO J=1,I
V(I,J)=0.
DO IC=1,NUM2
X=IC*DX2
R=X*R3
BSLJ=AN1(J)*SB1(X*Z1(J))
BSLI=AN1(I)*SB1(X*Z1(I))
V(I,J)=V(I,J)+BSLJ*BSLI*R**2*DR*VELEC(IC)
END DO
V(J,I)=V(I,J)
END DO
END DO
```

```fortran
! calculate the T matrix
DO I=1,NT
DO J=1,I
T(I,J)=0.
DO IC=1,NUM2
X=IC*DX2
R=X*R3
BSLJ=AN1(J)*SB1(X*Z1(J))
BSLI=AN1(I)*SB1(X*Z1(I))
T(I,J)=T(I,J)+BSLJ*BSLI*R**2*DR*(1.0/AEMASS(IC))
END DO
T(I,J)=T(I,J)*EELEC*Z1(J)**2
T(J,I)=T(I,J)
END DO
END DO

! calculate the T1 matrix
DO I=1,NT
DO J=1,I
T1(I,J)=0.
DO IC=1,NUM2-2
X=IC*DX2
R=X*R3
BSLJ=AN1(J)*SB1(X*Z1(J))
BSLI=AN1(I)*(SB1((X+DX2)*Z1(I))-SB1(X*Z1(I)))/DR
T1(I,J)=T1(I,J)-(1.0/AEMASS(IC+1)-1.0/AEMASS(IC))*BSLJ*BSLI*R**2
END DO
T1(I,J)=T1(I,J)*EELEC
T1(J,I)=T1(I,J)
END DO
END DO

DO I=1,NT
DO J=1,NT
V(I,J)=V(I,J)+T(I,J)+T1(I,J)
END DO
END DO

CALL EVCSF(NT,V,LDA,EVAL,EVEC,LDEVEC)

DO I=1,NT
EE1(I)=EVAL(NT-I+1)
END DO

! FE is the electron wavefunction
DO JS=1,NS
```

```
DO IC=1,NUM2+1
FE1(IC,JS)=0.0
END DO
END DO
DO JS=1,NS
DO IC=1,NUM2+1
X=IC*DX2
DO J=1,NT
FE1(IC,JS)=FE1(IC,JS)+EVEC(J,NT-JS+1)*AN0(J)*SB1(X*Z1(J))
END DO
END DO
END DO

DO JS=1,NS
TOT=0.
DO IC=1,NUM2
X=IC*DX2
R=X*R3
TOT=TOT+FE1(IC,JS)**2*R**2*DR
END DO
DO IC=1,NUM2
FE1(IC,JS)=FE1(IC,JS)/SQRT(TOT)
END DO
END DO

!HOLE WAVE FUNCTION------------------------------------------------

! calculate the V matrix
DO I=1,NT
DO J=1,I
V(I,J)=0.
DO IC=1,NUM2
X=IC*DX2
R=X*R3
BSLJ=AN0(J)*SIN(J*PI*X)/(J*PI*X)
BSLI=AN0(I)*SIN(I*PI*X)/(I*PI*X)
V(I,J)=V(I,J)+BSLJ*BSLI*R**2*DR*VHOLE(IC)
END DO
V(J,I)=V(I,J)
END DO
END DO

! calculate the T matrix
DO I=1,NT
DO J=1,I
T(I,J)=0.
```

```fortran
DO IC=1,NUM2
X=IC*DX2
R=X*R3
BSLJ=AN0(J)*SIN(J*PI*X)/(J*PI*X)
BSLI=AN0(I)*SIN(I*PI*X)/(I*PI*X)
T(I,J)=T(I,J)+BSLJ*BSLI*R**2*(DR/AHMASS(IC))
END DO
T(I,J)=T(I,J)*EHOLE*(J*PI)**2
T(J,I)=T(I,J)
END DO
END DO

! calculate the T1 matrix
DO I=1,NT
DO J=1,I
T1(I,J)=0.
DO IC=1,NUM2-2
X=IC*DX2
R=X*R3
BSLJ=AN0(J)*SIN(J*PI*X)/(J*PI*X)
BSLI=AN0(I)*(SIN(I*PI*(X+DX2))/(I*PI*(X+DX2))-SIN(I*PI*X)/(I*PI*X))/DR
T1(I,J)=T1(I,J)-(1.0/AHMASS(IC+1)-1.0/AHMASS(IC))*BSLJ*BSLI*R**2
END DO
T1(I,J)=T1(I,J)*EHOLE
T1(J,I)=T1(I,J)
END DO
END DO

DO I=1,NT
DO J=1,NT
V(I,J)=V(I,J)+T(I,J)+T1(I,J)
END DO
END DO

CALL EVCSF(NT,V,LDA,EVAL,EVEC,LDEVEC)

DO I=1,NT
EH(I)=EVAL(NT-I+1)
END DO

! FH is the hole wavefunction
DO JS=1,NS
DO IC=1,NUM2
X=IC*DX2
FH(IC,JS)=0.
DO J=1,NT
```

```
FH(IC,JS)=FH(IC,JS)+EVEC(J,NT-JS+1)*AN0(J)*SIN(J*PI*X)/(J*PI*X)
END DO
END DO
END DO

DO JS=1,NS
TOT=0.
DO IC=1,NUM2
X=IC*DX2
R=X*R3
TOT=TOT+FH(IC,JS)**2*R**2*DR
END DO
DO I=1,NUM2
FH(IC,JS)=FH(IC,JS)/SQRT(TOT)
END DO
END DO


!-------------------------------------------------------------------------
!write electron and hole energies
write (*,*) "    n        nSe energy   nPe energy   nSh energy"
do i=1,ns
write (*,*) i,ee(i), ee1(i), eh(i)
end do


!-------------------------------------------------------------------------
! electron-hole interaction
WRITE (*,*)
! electron wavefunction
DO JS=1,8
TOT=0.
DO I=1,NUM2
DO J=1,NUM2
RE=I*DR
RH=J*DR
IF (RE > RH)THEN
X=RE
ELSE
X=RH
END IF
TOT=TOT+RE**2*RH**2*FH(J,1)**2*FE(I,1)*FE(I,JS)*DR**2*(1.0/X)
END DO
END DO
TOT=TOT*EHCONST/DCONST

DO I=1,NUM2
FELEC(I)=FE(I,1)
```

174

```
END DO
DO I=1,NUM2
FELEC(I)= FELEC(I)+(TOT/(EE(JS)-EE(1)))*FE(I,JS)
END DO
END DO
WRITE(*,*)
! hole wavefunction

DO JS=1,8
TOT=0.
DO I=1,NUM2
DO J=1,NUM2
RE=I*DR
RH=J*DR
IF (RE > RH)THEN
X=RE
ELSE
X=RH
END IF
TOT=TOT+RE**2*RH**2*FE(I,1)**2*FH(J,1)*FH(J,JS)*DR**2*(1.0/X)
END DO
END DO
TOT=TOT*EHCONST/DCONST

DO I=1,NUM2
FHOLE(I)=FH(I,1)
END DO
DO I=1,NUM2
FHOLE(I)= FHOLE(I)+(TOT/(EH(JS)-EH(1)))*FH(I,JS)
END DO
END DO

! renormalize wavefunctions
TOT=0.
DO IC=1,NUM2
X=IC*DX2
R=X*R3
TOT=TOT+FELEC(IC)**2*R**2*DR
END DO
DO IC=1,NUM2
FELEC(IC)=FELEC(IC)/SQRT(TOT)
END DO
TOT=0.
DO IC=1,NUM2
X=IC*DX2
R=X*R3
```

```fortran
TOT=TOT+FHOLE(IC)**2*R**2*DR
END DO
DO IC=1,NUM2
FHOLE(IC)=FHOLE(IC)/SQRT(TOT)
END DO

!calculate 1Pe - hole attraction energy of first order corrected functions
TOT=0.
DO I=1,NUM2
DO J=1,NUM2
RE=I*DX2*R3
RH=J*DX2*R3
IF (RE > RH)THEN
X=RE
ELSE
X=RH
END IF
TOT=TOT+RE**2*RH**2*FHOLE(J)**2*FE1(I,1)**2*(1.0/X)*DR**2
END DO
END DO
TOT=TOT*EHCONST/DCONST
QCE=EE(1)+EH(1)-TOT
WRITE (*,*) "uncorrected 1Pe/1Sh interacion energy", TOT

!calculate electron-hole attraction energy of first order corrected functions
TOT=0.
DO I=1,NUM2
DO J=1,NUM2
RE=I*DX2*R3
RH=J*DX2*R3
IF (RE > RH)THEN
X=RE
ELSE
X=RH
END IF
TOT=TOT+RE**2*RH**2*FHOLE(J)**2*FELEC(I)**2*(1.0/X)*DR**2
END DO
END DO
TOT=TOT*EHCONST/DCONST
QCE=EE(1)+EH(1)-TOT
WRITE (*,*) "corrected 1Se/1Sh interacion energy", TOT
write (*,*) "onset wavelength =",1.e+7/(ee(1)+eh(1)-tot+ CORX +VE)
Write (*,*)

!calculate the electron hole overlap
S1=0
```

```fortran
DO IC=1,NUM2
X=IC*DX2
R=X*R3
S1=S1+FHOLE(IC)*FELEC(IC)*R**2*DR
END DO
S1=S1**2
WRITE (*,*) "corrected 1Se/1Sh overlap =", S1
write (*,*)

! calculate electron hole overlap for unperturbed electron functions
! 1S
S1=0
DO IC=1,NUM2
X=IC*DX2
R=X*R3
S1=S1+FHOLE(IC)*FE(IC,1)*R**2*DR
END DO
S1=S1**2
WRITE (*,*) "1Se/1Sh overlap =",S1

!1P
S1=0
DO IC=1,NUM2
X=IC*DX2
R=X*R3
S1=S1+FHOLE(IC)*FE1(IC,1)*R**2*DR
END DO
S1=S1**2
WRITE (*,*) "1Pe/1Sh overlap =",S1

! 2S
S1=0
DO IC=1,NUM2
X=IC*DX2
R=X*R3
S1=S1+FHOLE(IC)*FE(IC,2)*R**2*DR
END DO
S1=S1**2
WRITE (*,*) "2Se/1Sh overlap =", S1

OPEN (1,NAME='FUNCTION.DAT')
DO IC=1,NUM2
X=(IC-1)*DX2
WRITE (1,50) X*R3,FHOLE(IC),FELEC(IC),FH(IC,1),FE(IC,1)
!,FE(IC,2),FE1(IC,2)
!WRITE (1,50) X*R3,(FE(IC,I), I=1,NS),(FH(IC,I), I=1,NS)
```

```
END DO
CLOSE (UNIT=1)

!-------------------------------------------------------------------------

!calculate relative dipolar mixing between lowest s and np states
OPEN(1,NAME='DIELECTRIC.DAT')
XD=1.6
!do je=1,50
XD=XD+.2
efield=0.60775-0.0699* XD+0.00929* XD**2-7.03874E-4* XD**3+2.2282E-5* XD**4
EFIELD=EFIELD*8065.
efield=0.
DO JS=1,NS
TOT=0.
DO IC=1,NUM2
X=IC*DX2
R=X*R3
TOT=TOT+FE1(IC,JS)*FE(IC,1)*R**3*DR
END DO
AMIX(JS)=TOT
AMIX2(JS)=efield*AMIX(JS)/(EE1(JS)-EE(1))
END DO
!write (*,*)
!write (*,*) "1Se-nPe  state mixing", efield, AMIX2(1)**2

!-------------------------------------------------------------------------
!do the Fourier-Bessel transform of the lowest electron and hole functions
AUGERE= 0.0571* SQRT(CMASSE)* SQRT(ee(1)+eh(1)+ 12100.+VE)
AUGERH= 0.0571* SQRT(CMASSH)* SQRT(ee(1)+eh(1)+ 12100.+VE)
! k value associated with the bandgap energy
! k nm = 0.0571 * SQRT(m*) * sqrt(E/wavenumbers)
DK=0.02
NKE=AUGERE/DK
NKH=AUGERH/DK
NK=300
do k=1,nk
FKE(K)=0
FKH(K)=0
FKE1(K)=0
FKE2(K)=0
FKE3(K)=0
END DO
DO K=1,NK
RK=K*DK
DO IC=1,NUM2
```

```fortran
X=IC*DX2
R=X*R3
FKE(K)=FKE(K)+R**2*DR*FELEC(IC)*SIN(R*RK)/(R*RK)
FKH(K)=FKH(K)+R**2*DR*FHOLE(IC)*SIN(R*RK)/(R*RK)
FKE1(K)=FKE1(K)+R**2*DR*FE1(IC,1)*SB1(R*RK)
FKE2(K)=FKE2(K)+R**2*DR*FE1(IC,2)*SB1(R*RK)
FKE3(K)=FKE3(K)+R**2*DR*FE1(IC,3)*SB1(R*RK)
END DO
FKET(K)=FKE(K)+FKE1(K)*AMIX2(1)+FKE2(K)*AMIX2(2)+FKE3(K)*AMIX2(3)
END DO
WRITE (*,*) XD, efield, FKET(NKE)**2
WRITE (1,50) XD, efield, FKET(NKE)**2
!WRITE (*,*) "electron k^2 values, w/o and w/ mixing", efield, FKE(NKE)**2,
FKET(NKE)**2
!end do
CLOSE(UNIT=1)
!stop
OPEN (1,NAME='XFORM.DAT')

DO I=1,NK
WRITE (1,50) I*DK,FKE(I)**2,FKH(I)**2, FKE1(I)**2, FKE2(I)**2, FKE3(I)**2,
FKET(I)**2
END DO

CLOSE(UNIT=1)
STOP
!------------------------------------------------------------------
!Calculate Raman spectrum
NONRES=.0
DO IC=1,NUM
XC=(1.0-C1(IC))
OMEGA=211.5 + 71.3*XC - 27.9*XC**2
I=INT(OMEGA)
DO IC2=-100,100
A=GAMMA**2/(IC2**2+GAMMA**2)
IC3=I-IC2
if (IC3 .le. 0) then
cycle
end if
RS(IC3)=RS(IC3)+A*(NONRES+abs(FELEC(IC)*FHOLE(IC)))*IC**2
END DO
END DO
OPEN (1,NAME='RAMAN.DAT')
DO I=1,400
!WRITE (*,*) I+200, RS(I)/NUM
WRITE (1,60) I, RS(I)/NUM
```

```fortran
END DO
CLOSE(UNIT=1)
STOP

50 FORMAT (11F15.8)
60 FORMAT (I5,F12.5)
70 FORMAT (3F14.5,3I6)

END

FUNCTION SB0(X)
SB0 = SIN(X)/X
RETURN
END

Function SB1(X)
SB1=SIN(X)/X**2-COS(X)/X
RETURN
END

! THIS PROGRAM USES THE IMSL ROUTINE CALL
EVCSF(N,A,LDA,EVAL,EVEC,LDEVEC)
! To link in the IMSL library, one goes to
!  Project > Settings > Fortran > Libraries and check Use IMSL Math Library
! N - ORDER OF THE MATRIX
! REAL MATRIX OF ORDER N
! LDA - LEADING DIMENION OF A (DIMENSION STATEMENT)
! EVAL - OUTPUT- VECTOR OF THE EIGENVALUES
! EVEC - OUTPUT - MATRIX OF THE EIGENVECTORS; J'TH EIGENVECTOR IS IN THE
J'COLUMN
! LDEVEC - LEADING DIMENSION OF EVEC (DIMENSION STATEMENT)
```

REFERENCES

1 Peter Y. Yu and Manuel Cardona , *Fundamentals of Semiconductors: Physics and Materials Properties*, New York: Springer **2010**

2 V. Chikan, D. F. Kelley, "Synthesis of Highly Luminescent GaSe Nanoparticles", *Nano Lett.* **2002**, *2*, 141

3 E. Mooser, M. Schluter, "The Band-Gap Excitons in Gallium Selenide", *Nuovo Cimento* **1973**, *18B*, 164

4 H. Tu, S. Yang, V. Chikan, and D.F. Kelley, "Spectroscopy of GaSe Nanoparticle Aggregates", *J. Phys. Chem. B* **2004**, *108*, 4701

5 H. Mirafzal, D. F. Kelley, "Singlet/Triplet Reversal in Strongly Coupled GaSe Nanoparticle Aggregates", *J. Phys. Chem. C*. **2009**, *113*, 7139

6 M. O. D. Camara, A. Mauger, "Electronic Structure of the Layer Compounds GaSe and InSe in a Tight-Binding Approach", *Phys. Rev. B*. **2002**, *65*, 125206

7 H. Tu, K. Mogyorosi, D. F. Kelley, "Intraband Spectroscopy and Photophysics in GaSe Nanoparticles", *Phys. Re*V. *B*. **2005**, *72*, 205306

8 V. Chikan, D. F. Kelley, "Relaxation Dynamics in Photoexcited GaSe Nanoparticles", *J. Chem. Phys.* **2002**, *117*, 8944

9 V. Chikan, D. F. Kelley, "Carrier Relaxation Dynamics in GaSe Nanoparticles", *Nano Lett.* **2002**, *2*, 1015

10 H. Tu, V. Chikan, D. F. Kelley, "Electron and Hole Intraband Spectroscopy of GaSe Nanoparticles", *J. Phys. Chem. B* **2003**, *107*, 10389

11 H. Tu, D. F. Kelley, "Photoinduced Direct Electron Transfer from InSe to GaSe Semiconductor Nanoparticles", *Nano Lett.* **2006**, *6*, 116

12 H. Tu, K. Mogyorosi, D. F. Kelley, "Exciton Dynamics of GaSe Nanoparticle Aggregates", *J. Chem. Phys.* **2005**, *122*, 44709

13 E. E. Jelly, *Nature* **1937**, *139*, 631

14 E. O. Potma, D. A. Wiersma, "Exciton Superradiance in Aggregates: The Effect of Disorder, Higher Order Exciton-Phonon Coupling and Dimensionality", *J. Chem. Phys.* **1998**, *108*, 4894

15 J. Moll, S. Daehne, J. R. Durrant, D. A. Wiersma, "Optical Dynamics of Excitons in J Aggregates of a Carbocyanine Dye", *J. Chem. Phys.* **1995**, *102*, 6362

16 H. Fidder, J. Knoester, D. A. Wiersma, "Observation of the One-Exciton to Two-Exciton Transition in a J Aggregate", *J. Chem. Phys.* **1993**, *98*, 6564

17 F. Spano, S. Mukamel, "Superradiance in Molecular Aggregates", *J. Chem. Phys.* **1989**, *91*, 683

18 X. Peng, J. Wickham, and A. P. Alivisatos, "Kinetics of II-VI and III-V Colloidal Semiconductor Nanocrystal Growth: "Focusing" of Size Distributions" *J. Am. Chem. Soc.* **1998**, *120,* 5343

19 C. B. Murray, D. J. Norris, and M. G. Bawendi, "Synthesis and Characterization of Nearly Monodisperse CdE (E = S, Se, Te) Semiconductor Nanocrystallites", *J. Am. Chem. Soc.* **1993,** *115,* 8706

20 J. Jasieniak, C. Bullen, J. van Embden, and P. Mulvaney, "Phosphine-Free Synthesis of CdSe Nanocrystals " *J. Phys. Chem. B.* **2005**, *109,* 20665

21 Fudong Wang, Rui Tang and William E. Buhro, "The Trouble with TOPO; Identification of Adventitious Impurities Beneficial to the Growth of Cadmium Selenide Quantum Dots, Rods, and Wires", Nano Lett. 2008, 8 (10), 3521

22 Fudong Wang, Rui Tang, Jeff L.-F. Kao, Sean D. Dingman and William E. Buhro, "Spectroscopic Identification of Tri-n-octylphosphine Oxide (TOPO) Impurities and Elucidation of Their Roles in Cadmium Selenide Quantum-Wire Growth", J. Am. Chem. Soc. 2009, 131 (13), 4983

23 Deborah L. Lair, *Spectroscopy of Gallium Selenide Nanoparticle Nuclei*, Merced: University of California – Merced **2011**

24 A. Hasegawa, Y. Mitsumori, F. Minami, "Polarization Dependence of the Stimulated Photon Echo Due to Excitons in GaSe", *J. Lumin.* **1995**, *66*, 51

25 J. Shao, H. Mirafzal, J. R. Petker, J. L. S. Cosio, D. F. Kelley, T. Ye, "Nanoscale Organization of GaSe Quantum Dots on a Gold Surface", *J. Phys. Chem. C*. **2009**, *113*, 19102

26 J. T. Kopping, T. E. Patten, "Identification of Acidic Phosphorus-Containing Ligands Involved in the Surface Chemistry of CdSe Nanoparticles Prepared in Tri-*N*-octylphosphine Oxide Solvents", *J. Am. Chem. Soc.* **2008**, *130*, 5689

27 H. Liu, J. S. Owen, A. P. Alivisatos, "Mechanistic Study of Precursor Evolution in Colloidal Group II-VI Semiconductor Nanocrystal Synthesis", *J. Am. Chem. Soc.* **2007**, *129*, 305

28 K. Mogyorosi, D. F. Kelley, "Superradiance in GaSe Nanoparticle Aggregates", *J. Phys. Chem. C*. **2007**, *111*, 579

29 M. Schluter, "The Electronic Structure of GaSe", *Nuovo Cimento* **1973**, *13B*, 313

30 L. C. T. Shoute, D. F. Kelley, "Spatial Organization of GaSe Quantum Dots: Organic/Semiconductor Liquid Crystals", *J. Phys. Chem. C*. **2007**, *111*, 579

31   M. D. Lynch, D. L. Patrick, "Organizing Carbon Nanotubes with Liquid Crystals" *Nano Lett.* **2002***, 2,* 1197

32   R. K. Lammi, K. P. Fritz, G. D. Scholes, P. F. Barbara, "Ordering of Single Conjugated Polymers in a Nematic Liquid Crystal Host" *J. Phys. Chem. B* **2004***, 108,* 4593

33 S. Link, D. Hu, W.-S. Chang, G. D. Scholes, P. F. Barbara, "Nematic Solvation of Segmented Polymer Chains" *Nano Lett.* **2005***, 5,* 1757

34 D. Sharma, J. C. MacDonald, G. S. Iannacchione, "Thermodynamics of Activated Phase Transitions of 8CB: DSC and MC Calorimetry" *J. Phys. Chem. B.* **2006**, *110*, 16679

35 Y. K. Verma, R. H. Inman, C. G. L. Ferri, H. Mirafzal, S. N. Ghosh, D. F. Kelley, L. S. Hirst, S. Ghosh, "Electrical Modulation of Static and Dynamic Spectroscopic Properties of Coupled GaSe Quantum Dot Nano-Assemblies", *Phys. Rev. B.* **2010**, *82*, 165428

36 M.O.D. Camara, A. Mauger, I. Devos, "Electronic Structure of the Layer Compounds GaSe and InSe in a Tight-binding Approach", *Phys. Rev. B.* **2002**, *65*, 125206

37 Zh. I. Alferov, "The History and Future of Semiconductor Heterostructures", *Fiz. Tekh. Poluprovodn.* **1998**, *32*, 1

38 R. Dingle, W. Wiegmann, and C. H. Henry, "Quantum States of Confined Carriers in Very Thin AlxGa1-xAs-GaAs-AlxGa1-xAs Heterostructures", *Phys. Rev. Lett.* **1974**, *33*, 827

39 A. R. West, *Basic Solid State Chemistry*, Wiley **1988**

40 A. Peng, X. Peng, "Mechanisms of the Shape Evolution of CdSe Nanocrystals", *J. Am. Chem. Soc*. **2001,** *123*, 1389

41 X. Peng, L. Manna, W. Yang, Juanita Wickham, E. Scher, A. Kadavanich, A. P. Alivisatos, "Shape control of CdSe nanocrystals", *Nature* **2000,** *404*, 59

42 Z. A. Peng, X. Peng, "Nearly Monodisperse and Shape-Controlled CdSe Nanocrystals via Alternative Routes: Nucleation and Growth", *J. Am. Chem. Soc*. **2002,** *124*, 3343

43 W. Wang, S. Banerjee, S. Jia, M. L. Steigerwald, I. P. Herman, "Ligand Control of Growth, Morphology, and Capping Structure of Colloidal CdSe Nanorods", *Chem. Mater.* **2007,** *19*, 2573

44 D. V. Talapin, J. H. Nelson, E. V. Shevchenko, S. Aloni, B. Sadtler, A. P. Alivisatos, "Seeded Growth of Highly Luminescent CdSe/CdS Nanoheterostructures with Rod and Tetrapod Morphologies", *Nano Lett.* **2007,** *7*, 2951

45 F. Shieh, A. E. Saunders, and B. A. Korgel, "General Shape Control of Colloidal CdS, CdSe, CdTe Quantum Rods and Quantum Rod Heterostructures", *Phys. Chem. B* **2005** , *109*, 8538

46 L. Xi, C. Boothroyd, and Y. M. Lam, "Controlled Synthesis of CdTe and CdSe Multiblock Heteronanostructures", *Chem. Mater.* **2009,** *21*, 1465

47 L. Manna, D. J. Milliron, A. Meisel, E. C. Scher, A. P. Alivisatos, "Controlled Growth of Tetrapod-branched Inorganic Nanocrystals", *Nature materials* **2003,** *2*, 385

48 S. S. Lo, T. Mirkovic, C. Chuang, C. Burda, G. D. Scholes, "Emergent Properties Resulting from Type-II Band Alignment in Semiconductor Nanoheterostructures", *Adv. Mater.* **2011**, *23*, 180

49 C. Chuang, S. S. Lo, G. D. Scholes, C. Burda, "Charge Separation and Recombination in CdTe/CdSe Core/Shell Nanocrystals as a Function of Shell Coverage: Probing the Onset of the Quasi Type-II Regime", *J. Phys. Chem. Lett*. **2010**, *1*, 2530

50 D. Oron, M. Kazes, U. Banin, "Multiexcitons in type-II colloidal semiconductor quantum dots ", *Phys. Rev. B* **2007,** *75*, 035330

51 C. M. Donega, "Formation of Nanoscale Spatially Indirect Excitons: Evolution of the Type II Optical Character of CdTe/CdSe Heteronanocrystals", *Phys. Rev. B*. **2010**, *81*, 165303

52 C. J. Dooley, S. D. Dimitrov, T. Fiebig, "Ultrafast Electron Transfer Dynamics in CdSe/CdTe Donor-Acceptor Nanorods", *J. Phys. Chem. C. Lett*. **2008**, *112*, 12074

53 S. Kumar, M. Jones, S. S. Lo, G. D. Scholes, "Nanorod Heterostructures Showing Photoinduced Charge Separation", *Small* **2007**, *3*, 1633

54 P. Peng, D. J. Milliron, S. M. Hughes, J. C. Johnson, A. P. Alivisatos, R. J. Saykally, "Femtosecond Spectroscopy of Carrier Relaxation Dynamics in Type II CdSe/CdTe Tetrapod Heteronanostructures", *Nano Lett*. **2005**, *5*, 1809

55 A. L. Rogach, A. Kornowski, M. Gao, A. Eychmuller, H. Weller, "Synthesis and

Characterization of a Size Series of Extremely Small Thiol-Stabilized CdSe Nanocrystals", *J. Phys. Chem. B* **1999**, *103*, 3065

56 Y. Masumoto, K. Sonobe, "Size-dependent Energy Levels of CdTe Quantum Dots", *Phys. Rev. B* **1997**, *56*, 9734

57 W. W. Yu, Y. A. Wang, X. Peng, "Formation and Stability of Size-, Shape-, and Structure-Controlled CdTe Nanocrystals: Ligand Effects on Monomers and Nanocrystals", *Chem. Mater.* **2003**, *15*, 4300

58 M. B. Mohamed, D. Tonti, A. Al-Salman, A. Chemseddine, M. Chergui, "Synthesis of High Quality Zinc Blende CdSe Nanocrystals", *J. Phys. Chem. B. Lett*. **2005**, *109*, 10533

59 R. K. Capek, I. Moreels, K. Lambert, D. De Muynck, Q. Zhao, A. Van Tomme, F. Vanhaecke, Z. Hens, "Optical Properties of Zincblende Cadmium Selenide Quantum Dots", *J. Phys. Chem. C* **2010**, *114*, 6371

60 H. Zhong, G. D. Scholes, "Shape Tuning of Type II CdTe-CdSe Colloidal Nanocrystal Heterostructures Through Seeded Growth", *J. Am. Chem. Soc*. **2009**, *131*, 9170

61 C. Burda, S. Link, M. Mohamed, M. A. El-Sayed, "The Relaxation Pathways of CdSe Nanoparticles Monitored with Femtosecond Time-Resolution from the Visible to the IR: Assignment of the Transient Features by Carrier Quenching", *J. Phys. Chem. B* **2001,** *105*, 12286

62 J. A. McGuire, J. Joo, J. M. Pietryga, R. D. Schaller, V. I. Klimov, "New Aspects of Carrier Multiplication in Semiconductor Nanocrystals", *Acc. Chem. Res* **2008,** *41*, 1810

63 M. A. El-Sayed, "Small Is Different: Shape-, Size-, and Composition-Dependent Properties of Some Colloidal Semiconductor Nanocrystals", *Acc. Chem. Res*. **2004,** *37*, 326

64 M. B. Mohamed, C. Burda, M. A. El-Sayed, "Shape Dependent Ultrafast Relaxation Dynamics of CdSe Nanocrystals: Nanorods vs Nanodots", *Nano Lett.* **2001,** *1*, 589

65 G. E. Cragg, A. L. Efros, "Suppression of Auger Processes in Confined Structures", *Nano Lett*. **2010,** *10*, 313

66 A. M. Smith, A. M. Mohs, S. Nie, "Tuning the Optical and Electronic Properties of Colloidal Nanocrystals by Lattice Strain", *Nature Nanotechnology* **2009**, *4*, 56

67 J. Rockenberger, L. Tröger, A. L. Rogach, M. Tischer, M. Grundmann, A. Eychmüller, H. Weller, "The Contribution of Particle Core and Surface to Strain, Disorder and Vibrations in

Thiolcapped CdTe Nanocrystals", *J. Chem. Phys*. **1998**, *108*, 7807

68 A. Piryatinski, S. A. Ivanov, S. Tretiak, V. I. Klimov, "Effect of Quantum and Dielectric Confinement on the Exciton-Exciton Interaction Energy in Type II Core/Shell Semiconductor Nanocrystals", *Nano Lett.* **2007,** *7*, 108

69 V. I. Klimov, "Spectral and Dynamical Properties of Multiexcitons in Semiconductor Nanocrystals", *Annu. Rev. Phys. Chem.* **2007,** *58*, 635

70 R. M. Kraus, P. G. Lagoudakis, J. Müller, A. L. Rogach, J. M. Lupton, J. Feldmann, D. V. Talapin, H. Weller, "Interplay between Auger and Ionization Processes in Nanocrystal Quantum Dots", *J. Phys. Chem. B* **2005,** *109*, 18214

71 J. Nanda, S. A. Ivanov, H. Htoon, I. Bezel, A. Piryatinski, S. Tretiak, and V. I. Klimov, "Absorption cross sections and Auger recombination lifetimes in inverted core-shell nanocrystals: Implications for lasing performance", *J. Appl. Phys* **2006,** *99*, 34309

72 L. P. Balet, S. A. Ivanov, A. Piryatinski, M. Achermann, and V. I. Klimov, "Inverted Core/Shell Nanocrystals Continuously Tunable between Type-I and Type-II Localization Regimes", *Nano Letters* **2004,** *4*, 1485

73 V. I. Klimov, A. A. Milhailosky, D. W. McBranch, C. A. Leatherdale, M. G. Bawendi, "Mechanisms for intraband relaxation in semiconductor quantum dots: The role of electron-hole interactions", *Phys. Rev. B* **2000,** *61*, R13349

74 R. R. Cooney, S. L. Sewall, E. A. Dias, D. M. Sagar, K. E. H. Anderson, P. Kambhampati, "Unified picture of electron and hole relaxation pathways in semiconductor quantum dots ", *Phys. Rev. B* **2007,** *75*, 245311

75 S. Xu, A. A. Mikhailovsky, J. A. Hollingsworth, V. I. Klimov, "Hole intraband relaxation in strongly confined quantum dots: Revisiting the "phonon bottleneck" problem", *Phys. Rev. B* **2002,** *65*, 45319

76 M. Califano, "Efficient Auger Electron Cooling in Seemingly Unfavorable Configurations: Hole Traps and Electrochemical Charging", *J. Phys. Chem. C* **2008,** *112*, 8570

77 E. Hendry, M. Koeberg, F. Wang, H. Zhang, C. d. M. Donegá, D. Vanmaekelbergh, and M. Bonn, "Direct Observation of Electron-to-Hole Energy Transfer in CdSe Quantum Dots", *Phys. Rev. Lett*. **2006,** *96*, 57408

78 P. Guyot-Sionnest, M. Shim, C. Matranga, and M. Hines, "Intraband Relaxation in CdSe

Quantum Dots", *Phys. Rev. B* **1999,** *60*, R2181

79 P. Guyot-Sionnest and M. A. Hines, "Intraband transitions in semiconductor nanocrystals", *App. Phys. Lett*. **1998,** *72*, 686

80 P. Guyot-Sionnest, B. Wehrenberg, and D. Yu, "Intraband relaxation in CdSe nanocrystals and the strong influence of the surface ligands", *J. Chem. Phys*. **2005,** *123*, 074709

81 A. Pandey and P. Guyot-Sionnest, "Slow Electron Cooling in Colloidal Quantum Dots", *Science* **2008,** *322*, 929

82 P. Peng, D. J. Milliron, S. M. Hughes, J. C. Johnson, A. P. Alivisatos, and R. J. Saykally, "Femtosecond Spectroscopy of Carrier Relaxation Dynamics in Type II CdSe/CdTe Tetrapod Heteronanostructures", *Nano Lett.* **2005,** *5*

83 D. Oron, M. Kazes, and U. Banin, "Multiexcitons in type-II colloidal semiconductor quantum dots ", *Phys. Rev. B* **2007,** *75*, 035330